

Fabrication and analysis of co-diffused *n*-type silicon solar cells applying plasma-deposited diffusion sources

Von der Fakultät für Mathematik und Physik
der Gottfried Wilhelm Leibniz Universität Hannover
zur Erlangung des Grades

Doktorin der Naturwissenschaften
(Dr. rer. nat.)

genehmigte Dissertation

von

M.Sc.Phys. Nadine Wehmeier

geboren am 31.10.1986 in Bünde

2016

Referent: Prof. Dr. Jan Schmidt
Korreferent: Prof. Dr.-Ing. Tobias Wietler
Tag der Promotion: 20. Oktober 2016

Kurzzusammenfassung

Die Herstellung von n -Typ Silizium-Solarzellen lässt sich durch die Anwendung einer multifunktionalen Plasma-abgeschiedenen Bor-Dotierquelle und eines Ko-Diffusionsprozesses deutlich vereinfachen. Dadurch können Hochtemperatur-Diffusionen sowie Beschichtungs- und Ätz-Schritte eingespart und Solarzellen kosten- und zeiteffizienter hergestellt werden. In der vorliegenden Arbeit optimieren wir die Plasma-Gasphasenabscheidung (PECVD) von Bor-Silikatglas (BSG), das als einseitige Dotierquelle dient. Der Einfluss des PECVD Gasfluss-Verhältnisses von Silan (SiH_4) und Diboran (B_2H_6) und der BSG-Schichtdicke auf die resultierende Bor-Diffusion wird untersucht. Wir entwickeln eine zweistufige POCl_3 -Ko-Diffusion mit einem Bor-Eintreibeschritt bei 950°C in Stickstoff-Atmosphäre, gefolgt von einer POCl_3 -Diffusion bei 829°C . Dadurch können sowohl der Bor p^+ -Rückseiten-Emitter als auch das Phosphor n^+ -Front Surface Field (FSF) in einem einzigen Hochtemperatur-Prozess ausgebildet werden. Als Phosphor-Diffusionsbarriere und als Schutzschicht während chemischer Reinigungs- und Texturschritte ist eine Abdeckschicht auf der BSG-Schicht erforderlich. Es werden PECVD-Nitrid (SiN_z) und PECVD-Oxinitrid (SiO_xN_y) Abdeckschichten untersucht. Ein PECVD-Schichtstapel aus 40 nm BSG mit $[\text{SiH}_4]/[\text{B}_2\text{H}_6]=8\%$ und 120 nm SiN_z stellt sich als optimale Bor-Dotierquelle heraus. Damit werden Sättigungsstromdichten J_0 unter 10 fA/cm^2 für eine Aluminiumoxid (AlO_x)-Passivierung des p^+ -Emitters erreicht. Mit dieser PECVD-BSG/ SiN_z Dotierquelle demonstrieren wir ko-diffundierte, monofaciale n -Typ Passivated Emitter and Rear, Rear Totally doped Back Junction (PERT BJ) Solarzellen mit einem Rekord-Wirkungsgrad von 21.0%. Durch die Verwendung der alternativen Dotierquelle und der Ko-Diffusion lässt sich die Anzahl der Prozessschritte gegenüber n -PERT BJ Zellen mit separaten Diffusionen verrin-

gern und der Herstellungsprozess vereinfachen. Zur weiteren Prozessvereinfachung wird der multifunktionale Einsatz der PECVD-Schichtstapel zugleich als Dotierquelle und als Rückseitenpassivierung statt $\text{AlO}_x/\text{SiN}_y$ betrachtet. Wir untersuchen die Passivierqualität und den Grenzflächen-Passiviermechanismus von PECVD-BSG Schichten und erreichen niedrigste publizierte J_0 Werte für eine BSG/ SiN_z -Passivierung auf einem p^+ -Emitter von 40 fA/cm^2 . Wir stellen ein neues n -Typ Cz-Si Zellkonzept mit der Bezeichnung Bifacial Co-diffused Rear Emitter (BiCoRE) vor, das eine Weiterentwicklung der n -PERT BJ Zellen darstellt. Die ersten BiCoRE-Zellen erreichen 20.6% Effizienz und 78% Bifacialität. Der BiCoRE Prozessfluss und die Prozesskomplexität sind vergleichbar zu industriellen, siebgedruckten p -Typ Passivated Emitter and Rear Cells (PERC), jedoch ermöglicht das n -Typ Silizium-Substrat, das nicht durch lichtinduzierte Degradation (LID) beeinträchtigt wird, stabile Zelleffizienzen. Wir entwickeln ein Simulations-Modell, das die Bor-Diffusion aus der PECVD-BSG-Schicht in das Silizium beschreibt und ermöglicht, die experimentellen Bor-Diffusionsprofile nach Ko-Diffusion nachzusimulieren. Zellsimulationen mit Verlust- und Effizienzgewinn-Analysen der ko-diffundierten Zellen werden durchgeführt, um Rekombinationsverluste und potenzielle Effizienzgewinne zu identifizieren. Die Simulationen bestätigen die hohe Qualität unserer PECVD-BSG-Dotierquellen.

Schlagworte:

Plasma-Gasphasenabscheidung,

Bor-Silikatglas-Dotierquelle und -Passivierung,

Vereinfachte ko-diffundierte n -Typ Silizium Solarzellen.

Abstract

The processing of *n*-type silicon solar cells can be significantly simplified by applying a multifunctional plasma-deposited boron diffusion source and a co-diffusion process. Thus, high-temperature furnace diffusions as well as deposition and etching steps can be reduced and solar cells can be fabricated more cost- and time-efficiently. In this work, we optimize the plasma-enhanced chemical vapor deposition (PECVD) of boron silicate glass (BSG) which is used as a single-sided solid diffusion source. The influence of the gas flow ratio of the precursor gases silane (SiH_4) and diborane (B_2H_6) during PECVD and of the BSG layer thickness on the resulting boron diffusion is investigated. We develop a two-stage POCl_3 co-diffusion with a boron drive-in step at 950°C in nitrogen ambient followed by a POCl_3 diffusion at 829°C . Thus, both the boron p^+ -rear side emitter and the phosphorus n^+ -front surface field (FSF) are formed in a single high-temperature process. As a phosphorus diffusion barrier and as a protection layer during chemical cleaning and texturing steps, a capping layer needs to be applied on top of the BSG layer. PECVD nitride (SiN_2) and oxynitride (SiO_xN_y) capping layers are investigated. A PECVD stack of 40 nm BSG with $[\text{SiH}_4]/[\text{B}_2\text{H}_6]=8\%$ and 120 nm SiN_2 is identified as optimized boron diffusion source that allows for saturation current densities J_0 below 10 fA/cm^2 for an aluminium oxide (AlO_x) passivation of the p^+ -emitter. With this PECVD BSG/ SiN_2 diffusion source, we demonstrate co-diffused monofacial *n*-type Passivated Emitter and Rear, Rear Totally doped Back Junction (PERT BJ) cells with a record-high conversion efficiency of 21.0%. By applying the alternative diffusion source and the co-diffusion, the number of process steps is reduced and the fabrication process is simplified compared to separately diffused *n*-PERT BJ cells. To further simplify the process, the multifunctional use

of PECVD stacks as diffusion source and also as rear side passivation instead of $\text{AlO}_x/\text{SiN}_y$ is considered. We investigate the passivation quality and the interface passivation mechanism of PECVD BSG layers and reach the lowest published J_0 value for a BSG/ SiN_z passivation stack on a p^+ -emitter of 40 fA/cm^2 . We present a novel cell concept based on n -type Cz-Si named Bifacial Co-diffused Rear Emitter (BiCoRE) cells as an advancement of n -PERT BJ cells. The first BiCoRE cells reach 20.6% efficiency and 78% bifaciality. The BiCoRE process flow and complexity are comparable to industrial screen-printed p -type Passivated Emitter and Rear Cells (PERC) but the n -type silicon substrate that does not suffer from light-induced degradation (LID) allows for stable cell efficiencies. We set up a process simulation model that describes the boron diffusion from the PECVD BSG layer into the silicon and allows to reproduce the experimental boron diffusion profiles obtained during co-diffusion. Device simulations as well as loss and efficiency gain analysis of the co-diffused cells are performed in order to identify recombination loss contributions and potential efficiency gains. The simulations prove the high quality of our PECVD BSG diffusion source.

Keywords:

Plasma enhanced chemical vapor deposition,
Boron silicate glass diffusion source and passivation,
Simplified co-diffused n -type silicon solar cells.

Contents

1	Introduction	9
2	Physical fundamentals	15
2.1	Semiconductor silicon	15
2.1.1	<i>p-n</i> junction and diode	16
2.2	Working principle of a solar cell	17
2.2.1	<i>IV</i> characteristic of an ideal solar cell	17
2.2.2	Loss mechanism in a real solar cell	19
2.3	Bulk recombination	20
2.4	Surface recombination	21
2.4.1	High-quality surface passivation layers	21
2.5	Recombination in a solar cell	23
3	Measurement techniques	25
3.1	Ellipsometry	25
3.2	Four-point probe sheet resistance measurement	26
3.3	Electrochemical capacitance-voltage doping profile measurement	27
3.4	Plasma profiling time of flight mass spectrometry	28
3.5	Photoconductance lifetime measurement	29
3.6	Corona charge analysis	30
4	Plasma deposition and diffusion	33
4.1	Plasma-enhanced chemical vapor deposition	33
4.2	Boron and phosphorus furnace diffusions	35
4.3	Co-diffusion of boron and phosphorus	36
4.4	Sample preparation	38

5	Optimization of PECVD diffusion sources	41
5.1	Properties of PECVD layers	42
5.1.1	Undoped PECVD oxynitride	42
5.1.2	PECVD boron silicate glass	46
5.2	Boron diffusion from PECVD BSG and co-diffusion	49
5.2.1	Impact of the PECVD gas flow ratios	50
5.2.2	Impact of the PECVD BSG layer thickness	57
5.2.3	Impact of co-diffusion parameters and capping layers	60
5.2.4	Impact of the silicon surface morphology	63
5.2.5	Boron-rich layer formation	67
5.3	Passivation quality of PECVD BSG	68
5.3.1	Interface passivation mechanism	70
6	Fabrication and characterization of solar cells	75
6.1	Co-diffused front junction cells	76
6.1.1	<i>n</i> -PERT FJ solar cells	76
6.2	Co-diffused back junction cells	81
6.2.1	<i>n</i> -PERT BJ solar cells	81
6.2.2	<i>n</i> -PERT BJ module	86
6.2.3	Simplified BJBC cells	87
6.2.4	BiCoRE solar cells	91
6.2.5	UV stability of BiCoRE solar cells	96
7	Process and device simulations	101
7.1	Simulation of boron diffusion profiles	101
7.2	Device simulations	104
7.2.1	Free energy loss analysis	105
7.2.2	Synergistic energy gain analysis	107
8	Summary and outlook	109
8.1	Summary	109
8.2	Outlook	111
9	Appendix	113
9.1	Abbreviations and symbols	114
9.2	References	118
9.3	List of publications	126
9.4	Acknowledgement	128

Chapter 1

Introduction

The success story of the direct conversion of solar energy into electrical power started in 1839 when Alexandre Edmond Becquerel discovered the photoelectric effect. Over 100 years later, after the beginning of the semiconductor era, in 1954 Chapin demonstrated the first solar cell that was based on crystalline silicon and reached a conversion efficiency of 6% [Go98, 1.2].

Henceforward, different solar cell concepts and semiconductor materials were investigated and the conversion efficiency and module power was steeply increased. The cell and module development and production was moved from small labs to a growing photovoltaic industry.

A variety of silicon solar cell concepts with the aim of both a high conversion efficiency and a simple process flow for cost and time efficient industrial fabrication have been developed during the last decades. The most common industrial cell concept is the aluminum back surface field (Al-BSF) cell that applies screen-printed silver (Ag) front and Al rear contacts. The Al-BSF cells use crystalline p -type silicon wafers as base material and a phosphorus diffusion to form the front side emitter. During firing, a full-area Al- p^+ -BSF is formed. The Al-BSF cells, as shown in Fig. 1.1 (top), reach efficiencies of about 18% [Du12] and with currently improved screen-print metallization up to 19.9% [Ch16].

Nowadays, the Passivated Emitter and Rear Cell (PERC) concept based on p -type silicon wafers is expected to become a major industrial solar cell technology [IT16]. This cell type applies dielectric layers to improve

the surface passivation and the optical properties both at the front and rear side and thus reducing electrical and optical losses that limit the Al-BSF cell efficiencies. The Al- p^+ -BSF is formed only locally where laser contact openings (LCO) of the dielectric layers are applied, thus recombination losses are reduced. With a lean process flow, record efficiencies of 21.2% in 2014 [Ha14] and, currently, of 22.13% [Ye16] were demonstrated.

However, the efficiency of PERC solar cells typically decreases around 0.5%_{abs.} due to light-induced degradation (LID) of the boron-doped p -type Czochralski-grown silicon (Cz-Si) used as base material [Du13]. Different approaches have been developed to reduce or avoid the degradation of p -type silicon, but additional thermal treatments are required [Sc04]. Monocrystalline n -type Cz-Si is in general more insensitive to metal impurities than p -type silicon and thus allows for high stable lifetimes and high cell efficiencies [Sc07].

Consequently, cell concepts using n -type Cz-Si substrates and applying a boron emitter have been developed. One of these concepts is the Passivated Emitter and Rear, Rear Totally doped (PERT) cell in back junction (BJ) configuration which is an n^+np^+ device [Me13]. The n -type PERT (n -PERT) BJ cell has a similar structure and process flow as the p -type PERC (p -PERC) cell in front junction (FJ) configuration (an n^+pp^+ device) as shown in Fig. 1.1. The main difference between the two cell concepts is the n -type substrate and the full-area boron diffusion at the rear of the PERT BJ cell, which acts as the emitter. In laboratory-scale processing, this emitter is commonly formed during a BBr_3 furnace diffusion which is followed by the deposition of a dielectric layer. This layer protects the emitter during the following front-side texturing and $POCl_3$ -diffusion to form the n^+ -front surface field (FSF). Thus, two additional process steps are needed.

Until now, n -PERT BJ cells applying BBr_3 and $POCl_3$ furnace diffusions have demonstrated conversion efficiencies up to 22.5% using Ni/Cu/Ag plating for metallization [Ur15] and with all-screen-printed contacts up to 21.8% [Bo16]. For n -PERT cells compared to PERC cells, due to the boron diffusion, an additional high-temperature step is needed that is both cost- and time-intensive. Therefore, alternative diffusion sources are investigated with the aim of process simplification. High-efficiency n -type

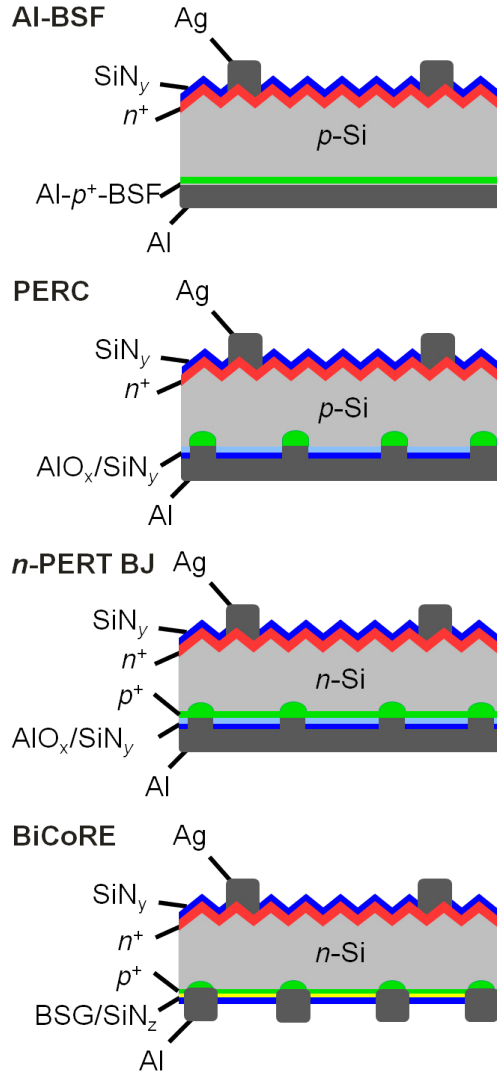


Figure 1.1: Schematic diagrams of the screen-printed solar cell concepts Al-BSF, p -PERC, n -PERT BJ and n -BiCoRE. The efficiencies are improved with the evolution from the simple Al-BSF to the industrial PERC cells, but the process complexity is increased. With the n -type PERT BJ and BiCoRE cells, the efficiency potential is further increased but a simplified processing allows to keep the complexity and thus production time and costs low.

solar cells with a process complexity comparable to that of p -PERC cells shall be achieved so that an easy integration into existing PERC production lines is possible.

In this work, we optimize and apply the plasma-enhanced chemical vapor deposition (PECVD) of boron silicate glass (BSG) which is used as a single-sided solid diffusion source. We apply a POCl_3 co-diffusion process to form both the boron p^+ -rear side emitter and the phosphorus n^+ -front surface field (FSF) in a single high-temperature process. First, we investigate optimum parameter settings for the deposition of undoped PECVD layers and BSG layers on test structures. We perform the boron drive-in at temperatures of 900 °C to 1000 °C and characterize the resulting boron diffusions. Next, we develop a two-stage POCl_3 co-diffusion with a boron drive-in step in nitrogen ambient followed by a POCl_3 diffusion at about 830 °C. As a phosphorus diffusion barrier and as protection layer during chemical cleaning and texturing steps, a PECVD capping layer needs to be applied on top of the BSG layer. As an approach for process simplification, CVD BSG layers combined with a POCl_3 co-diffusion have already been applied to n -PERT solar cells (front and back junction) [Ro14, Fr14, Ca14] reaching conversion efficiencies up to 20.1% for bifacial devices [Ca14]. We demonstrate monofacial n -PERT BJ cells with a record-high conversion efficiency of 21.0% with a co-diffused boron emitter from a PECVD BSG/ SiN_z stack.

To further simplify the process, the multifunctional use of PECVD stacks as diffusion source and also as rear side passivation instead of $\text{AlO}_x/\text{SiN}_y$ has been proposed and saturation current densities J_0 down to 50 fA/cm² have been demonstrated for a BSG/ SiN_x passivation on test structures by Engelhardt et al. [En15]. In this work, we investigate the passivation quality of PECVD BSG layers capped with SiN_z reaching the lowest published J_0 result of 40 fA/cm² and integrate it into the fabrication of bifacial n -type cells. We present a cell concept based on n -type Cz-Si named bifacial co-diffused rear emitter (BiCoRE) cells as an advancement of n -PERT BJ cells. BiCoRE cells, as shown in Fig. 1.1 (bottom), have a screen-printed Al grid on the rear side to obtain bifaciality. A PECVD BSG/ SiN_z diffusion source is applied that is not removed after co-diffusion but remains on the rear side emitter as a passivation layer

and also as anti-reflective coating (ARC). We demonstrate 20.6% efficient BiCoRE cells with a significantly reduced number of process steps compared to separately diffused PERT cells.

Thus, applying our optimized PECVD diffusion sources and co-diffusion process, simplified n -type silicon solar cells can be fabricated with a comparable process complexity as industrial p -PERC cells but with high LID stable lifetimes and cell efficiencies.

Chapter 2

Physical fundamentals

2.1 Semiconductor silicon

The predominant material used today in the industrial production of solar cells is silicon (Si), thus its properties shall briefly be described. Silicon is a semiconductor that is defined as a crystalline solid which acts as an insulator at temperatures approaching 0 K but otherwise has an electronic conductivity higher than that of insulators and lower than the conductivity of metals [Go98, 3.1]. Silicon is an element of the fourth group of the periodic table and thus exhibits four valence electrons. The Si atoms form covalent bonds and arrange in the periodic crystal structure of a diamond lattice.

An electronic conductivity can only be reached when some of the bonds are broken and electrons are moved from a state of low energy within the valence band (valence band edge E_v) to a higher energy level in the conduction band (conduction band edge E_c), leaving an empty state that is called defect electron or hole. Therefore, the band gap needs to be overcome by transferring an energy $E \geq E_g = E_c - E_v$ to an electron in the valence band. For semiconductors, E_g is small compared to insulators, so that an electronic conductivity is observed at room temperature. For silicon, the gap energy E_g at 300 K is 1.124 eV [Go98, 3.1.4]. The number of free charge carriers is controlled by the temperature. At 300 K, an intrinsic carrier density of $n_i = 1.08 \times 10^{10} \text{ cm}^{-3}$ has been extracted in [Go98, 3.1.4]. From that, the electron concentration n and the hole con-

centration p are calculated according to $n \cdot p = n_i^2$. The conductivity σ of a semiconductor is $\sigma = q \cdot (n \cdot \mu_n + p \cdot \mu_p)$ with the elementary charge q and the mobility of electrons μ_n and of holes μ_p . For intrinsic silicon, the resistivity $\rho = 1/\sigma$ at 300 K is about 300 k Ω cm. More details about the band structure of intrinsic semiconductors, the occupation of energy levels and the conduction mechanisms can be found in [Go98, 3.1].

The conductivity of a semiconductor can strongly be influenced by changing the concentration of charge carriers. Therefore, impurity atoms can be introduced into the crystal structure which is called doping. Atoms from the fifth group of the periodic table, such as phosphorus (P), are called donors because they donate conduction electrons. The semiconductor is denoted as an n -type conductor in which the electrons are the majority charge carriers and the holes are the minority charge carriers. Impurity atoms from the third group, such as boron (B), are called acceptors and due to the presence of holes, the hole conductivity is increased so that the semiconductor is called a p -type conductor.

2.1.1 p - n junction and diode

When an n -type doped and a p -type doped region are merged within the same silicon crystal lattice, this is called a p - n junction. At the junction, diffusion currents arise: The electrons from the n -region diffuse into the p -region and the holes diffuse from the p -area into the n -region, the ionised acceptors and donors are left as fixed space charges. In the space charge region, an electric field is generated that compensates the diffusion flow.

A diode is an electrical device that is based on a p - n junction and that controls a current flow in dependence of an applied voltage: When an electrical voltage is applied with the positive terminal to the p -region, with increasing voltage the width of the space charge region and its resistance is decreased and an increasing forward bias current flows. For a reverse voltage, the space charge region becomes wider and its resistance grows so that the current is blocked. There is only a small reverse leakage current that reaches a constant value and that is called the saturation current I_0 of the diode [Go98, 4].

2.2 Working principle of a solar cell

A solar cell is a device that converts solar energy into electrical energy by utilizing the internal photoelectric effect. Basically, a solar cell is an illuminated silicon crystal with a p - n junction and with metal contacts in order to extract the generated current.

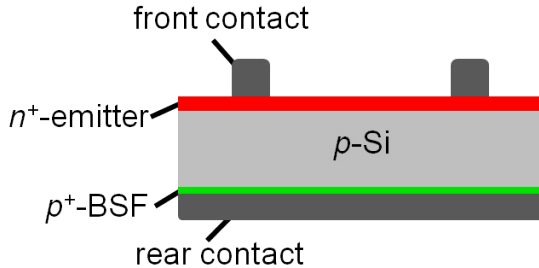


Figure 2.1: Schematic diagram of a simple silicon solar cell with a p -type base, n -type front side emitter and p -type BSF and metal contacts.

A simple solar cell structure is shown in Fig. 2.1. As the base material, p -type silicon is used. The n -type doping is typically introduced by a furnace diffusion process and the shallow highly doped n^+ -region is called emitter. When the cell is illuminated from the emitter side, charge carrier pairs are generated. If the electrons and holes are generated in the active area of the solar cell, that is in the space charge region and predominantly the p -Si base, a voltage V builds up at the contacts. When the front and rear side metal contacts are connected via an electrical load, electrons can be extracted at the emitter contacts and a current I flows through the external load. The holes are transported to the base contact through the back surface field (BSF). The BSF is a p -type doped region with an increased doping compared to the base indicated by p^+ , and thus an increased conductivity for holes.

2.2.1 IV characteristic of an ideal solar cell

The current-voltage (IV) characteristic of an ideal illuminated solar cell is shown in Fig. 2.2. Compared to an unilluminated solar cell, that is a

diode, the IV -curve is shifted along the I -axis.

For $V=0$ the maximum current, called short-circuit current I_{sc} , is reached that has a theoretical limit of 44 mA cm^{-2} for an ideal silicon cell [Go98, 5.1.1].

The IV characteristic of an ideal solar cell can be described by the one-diode equation:

$$I = I_0 \cdot \left(e^{\frac{V \cdot q}{kT}} - 1 \right) - I_{sc} \quad (2.1)$$

with the saturation current I_0 , the Boltzman constant k and the temperature T .

When there is no current flow, the open circuit voltage V_{oc} is obtained. From equation 2.1 in the case of $I=0$, V_{oc} can be approximated by:

$$V_{oc} = \frac{k \cdot T}{q} \cdot \ln \left(\frac{I_{sc}}{I_0} \right). \quad (2.2)$$

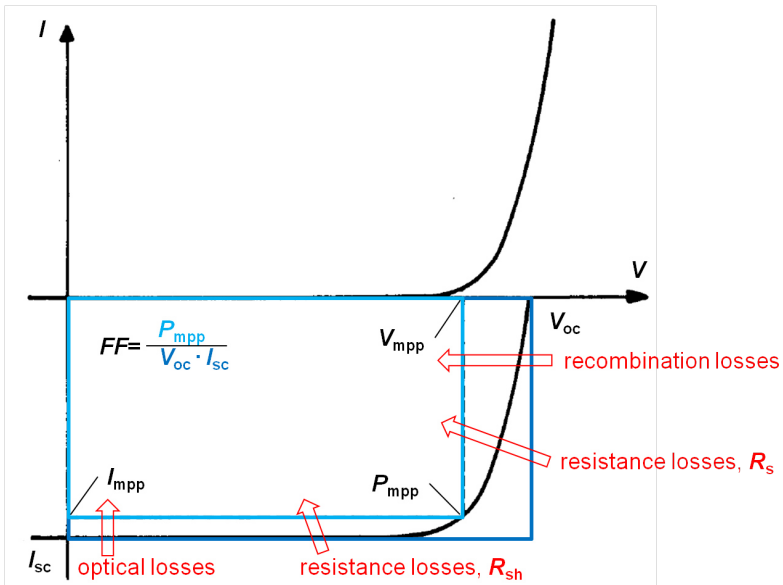


Figure 2.2: Illuminated and dark IV characteristics of an ideal solar cell. In a real solar cell, the power output and the fill factor FF might be reduced from different loss mechanism.

The solar cell has an optimal operating point at which the maximum power output $P_{mpp} = V_{mpp} \cdot I_{mpp}$ is reached. The ratio of the maximum power and the product of $V_{oc} \cdot I_{sc}$ is defined as the fill factor $FF = \frac{V_{mpp} \cdot I_{mpp}}{I_{sc} \cdot V_{oc}}$. FF corresponds to the ratio of the rectangular areas beneath the IV -curve, as indicated in Fig. 2.2, and has a typical value of 0.75-0.85 [Go98, 5.1.1].

The solar cell parameter of most interest is the conversion efficiency η that is defined as the ratio of the generated electric power at maximum power point P_{mpp} and the irradiated power P_{light} :

$$\eta = \frac{P_{mpp}}{P_{light}} = \frac{FF \cdot I_{sc} \cdot V_{oc}}{P_{light}}. \quad (2.3)$$

The theoretical efficiency limit for an ideal silicon solar cell is 29%, given by the detailed balance limit [Sh61].

2.2.2 Loss mechanism in a real solar cell

In a real solar cell, different loss mechanism lead to power losses and thus reduce the fill factor, as indicated in Fig. 2.2. In order to achieve high-efficiency solar cells, the amount of total loss arising from optical, resistance and recombination loss contributions needs to be reduced [Go98, 6.1].

Optical losses arise from reflection and shadowing of the incoming light and lead to a reduced I_{sc} . Optical losses can be minimized by applying textured surfaces and anti-reflective coating (ARC) layers for reduced reflection and improved light-harvesting as well as a low metallization fraction for reduced shadowing.

The resistance losses are described by the series resistance R_s and the shunt resistance R_{sh} . R_s comprises contact resistances from the metal to the semiconductor as well as ohmic resistances within the metal contacts and the silicon. R_{sh} arises from leaking currents at the edges of the solar cell as well as interruptions of the p - n junction that might be caused by an insufficient emitter diffusion. R_{sh} is also lowered, if a short circuit caused by an electrical contact of the base and the metallization occurs [Go98, 5.2.3]. Thus, optimum contact and emitter formation are necessary in order to reduce resistance losses in a real solar cell and to achieve high

efficiencies.

The loss mechanism of main interest in solar cell physics is the recombination loss. Recombination of the photogenerated charge carriers may occur in the silicon bulk, at the surfaces and in the diffused regions of a silicon solar cell, as discussed in more detail in the following Sections. Recombination losses reduce the current I_{sc} and most of all the voltage V_{oc} of a real solar cell. High-quality bulk material, emitter and BSF regions and surface passivation layers are applied in order to keep recombination losses as low as possible.

2.3 Bulk recombination

Pairs of quasi-free electrons and holes can be generated in the silicon bulk by absorption of light and transferring energy from photons to electron-hole pairs, lifting the electrons to the conduction band. The annihilation of these generated electron-hole pairs is called recombination.

One type of recombination is the radiative recombination, which is the inverse process to absorption. When one electron from the conduction band recombines with one hole in the valence band, an energy that corresponds approximately to the band gap energy E_g is released and a photon with the energy $E = h \cdot \nu$ and thus with the wavelength $\lambda = h \cdot c / E_g$ is emitted (h : Plancks constant, ν : photon frequency, c : speed of light). In silicon, the radiative recombination is an unlikely process because Si is an indirect semiconductor, so that both photons and phonons are involved in the recombination and the absorption processes. Thus the radiative lifetime τ_{rad} is large and is usually not limiting the charge carrier recombination lifetime in the silicon bulk. [Go98, 3.4.1].

During Auger recombination, energy is transferred from one recombining electron to another electron that is thus excited. The electron loses the additional energy during lattice collisions and returns to the initial energy level. The recombination rate R_{Aug} for electrons is proportional to $n^2 p$ because three particles are involved. The Auger lifetime τ_{Aug} , that is proportional to the inverse of the recombination rate, decreases with increasing doping concentration [Go98, 3.4.2].

The most important recombination mechanism in silicon, that is based on impurities and defects in the silicon crystal, is called the Shockley-Read-Hall (SRH) recombination. The presence of impurity atoms and crystal defects cause energy levels that are traps for charge carriers and determine their recombination lifetime τ_{SRH} [Go98, 3.4.3].

The types of recombination that take place in the silicon bulk are summarized in the bulk lifetime τ_{bulk} as follows:

$$\frac{1}{\tau_{bulk}} = \frac{1}{\tau_{rad}} + \frac{1}{\tau_{Aug}} + \frac{1}{\tau_{SRH}}. \quad (2.4)$$

In silicon, radiative recombination is negligible. τ_{bulk} is mainly limited by SRH recombination, but the Auger recombination, that is strongly dependent on the dopant concentration, becomes the dominant recombination mechanism at high doping levels $>10^{18} \text{ cm}^{-3}$ [Go98, 3.4.4].

2.4 Surface recombination

The abrupt interruption of the crystal structure at an uncapped silicon surface results in a high density of defect states of about 10^{15} cm^{-2} that act as traps and lead to a high recombination rate [Go98, 6.2.1.1.2].

The surface recombination is characterized by the effective surface recombination velocity S_{eff} . For a silicon wafer with the wafer thickness W and with symmetrical front and rear surfaces, an effective lifetime τ_{eff} combines bulk and surface recombination. If the wafer is symmetrically passivated with a high-quality passivation, leading to low S_{eff} values, the following approximation is valid [Si06]:

$$\frac{1}{\tau_{eff}} = \frac{1}{\tau_{bulk}} + \frac{2 \cdot S_{eff}}{W}. \quad (2.5)$$

2.4.1 High-quality surface passivation layers

Surface passivation layers are applied in order to minimize recombination of charge carriers at the silicon surface of a solar cell. A high-quality passivation aims for low interface state densities of $D_{it} < 10^{11} \text{ cm}^{-2}$ and low

effective recombination velocities $S_{eff} < 100 \text{ cm s}^{-1}$ [Go98, 6.2.1.1.2]. Thus the photogenerated current and the open-circuit voltage of solar cells can be enhanced [Ma03, Iib.2.5].

Different types of layers and deposition methods are used, based on different passivation mechanism. For a chemical passivation, free Si valences that are called “dangling bonds” are saturated. By hydrogen passivation, stable compounds such as SiH and SiOH are formed. Thus, the interface density of states D_{it} can be reduced. An electrical passivation by means of field effect occurs when a layer contains positive or negative fixed charges with a density Q_f so that the concentration of one type of charge carrier is reduced and the overall surface recombination is reduced.

Excellent passivation results in solar cell fabrication are achieved by applying a silicon dioxide (SiO_2) layer that can be grown during a high temperature oxidation in a furnace process (thermal oxide) [Ma03, Iib.2.5] or by means of CVD at lower temperatures $<400 \text{ }^\circ\text{C}$. The SiO_2 layer saturates the traps at the silicon surface. With an additional annealing, very low interface state densities $D_{it} = 10^{10} - 10^{11} \text{ cm}^{-2}$ and effective recombination velocities $S_{eff} = 10 - 100 \text{ cm s}^{-1}$ can be achieved [Go98, 6.2.1.1.2]. For thermally grown oxides, positive fixed charge densities Q_f of $+1 \times 10^{10} \text{ cm}^{-2}$ to $+2 \times 10^{11} \text{ cm}^{-2}$ are reported [WT86].

The deposition of a silicon nitride SiN_x layer by means of PECVD at about $400 \text{ }^\circ\text{C}$ can reduce the surface recombination velocity effectively. It is often applied on an n^+ -diffused textured silicon surface - as a single layer or on top of a thin oxide layer - and acts both as passivation layer and as antireflective coating. To achieve a good surface and bulk passivation, generally a thermal treatment of the SiN_x is necessary as it takes place during the solar cell processing step of contact firing [Ma03, Iib.2.5]. Due to the high hydrogen content of 10-15%_{at} of SiN_x , hydrogen atoms diffuse to the silicon surface and effectively passivate dangling Si bonds [Sc09].

The SiN_x passivation quality is dependent on the precursor gases used during PECVD, the doping of the substrate wafer and the injection level. Low surface recombination velocities S_{eff} have been demonstrated for both silicon-rich SiN_x with a refractive index $n > 2.3$ (measured at $\lambda = 632 \text{ nm}$) using pure SiH_4 and NH_3 , for stoichiometric SiN ($n = 1.95$) using di-

lute SiH_4 and NH_4 and for very silicon-rich SiN_x ($n > 2.8$) using SiH_4 , N_2 and H_2 on p -type silicon with a resistivity of 1-2 Ωcm [KC02, 1]. S_{eff} values of 1-10 cm s^{-1} have been measured on n -type Si that are decreased with increasing resistivity and decreasing injection level. On p -type Si, recombination velocities of $S_{eff} = 2-34 \text{ cm s}^{-1}$ are determined that are also decreased with increasing resistivity [KC02, 2.2]. SiN_x layers have a high positive fixed charge density leading to a field-effect passivation for both n - and p -type substrate wafers. At the surface of an n -type wafer electrons are accumulated while the surface of a (low doped) p -type wafer is inverted and a space-charge region is formed [KC02, 2.3].

Aluminium oxide (AlO_x) deposited by atomic layer deposition (ALD) or PECVD shows a high chemical and electrical passivation quality. Negative charges are included in AlO_x layers allowing for an effective field-effect passivation. A high fixed charge density of $Q_f = -(4 \pm 1) \times 10^{12} \text{ cm}^{-2}$ and a low interface state density of $D_{it} = 1 - 3 \times 10^{11} \text{ eV}^{-1} \text{ cm}^{-1}$ are measured in [We14, 8] allowing for recombination velocities $S_{eff} < 100 \text{ cm s}^{-1}$ for only 1 nm thin AlO_x layers on p -type Si and down to 1 cm s^{-1} for 10 nm AlO_x layer thickness on n -type Si. For ultrathin AlO_x layers deposited on p -type silicon, low $S_{eff} < 22 \text{ cm s}^{-1}$ can be obtained after a firing step. The thermal stability and passivation quality is further improved by depositing a PECVD SiN_x capping layer due to hydrogenation of interface states during firing [Sc09].

2.5 Recombination in a solar cell

In the diffused regions of a solar cell, that is in the emitter and the BSF, the three types of recombination Auger, SRH and surface recombination occur. These recombination mechanisms are summarized and the recombination in the highly-doped emitter and BSF regions and at its surfaces is described by the saturation current density J_0 . J_0 is increased for higher doping concentrations due to stronger Auger recombination. By applying passivation layers on the emitter and BSF regions, the surface recombination and thus the J_0 value can be reduced. Thus, in order to reach high solar cell efficiencies, the doping profiles of the emitter and BSF regions

as well as the surface passivation layers need to be optimized aiming for low J_0 results.

For a silicon solar cell with a passivated front side emitter and BSF, the effective lifetime is expressed as:

$$\frac{1}{\tau_{eff}} = \frac{1}{\tau_{bulk}} + \frac{J_{0,e} \cdot (N_{dop} + \Delta n)}{q \cdot n_i^2 \cdot W} + \frac{J_{0,BSF} \cdot (N_{dop} + \Delta n)}{q \cdot n_i^2 \cdot W} \quad (2.6)$$

with the emitter saturation current density $J_{0,e}$, the BSF saturation current density $J_{0,BSF}$ and the substrate dopant density N_{dop} [Si06].

For solar cell characterization, the effective lifetime τ_{eff} of unmetallized cell precursors and of symmetrically diffused and passivated test samples is measured and the saturation current density J_0 as well as the implied open-circuit voltage $V_{oc,impl}$ are extracted as will be described in 3.5.

Chapter 3

Measurement techniques

This Chapter describes different measurement techniques for the optical and electrical characterization of test structures. Thickness measurements of dielectric layers are performed by ellipsometry measurements. Boron and Phosphorus diffusions are characterized by measuring the sheet resistance by means of four-point probe (FPP). Depth-dependent doping profiles are determined by electrochemical capacitance-voltage (ECV) and plasma profiling time of flight mass spectrometry (PP-TOFMS) measurements. For the characterization of the surface passivation quality, carrier lifetimes and saturation current densities are derived from quasi steady state photoconductance (QSSPC) measurements that can be performed in dependence of applied charges during a corona charge analysis.

3.1 Ellipsometry

For the characterisation of dielectric layers deposited on planar Si substrates, monochromatic ellipsometry measurements at a single wavelength or spectral ellipsometry measurements can be performed. Thus, the optical properties such as thickness d and refractive index n of a single layer or a layer stack can be determined.

For a fast determination of d and n of a PECVD layer, in order to control the deposition parameters, a single monochromatic measurement is performed using a monochromatic ellipsometer (Plasmos SD2300). A beam of polarized laser light with a wavelength of 632 nm (He-Ne laser, 1 mW,

continuous wave) is directed on the sample and the reflected light beam is detected, passing an analyser. By measuring its polarisation condition, the values of d and n can be calculated. Details of the measurement theory can be found in [Sr98, 9.3].

For a detailed characterisation of a layer or a layer system, a spectroscopic ellipsometer (Woollam M-2000UI) is used. Typically, three measurements are performed at different angles of incidence from 50° to 70° . An effective medium approximation (EMA) model containing the optical properties of different layers such as Si, SiO_2 , SiN_z is set up and by fitting the experimental data, the properties of the layers of interest are extracted.

3.2 Four-point probe sheet resistance measurement

The distribution of the sheet resistance R_{sheet} of a boron or phosphorus diffusion can be measured on a Si substrate wafer after removal of all dielectric layers by means of a four-point probe (FPP) wafer tester (Polytec 4Dimensions). An average R_{sheet} value for one $15.6 \times 15.6 \text{ cm}^2$ wafer and the corresponding standard deviation is determined from 121 measurement points. It is important to note that only p - n junctions can be measured, that is B diffusions should be measured on n -type substrates.

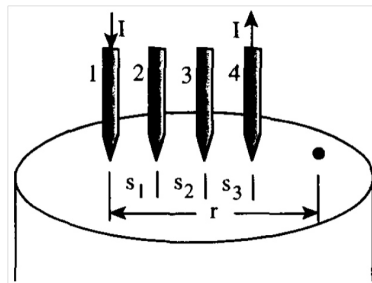


Figure 3.1: Four-point probe measurement setup. The four probes are arranged in-line and have an equal spacing $s_1 = s_2 = s_3 = s$. For the measurement of a sheet resistance R_{sheet} of a thin silicon sample, a current I is supplied through the outer probes and the voltage U is measured at the inner probes [Sr98, 1.2].

Using the advantageous FPP method, four contact needles are positioned on the sample surface, as shown in Fig. 3.1. A current is supplied through the outer electrodes and by measuring the resulting voltage drop using the inner electrodes, the sheet resistance is calculated according to:

$$R_{sheet} = \frac{\pi}{\ln 2} \frac{U}{I}. \quad (3.1)$$

Equation 3.1 is valid for the assumption of a thin and wide surface compared to the spacing of the needles. By using four probes instead of two and thus separating the current and voltage electrodes, the influence of contact resistances is eliminated. Details of the measurement theory can be found in [Sr98, 1.2].

3.3 Electrochemical capacitance-voltage doping profile measurement

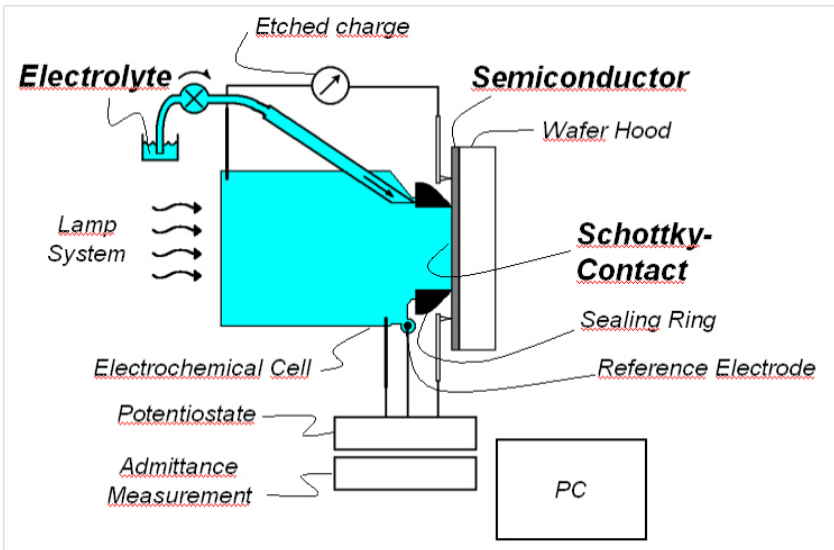


Figure 3.2: ECV measurement setup for the electrochemical etching of semiconductors and extracting depth-dependent carrier concentrations from CV measurements [WP03].

Doping profiles of B and P diffusions can be measured by electrochemical capacitance-voltage measurements (ECV) (Wafer Profiler CVP21). A Schottky contact is formed between the Si sample and an electrolyte contained in an electrochemical cell, as shown in Fig. 3.2. In subsequent steps, the carrier concentration at the surface is determined by applying an external voltage and measuring the capacitance. The Si is etched by the electrolyte and the etched depth is calculated from the measured electric charge. Thus a depth-dependent concentration profile of the electrically active dopants is attained [WP03].

3.4 Plasma profiling time of flight mass spectrometry

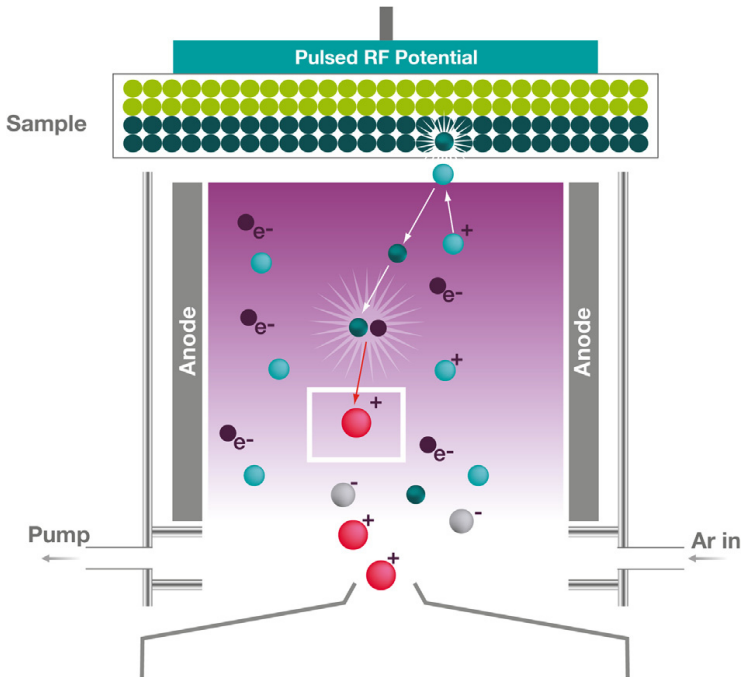


Figure 3.3: Principle of the PP-TOFMS analysis for depth profiling of elements in nanometer scale structures [Te14].

Plasma profiling time of flight mass spectrometry (PP-TOFMS) is a technique for depth profile analysis down to the nanometer scale for solid surfaces and thin films. It allows us to determine the dopant concentrations both in the diffusion source after PECVD and in the Si substrate after diffusion. Figure 3.3 shows the working principle of this measurement technique: A glow discharge plasma is created in an ultra pure argon (Ar) environment. The created Ar ions are used for sputtering the surface of a specimen and in a time of flight mass spectrometer, the sputtered species ionized by the plasma are collected and analysed. Further details of the measurement technique can be found in [Te14].

3.5 Photoconductance lifetime measurement

The photoconductance lifetime tester (WCT-120, Sinton Instruments) is used to measure lifetimes τ and to extract saturation current densities J_0 and implied open-circuit voltages V_{oc} of unmetallized passivated samples as well as to inductively determine sheet resistances of diffusions. Thus, the quality of emitter and BSF regions as well as the surface passivations of these highly-doped regions, that are applied during solar cell fabrication, can be evaluated.

The quasi steady state photoconductance (QSSPC) measurement is applied for samples with an expected lifetime lower than $200 \mu\text{s}$. A sample is illuminated by a slowly decaying pulse of light. Simultaneously, the light intensity is detected by a light sensor and the conductance of the sample is measured by a coil that is inductively coupled to the sample. For each moment in time, the excess carrier density Δn is calculated from the measured conductance and the generation rate of electron-hole pairs G is derived from the measured intensity. Thus, the lifetime is calculated from the steady-state condition $\Delta n = G \cdot \tau$ and plotted as a function of the excess carrier density Δn .

For samples with a high lifetime of more than $\approx 100 \mu\text{s}$, the transient photoconductance decay (PCD) method is applied. A short pulse of light is used and after illumination, the decay of the conductance is measured as a function of time. The excess carrier density Δn and its derivative are calculated and the lifetime is derived from $\tau = -\Delta n / (d\Delta n / dt)$ [Si06].

For J_0 measurements, the lifetime measurement results are evaluated by the Kane & Swanson method [Ka85] at an excess carrier density Δn that corresponds to ≈ 10 times the wafer doping concentration N_{dop} . For example, an excess carrier density of $9 \times 10^{15} \text{ cm}^{-3}$ is applied for the J_0 evaluation of a $5 \Omega \text{ cm}$ n -type Cz-Si wafer. An effective intrinsic carrier concentration of Si of $n_{i,eff} = 8.6 \times 10^9 \text{ cm}^{-3}$ is used that is calculated for a temperature of $25 \text{ }^\circ\text{C}$ corresponding to [Al03]. The J_0 samples are symmetrically diffused, passivated and typically measured before and after firing.

For symmetrical J_0 samples, from equation 2.6, the effective lifetime τ_{eff} that is derived from QSSPC measurements is:

$$\frac{1}{\tau_{eff}} = \frac{1}{\tau_{bulk}} + \frac{2 \cdot J_0 \cdot (N_{dop} + \Delta n)}{q \cdot n_i^2 \cdot W}. \quad (3.2)$$

From the slope of the inverse lifetime $1/\tau_{eff}$ as a function of the excess carrier density Δn , J_0 is calculated.

The implied open-circuit voltage $V_{oc,impl}$ is evaluated at a light intensity of 1 sun by the following equation:

$$V_{oc,impl} = \frac{kT}{q} \ln \left(\frac{np}{n_i^2} \right) \quad (3.3)$$

with the total electron concentration n and the total hole concentration p . For an n -type silicon wafer, $n = N_{dop} + \Delta n$ and $p = \Delta n$ [Si06].

3.6 Corona charge analysis

For the characterization of passivation layers, a corona charge analysis as described in more detail in [We14, 3.4] is performed that allows to extract the fixed charge density Q_f within a dielectric passivation layer by measuring the effective lifetime τ_{eff} of a passivated sample and calculating the effective surface recombination velocity S_{eff} as a function of deposited charge.

The samples are charged in a corona chamber with either positive or negative charge at a voltage of $\pm 7\text{-}8 \text{ kV}$ with increasing charging steps that

are assumed to be constant and to have a value of $\Delta Q_{corona} = \pm(4.54 \pm 0.003) \times 10^{11} \text{ cm}^{-2}$. After each charging step, measurements of the Kelvin voltage U_K are performed with a Kelvin probe setup (TREK 320 C) using the vibrating capacitor method [No02]. QSSPC measurements are performed from which the corresponding lifetime τ_{eff} is extracted. The corona charge is removed from a sample by cleaning it in DI water before the complementary charge is applied.

From the measured Kelvin voltage U_K , the deposited charge density Q_{corona} can be calculated from the equation of a parallel plate capacitor as follows:

$$Q_{corona} = C \cdot U_K = \frac{\epsilon_0 \cdot \epsilon \cdot U_K}{q \cdot d} \quad (3.4)$$

with the capacitance C , the dielectric constant ϵ_0 , the permittivity ϵ and the thickness d of the dielectric passivation layer.

The effective surface recombination velocity S_{eff} is calculated from the measured effective lifetime τ_{eff} of symmetrically passivated samples by the following equation:

$$S_{eff} = \sqrt{D \cdot \left(\frac{1}{\tau_{eff}} - \frac{1}{\tau_{bulk}} \right)} \cdot \tan \left[\frac{W}{2} \cdot \sqrt{\frac{1}{D} \cdot \left(\frac{1}{\tau_{eff}} - \frac{1}{\tau_{bulk}} \right)} \right] \quad (3.5)$$

with the minority-carrier diffusion coefficient D [Da02].

For samples with a good passivation quality and high lifetimes, a linear approximation of the tangent can be applied so that equation 3.5 is simplified:

$$S_{eff} = \frac{W}{2} \left(\frac{1}{\tau_{eff}} - \frac{1}{\tau_{bulk}} \right). \quad (3.6)$$

This approximation for S_{eff} , that is independent on the diffusivity and similar to equation 2.5, is valid for recombination velocities below about 250 cm s^{-1} at a typical wafer thickness of about $300 \mu\text{m}$ and a diffusion coefficient of about $30 \text{ cm}^2 \text{ s}^{-1}$ [Sc98, 3.2.1].

If the surface recombination velocity S_{eff} is plotted as a function of the deposited charge density Q , the fixed charge density Q_f of a passivation layer corresponds to the charge density $-Q_{corona}$ at which S_{eff} reaches a maximum value.

In Fig. 3.4, a calculation of a normalized recombination rate at the surface of a passivated $148 \mu\text{m}$ -thick $6.5 \Omega \text{ cm}$ n -type silicon wafer as a function of the deposited charge density $Q = Q_f + Q_{corona}$ is shown. The normalized recombination rate was calculated using the software package PC1D [CI97] from the minority carrier density without taking excess charge carrier generation by external illumination into account, similar to [Ho08].

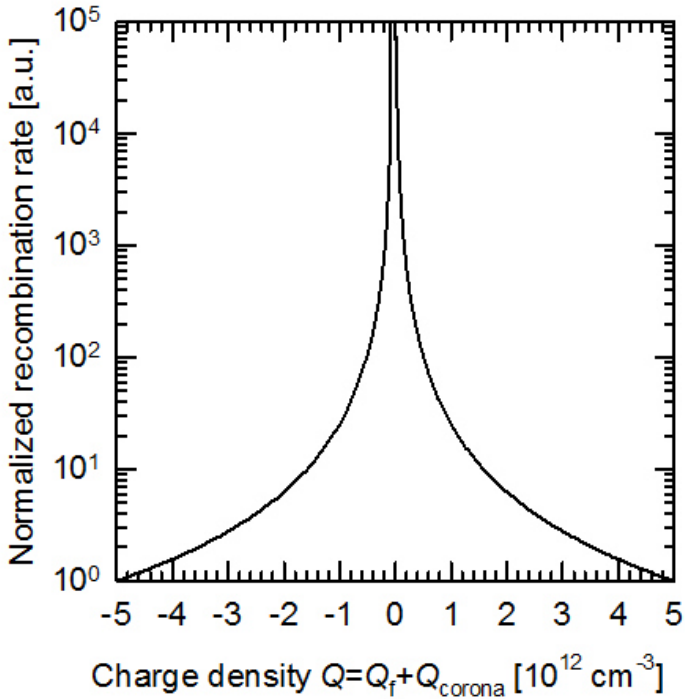


Figure 3.4: Calculation of the normalized recombination rate as a function of the deposited charge density Q , simulated with PC1D [CI97].

The recombination rate, that is proportional to the surface recombination velocity S_{eff} , reaches a maximum when the deposited corona charge balances the fixed charge within the dielectric passivation layer, thus only a chemical passivation of the sample surface is present. With increasing deposited charge density $|Q|$, the recombination rate is decreased due to an increasing level of field-effect passivation.

Chapter 4

Plasma deposition and diffusion

In the following Sections, the working principle of plasma enhanced chemical vapor deposition (PECVD) of dielectric layers is introduced. Standard boron and phosphorus furnace diffusions and co-diffusion processes that apply PECVD diffusion sources are discussed. The preparation of silicon test wafers for the characterization of the deposited layers and diffusions is described.

4.1 Plasma-enhanced chemical vapor deposition

For the fast and efficient deposition of high-quality dielectric layers such as oxides and nitrides as well as amorphous silicon layers, plasma-enhanced chemical vapor deposition (PECVD) is commonly used. A substrate is placed in a deposition chamber under high vacuum conditions (10^{-3} – 10^{-7} mbar). Precursor gases are injected and a plasma with a specific plasma frequency ranging from DC and RF (13.56 MHz) to VHF (30–110 MHz) and Microwave (2.45 GHz) is ignited. In the plasma, the precursor gas is decomposed by electron impact and the resulting ions are deposited on the substrate producing a solid film. The properties and the quality of the layer are determined by the PECVD parameters such as substrate temperature, pressure, plasma power and frequency, deposition time, precursor gases and their gas flows [Ma03, IIc.1.2.1].

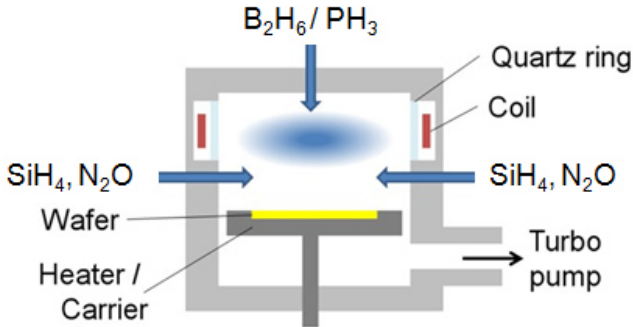


Figure 4.1: Inductively coupled plasma (ICP) source used for the deposition of plasma enhanced chemical vapor deposited (PECVD) boron silicate glass (BSG) layers with the precursor gases SiH_4 , N_2O , and B_2H_6 [DK13].

The deposition of the PECVD layers investigated in this work is performed in a process chamber of a von Ardenne Clustersystem CS 400 P with a 13.56 MHz inductively coupled plasma (ICP) source that is sketched in Fig. 4.1. The advantage of an ICP source compared to a parallel-plate plasma source is a very high plasma density of above 10^{12} cm^{-3} with a dissociation rate of 100% [VAAT]. In our laboratory deposition tool, one $156 \times 156 \text{ mm}^2$ wafer can be locked in, coated and locked out in about 30 min.

For the deposition of undoped oxynitride (SiO_xN_y) and silicon dioxide (SiO_2) layers, the precursor gases silane (SiH_4) and nitrous oxide (N_2O) are used. In order to include dopant atoms, diborane (B_2H_6) or phosphine (PH_3) is added. The resulting layers are boron silicate glasses (BSG) or phosphorus silicate glasses (PSG) that can act as B or P diffusion sources in a following high-temperature treatment. Both diborane and phosphine are diluted: 3% in 97% hydrogen (H_2). In this work, we focus on PECVD BSG solid diffusion sources.

In first experiments, the PECVD parameters are varied in order to find optimal settings for the deposition of undoped SiO_2 , BSG diffusion sources and SiO_xN_y capping layers. The parameter variations will be discussed in 5.1. The temperature of the heater is set constant at $400 \text{ }^\circ\text{C}$ resulting in a substrate temperature of $\leq 200 \text{ }^\circ\text{C}$ and the power is set at 1500 W. The

layer thickness d in the range of about 20 to 300 nm is controlled by the deposition time t . The gas flows and the gas flow ratios of the precursor gases are varied, affecting the composition of the PECVD layer. The total gas flow defines the pressure p during the plasma process that is in the range of $6-8 \times 10^{-3}$ mbar.

For the deposition of PECVD SiN_z layers from the precursor gases silane (SiH_4), ammonia (NH_3) and hydrogen (H_2), the SiNA deposition tool (Meyer Burger) with a microwave plasma source is used [MB16]. In this inline tool, six wafers can be coated single-sided in about 10-20 min, depending on the layer thickness that is controlled by the transit velocity. The refractive index n of the SiN_z layers can be adjusted by changing the precursor gas flows. SiN_z layers with $n=1.9$ and thicknesses of about 50-200 nm that are deposited with a SiH_4 gas flow of about 80 sccm are used as protection layers and act as diffusion and etching barriers. We apply SiN_z as a capping layer on PECVD BSG during co-diffusion. Silicon nitride with a different composition SiN_y is deposited with an increased SiH_4 gas flow of about 125 sccm and has a higher refractive index $n=2.05$. SiN_y is used as a passivation layer on phosphorus-diffused silicon and acts also as anti-reflective coating (ARC) on textured silicon solar cell front sides.

4.2 Boron and phosphorus furnace diffusions

Standard boron and phosphorus diffusions are performed in a quartz-tube furnace by gas phase diffusion using the precursors boron tribromide (BBr_3) and phosphorus oxychloride (POCl_3). B diffusions are typically performed at temperatures of 900-1000 °C, for P diffusions a temperature of about 850 °C is sufficient due to the different diffusion mechanisms of the dopants and the lower activation energy for the diffusion of P atoms in silicon [Go98, 7.2.1].

During a boron gas phase diffusion, a mixed phase B_2O_3 - SiO_2 system that is called boron silicate glass (BSG) with a thickness ≤ 600 nm is grown on the silicon surface. Due to the high boron content, the BSG layer acts as an infinite diffusion source. The boron concentration exceeds the solid solubility of B in Si at the diffusion temperature, so that a Si-B compound

that is called a boron rich layer (BRL) with a thickness of ≤ 80 nm is formed at the silicon surface. A BRL can not be removed in HF after the furnace process and it prevents a good surface passivation. Therefore an in-situ oxidation can be included in a B gas phase diffusion resulting in a high diffusion process duration of about five hours [Ke10].

Alternatively, solid diffusion sources can be deposited on silicon substrates, for example by means of spin-on coating, sputtering or chemical vapour deposition (CVD). Subsequently, a high-temperature treatment is performed to drive-in the dopant atoms. By controlling the dopant content in the solid diffusion source, the resulting doping profile can be tailored. Disadvantages of standard (boron) gas phase diffusions such as high process durations and BRL formation can be prevented.

4.3 Co-diffusion of boron and phosphorus

In this work, co-diffusion processes are investigated: In only one high-temperature treatment two different types of dopants are introduced into silicon wafers forming p^+ - and n^+ -diffusions needed for solar cell fabrication.

One possibility is the single-sided deposition of a solid PECVD BSG diffusion source combined with a gas phase POCl_3 -diffusion in a quartz-tube furnace. For this approach, a two-stage temperature profile is needed, that is sketched in Fig. 4.2: First, at 950°C boron atoms diffuse from the PECVD BSG into the silicon. This step is performed in a POCl_3 furnace tube without POCl_3 gas flow but in nitrogen ambient. Second, after cooling down to 829°C , POCl_3 gas and O_2 are introduced to grow a PSG on the uncovered side of the silicon substrate and to drive-in phosphorus atoms.

P atoms might already diffuse into the silicon from PSG covering the quartz tube during the 950°C step. In order to prevent the indiffusion of P on the BSG covered wafer side, the application of an additional SiN_z or SiO_xN_y capping layer with varying thickness on the PECVD BSG is investigated. The diffusion of P into the unprotected wafer side during the high temperature step can be influenced by the N_2 gas flow that is varied between 1 slm and 10 slm. These influences will be discussed in 5.2.3.

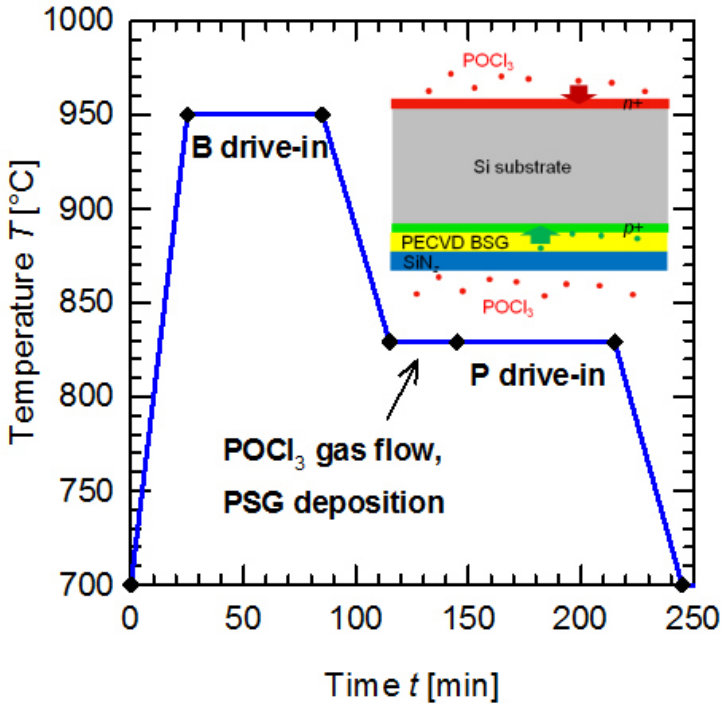


Figure 4.2: Two-stage temperature profile for the POCl_3 -co-diffusion applying a single-sided PECVD BSG diffusion source.

A further possibility for a co-diffusion process is the deposition of a PECVD PSG layer on one wafer side and applying a BBr_3 furnace diffusion. In this case, a single-stage temperature profile at a temperature of 900-1000 °C can be applied. The challenge is to adapt the PSG diffusion source so that the resulting P doping profile has a surface concentration and depth suitable for contacting.

The third option is the deposition of PECVD BSG and PSG diffusion sources on both wafer sides followed by a temperature treatment in N_2 ambient. Here, an independent tailoring of the B and P doping profiles by varying the PECVD deposition parameters is possible.

Considering time and cost efforts, it is favourable to perform one PECVD step and one gas phase co-diffusion with a temperature and duration as low as possible.

In the following, we focus on the deposition of a PECVD BSG diffusion source and the application of a POCl_3 co-diffusion.

4.4 Sample preparation

For the characterisation of PECVD layers and diffusions, different types of silicon test structures are fabricated. The sample preparation always starts with float zone (Fz) or Czochralski grown (Cz) silicon wafers with a (100) orientation that are either p -type doped with boron or n -type doped with phosphorus atoms (other dopants such as gallium are also possible but not considered in this work). The wafers pass through different laser processing, etching and cleaning steps before PECVD and diffusion, depending on the intended characterisation.

Typically, as a first step, labelling and cutting of the samples is performed with a laser system. If Cz-Si wafers are used, they are cleaned in Pura-tron cleaning agent for the removal of slurry after wire sawing. In order to remove crystal damage from sawing and laser damage, the samples are etched in potassium hydroxide (KOH) solution. If a textured silicon surface with random pyramids is needed, an alkaline texture in KOH solution (containing KOH and an additive) is performed. Before entering the PECVD system or the quartz-tube furnace, an RCA cleaning is performed: Ammonia solution (ammonium hydroxide, NH_4OH) with an addition of hydrogen peroxide (H_2O_2) oxidises organic impurities, that are removed in hydrofluoric acid (HF). Next, hydrochloric acid (HCl) with a H_2O_2 addition together with an HF etching step removes metallic impurities [Go98, 7.2.3.1].

For ellipsometry measurements, smooth sample surfaces are needed. Thus, shiny-etched Fz p -type silicon wafers with a resistivity of $(200 \pm 15) \Omega \text{ cm}$ are used. Either one entire wafer with a diameter of 150 mm is used or the wafer is cut into $25 \times 25 \text{ mm}^2$ pieces using a laser system. After laser damage removal and RCA cleaning, the samples are coated single-sided with a PECVD layer.

PECVD layers used as diffusion sources are characterised by the resulting sheet resistances R_{sheet} and saturation current densities J_0 after diffusion. $156 \times 156 \text{ mm}^2$ n -type Cz-Si wafers with a resistivity of 5-6 $\Omega \text{ cm}$ are

labelled, Puratron, KOH and RCA cleaned and coated. For J_0 samples, symmetrical samples with PECVD on both wafer sides are fabricated. After diffusion, the samples are etched in HF to remove all dielectric layers. In this state, the R_{sheet} samples can be measured by means of four point probe (FPP) (see 3.1) and electrical capacitance-voltage (ECV) (see 3.2) measurements starting at the silicon surface. The J_0 samples are additionally RCA cleaned and double-sided passivated: On a boron diffusion (from PECVD BSG) a stack of 5 nm aluminium oxide (AlO_x) deposited by means of atomic layer deposition (ALD) in an InpassionLAB tool (SoLayTec) and 100 nm PECVD silicon nitride (SiN_y) deposited in a Roth & Rau (Meyer Burger) SiNA system are applied. Note that the $\text{AlO}_x/\text{SiN}_y$ stack is currently the best known passivation system of boron emitters with high stability during high-temperature firing [Sc09]. Alternatively, the PECVD BSG/ SiN_z stack that acts as diffusion source is not removed after co-diffusion but it is used as a passivation stack on the p^+ -diffusion instead of $\text{AlO}_x/\text{SiN}_y$. The J_0 samples are characterised by means of photoconductance lifetime measurements (see 3.5) before and after firing in a belt furnace at a peak temperature of about 850 °C.

In order to characterise the phosphorus diffusion resulting from POCl_3 co-diffusion, RCA cleaned planar $156 \times 156 \text{ mm}^2$ p -type Cz-Si wafers with a resistivity of about $5 \Omega \text{ cm}$ are introduced into the furnace tube for the fabrication of R_{sheet} test samples. As J_0 samples, textured n -type Cz-Si wafers are used. After diffusion, HF etching and RCA cleaning, both sample sides are passivated by 100 nm PECVD SiN_y and the J_0 samples are fired.

For ellipsometry measurements of oxide or PSG thicknesses, shiny-etched Fz p -type silicon wafers with 150 mm diameter are used. Alternatively, p -type Cz-Si $156 \times 156 \text{ mm}^2$ wafers can be polished single-sided so that ellipsometry measurements can be performed on the polished side and FPP measurements on the rough sample side.

Chapter 5

Optimization of PECVD diffusion sources

In this Chapter, the as-deposited and annealed PECVD layers and the boron diffusions from PECVD BSG are characterized in order to develop and optimize a PECVD boron diffusion source. We aim at depositing a PECVD BSG layer stack that is multifunctional: Boron diffusions with reasonable R_{sheet} and J_0 values for solar cell fabrication shall be achieved during $POCl_3$ co-diffusion processes. Thus, the PECVD layer stack needs to act both as B diffusion source and P diffusion barrier. In addition, it needs to function as an etching barrier during chemical cleaning and texturing steps as applied during solar cell processing. Furthermore, the PECVD stack might be applied as surface passivation and anti-reflective coating.

This multifunctional PECVD stack will be integrated in the n -type silicon solar cell fabrication and allow to significantly simplify the process flow, as will be shown in Chapter 6.

First, undoped PECVD layers and BSG layers are characterised by means of ellipsometry and their properties are discussed in dependence on the deposition parameters. Second, the PECVD BSG layers are exposed to different high-temperature treatments such as a separate boron drive-in or a co-diffusion process with furnace parameter settings. The sheet resistances R_{sheet} , saturation current densities J_0 and concentration profiles of the resulting boron diffusions are measured and the dependencies on

various PECVD and furnace parameters are evaluated. Third, the surface passivation quality of PECVD BSG with different capping layers is evaluated and compared to an $\text{AlO}_x/\text{SiN}_y$ passivation. By means of a Corona charge analysis, the BSG passivation mechanism is investigated.

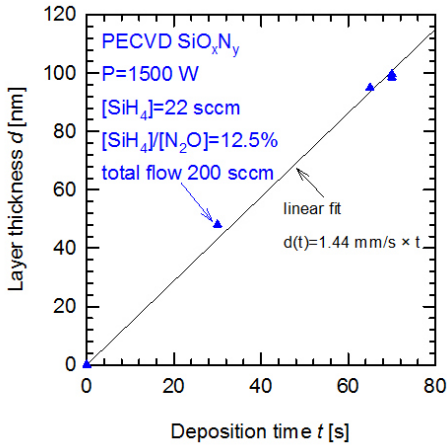
5.1 Properties of PECVD layers

5.1.1 Undoped PECVD oxynitride

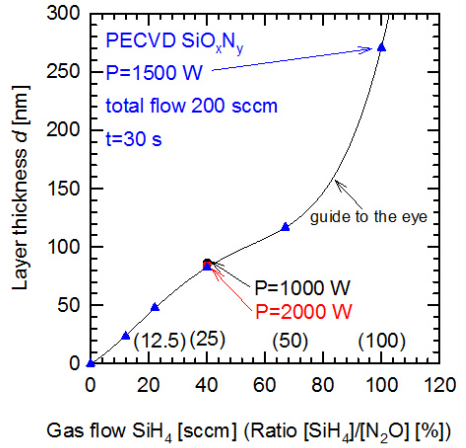
For the first deposited PECVD layers, the precursor gases silane SiH_4 and nitrous oxide N_2O are used so that the resulting dielectric layers are expected to be undoped oxynitride SiO_xN_y layers. The process chamber set temperature $\vartheta=400^\circ\text{C}$ and the total gas flow of 200 sccm are kept constant. This total gas flow defines the pressure p in the process chamber during gas inlet that is $(4.0 \pm 0.2) \times 10^{-3}$ mbar. The plasma power P , the gas flows of the precursors SiH_4 and N_2O and thus the ratio $[\text{SiH}_4]/[\text{N}_2\text{O}]$ and the deposition time are varied. The resulting layer thickness d is determined by spectral ellipsometry measurements.

Figure 5.1 (a) shows that for a fixed SiH_4 gas flow of 22 sccm and a ratio of $[\text{SiH}_4]/[\text{N}_2\text{O}]=12.5\%$, the PECVD layer thickness increases linearly with the deposition time. When the deposition time is kept constant, the layer thickness is increased with increasing $[\text{SiH}_4]$ and thus increasing $[\text{SiH}_4]/[\text{N}_2\text{O}]$, as shown in Fig. 5.1 (b). The PECVD thickness is not significantly influenced by varying the plasma power from 1000 W to 2000 W, as demonstrated for $[\text{SiH}_4]/[\text{N}_2\text{O}]=25\%$.

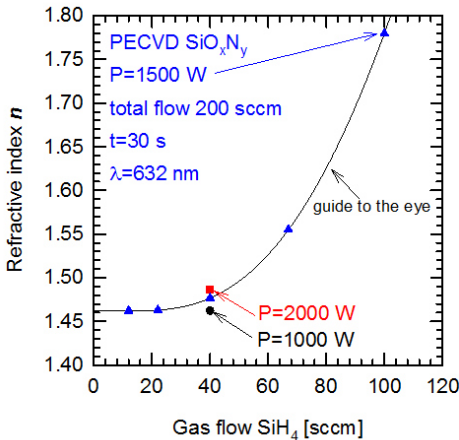
By spectral ellipsometry measurements the refractive index n of the PECVD layers is determined at a wavelength of $\lambda=632$ nm. Figure 5.1 (c) shows a measured refractive index $n=1.46$ for SiH_4 gas flows ≤ 22 sccm. This refractive index corresponds to silicon dioxide SiO_2 . For higher SiH_4 flows, n increases nonlinearly up to $n=1.78$ for a gas flow of 100 sccm. By increasing the plasma power from 1000 W to 2000 W, the measured n is slightly increased from 1.46 to 1.49.



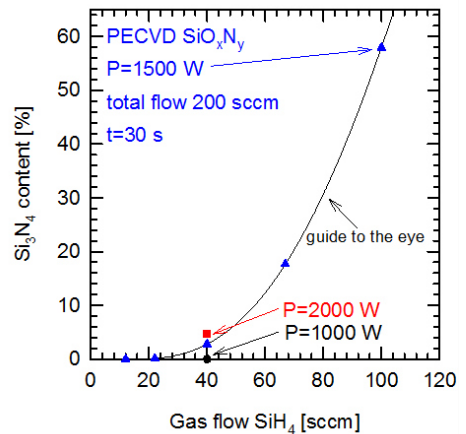
(a)



(b)



(c)



(d)

Figure 5.1: Thickness of undoped PECVD layers as a function of (a) deposition time and (b) SiH_4 gas flow for different plasma powers. (c) Refractive index and (d) Si_3N_4 content as a function of SiH_4 gas flow for different plasma powers.

The ellipsometry data is fitted by applying an effective medium approximation (EMA) using models for silicon dioxide SiO_2 and silicon nitride Si_3N_4 . The content of Si_3N_4 is increased with growing SiH_4 in a nonlinear way, as shown in Fig. 5.1 (d), similar to the increase in n . For low SiH_4 gas flows ≤ 22 sccm and a refractive index of 1.46, the Si_3N_4 content is 0%. For gas flows ≥ 40 sccm the Si_3N_4 content is growing steeply up to 58 % for 100 sccm which corresponds to the increasing values for n .

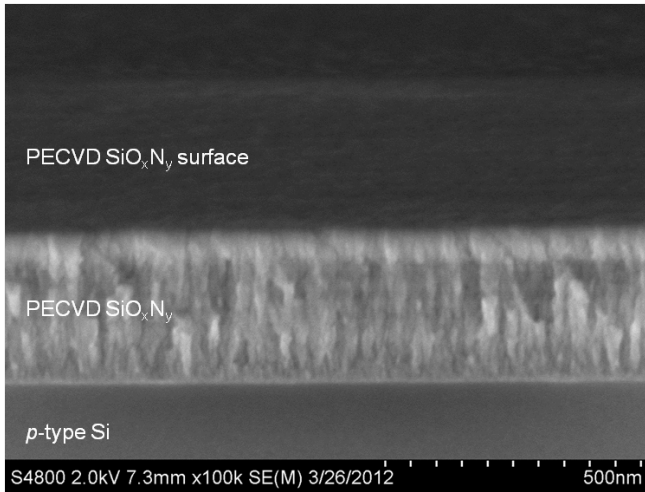


Figure 5.2: SEM image of a PECVD SiO_xN_y layer with a thickness of about 307 nm deposited on planar, polished p -type Si.

In addition, scanning electron microscopy (SEM) investigations together with energy-dispersive X-ray spectroscopy (EDS) measurements are performed in order to prove the ellipsometry-measured layer thicknesses and to investigate the structure and composition of the PECVD layers. Details of the working principles of SEM can be found in [Go03].

Figure 5.2 shows a cross fracture of a polished p -type FZ Si wafer with a thick PECVD layer that is deposited in 120 s with a SiH_4 gas flow of 40 sccm. By monochromatic ellipsometry measurements (at a wavelength of 632 nm) an average layer thickness of (323 ± 1) nm is measured that agrees with the average thickness of (307 ± 21) nm that is measured at different sample positions by SEM. Within the PECVD SiO_xN_y layer, a

columnar structure is observed and the surface of the PECVD layer that is visible in Fig. 5.2 shows a rough structure.

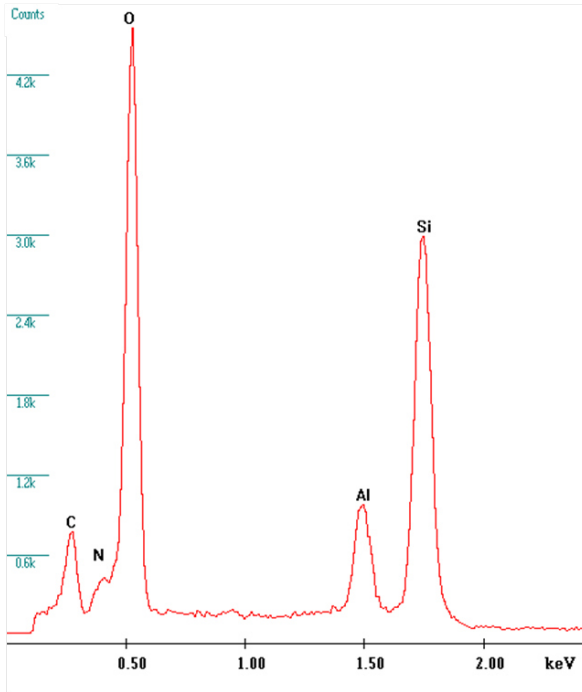


Figure 5.3: EDS spectrum of a PECVD layer.

By an EDS measurement using a spot mode, the spectrum shown in Fig. 5.3 is detected. The Al signal results from the specimen holder and is not included in the quantification. A composition of the PECVD layer of 62%_{wt.} Si, 34%_{wt.} O and 4%_{wt.} N corresponding to 47%_{at.} Si, 46%_{at.} O and 7%_{at.} N is calculated from the spectrum. Although a spot mode is used for signal detection from the PECVD layer, the detection area is larger than the layer thickness and there is a significant signal contribution from the Si substrate. Thus the amount of Si in the PECVD layer is assumed to be overestimated by 50%. With this assumption, a composition of 23%_{at.} Si and 46%_{at.} O is derived, indicating that the PECVD layer is resembling a silicon dioxide SiO₂. Due to the uncertainty of the EDS analysis, the composition of the PECVD layer can not be determined exactly. The small nitrogen content is difficult to quantify because of the low N signal.

But the amount of nitrogen in the PECVD layer can be estimated to be $\leq 7\%_{at.}$ which is in agreement with the ellipsometry results (see Fig. 5.1 (d)).

It is concluded that an undoped PECVD silicon dioxide SiO_2 is deposited for SiH_4 gas flows ≤ 22 sccm and a ratio of $[\text{SiH}_4]/[\text{N}_2\text{O}] \leq 12.5\%$ and silicon oxynitrides SiO_xN_y are grown when the SiH_4 gas flow is increased to > 40 sccm and the ratio of $[\text{SiH}_4]/[\text{N}_2\text{O}]$ is greater than 25%.

In the following, PECVD parameters for SiO_2 layers ($n=1.46$) with additional doping gases are used to deposit diffusion sources. SiO_xN_y layers with an increased refractive index resulting from the nitrogen content are evaluated as capping layers on top of the PECVD diffusion sources. These SiO_xN_y capping layers should act as diffusion and etching barriers, as SiN_z layers do. But for SiO_xN_y , a higher etching rate in HF is observed compared to SiN_z . Thus, if SiO_xN_y is applied instead of SiN_z , thicker capping layers are needed but they still allow for an easier removal of the dielectric layers during solar cell processing.

5.1.2 PECVD boron silicate glass

For the deposition of boron silicate glass (BSG) layers that act as solid, single-sided boron diffusion sources, the precursor gas diborane B_2H_6 that is diluted in 97% H_2 is added. The PECVD BSG layers are deposited with a gas flow ratio of either $[\text{SiH}_4]/[\text{N}_2\text{O}] = 6.25\%$ or 12.5% or 25%, increasing B_2H_6 gas flows and constant total gas flows of 200 sccm and a power of 1500 W. They are characterised by monochromatic and spectral ellipsometry measurements. The results are summarized in Table 5.1.

A refractive index n of 1.44 to 1.50 is measured that does not depend on the B_2H_6 gas flow and is similar to n of an undoped PECVD SiO_2 layer for $[\text{SiH}_4]/[\text{N}_2\text{O}] = 25\%$, 12.5% and 6.25% (compare Figs. 5.1 (c)). The layer thicknesses and growth rates of the BSG are similar to that of the undoped PECVD layers (compare Fig. 5.1 (a) and (b)).

We conclude that the addition of B_2H_6 does not significantly influence the deposition behaviour and the optical properties of the PECVD layers.

The spectral ellipsometry data is fitted with an EMA composed of SiO_2 and B to extract the content of B in the PECVD BSG. For a gas flow ratio

PECVD BSG									
deposition parameters					Monochromatic ellipsometry			Spectral ellipsometry	
[B ₂ H ₆] [sccm]	[SiH ₄] [sccm]	[N ₂ O] [sccm]	[SiH ₄]/[N ₂ O] [%]	t [s]	d [nm]	n	d [nm]	B [% _{out.}]	B [% _{out.}]
8	38	154	25	30	76.9	1.44			
16	37	147	25	30	77.4	1.48	77.0	4.5	
16	20	164	12.5	50	72.7	1.45	70.5	2.2	
32	19	149	12.5	50	71.7	1.45	70.4	1.8	
40	32	128	25	30	67.1	1.48	65.8	6.1	
50	30	120	25	60	128.3	1.50	128.2	7.2	
50	17	133	12.5	50	67.0	1.45	65.5	1.8	
50	9	141	6.25	100	78.6	1.46	78.5	1.9	

Table 5.1: Ellipsometry (monochromatic at $\lambda=632$ nm and spectral) measurement results for PECVD BSG layers that are deposited with increasing B₂H₆ gas flows.

of $[\text{SiH}_4]/[\text{N}_2\text{O}]=25\%$, boron contents of about $4.5\text{--}7\%_{at.}$ are observed that increase with increased B_2H_6 gas flow from 16 sccm to 50 sccm. In the case of $[\text{SiH}_4]/[\text{N}_2\text{O}]\leq 12.5\%$, lower boron contents of about $2\%_{at.}$ are measured independent of the B_2H_6 precursor gas flow. Due to the uncertainty of the fit of a layer with multiple components, the boron contents are considered to be a rough estimation and the composition of the PECVD BSG needs to be evaluated with an appropriate measurement technique. However, the extracted B contents are very small and in order to increase the B concentration in the PECVD BSG, in the following the maximum B_2H_6 gas flow of 50 sccm is applied and the SiH_4 gas flow is further reduced to values ≤ 5 sccm, so that low gas flow ratios of $[\text{SiH}_4]/[\text{B}_2\text{H}_6]\leq 10\%$ are reached.

Boron concentration profiles

Boron concentration profiles in the PECVD BSG after deposition are measured by PP-TOFMS (Horiba Scientific) as described in 3.4 on n -type Cz-Si samples deposited with either 40 nm or 80 nm PECVD BSG with varied gas flow ratios of $[\text{SiH}_4]/[\text{B}_2\text{H}_6]=4\%$ and 10% .

Figure 5.4 shows the B profiles in the as-deposited PECVD BSG. Depth $d=0$ corresponds to the surface of the as-deposited 80-nm-thick layers, while $d=40$ nm corresponds to the surface of the 40-nm-thick layer. PP-TOFMS allows determining the boron concentration quantitatively and shows that it generally increases with increasing B_2H_6 flow during PECVD. The profiles show a higher B concentration at the BSG-Si interface. This might be explained by the hypothesis of a higher availability of boron at the beginning of the PECVD process when the plasma ignites. For the $[\text{SiH}_4]/[\text{B}_2\text{H}_6]$ ratio of 4% and 80-nm layer thickness, a maximum B concentration of $6.4 \times 10^{21} \text{ cm}^{-3}$ is measured, corresponding to $13\%_{at.}$ B. The B concentrations for the 40-nm-thick and the 80-nm-thick PECVD BSG layer (red and green line) are comparable; thus, the dopant concentration in the diffusion source is unaffected by the PECVD layer thickness. In the case of $[\text{SiH}_4]/[\text{B}_2\text{H}_6]=10\%$ (blue line) and an additionally reduced total gas flow (resulting in a reduced pressure in the process chamber), smaller B concentrations and a different concentration profile shape with a less pronounced peak are observed.

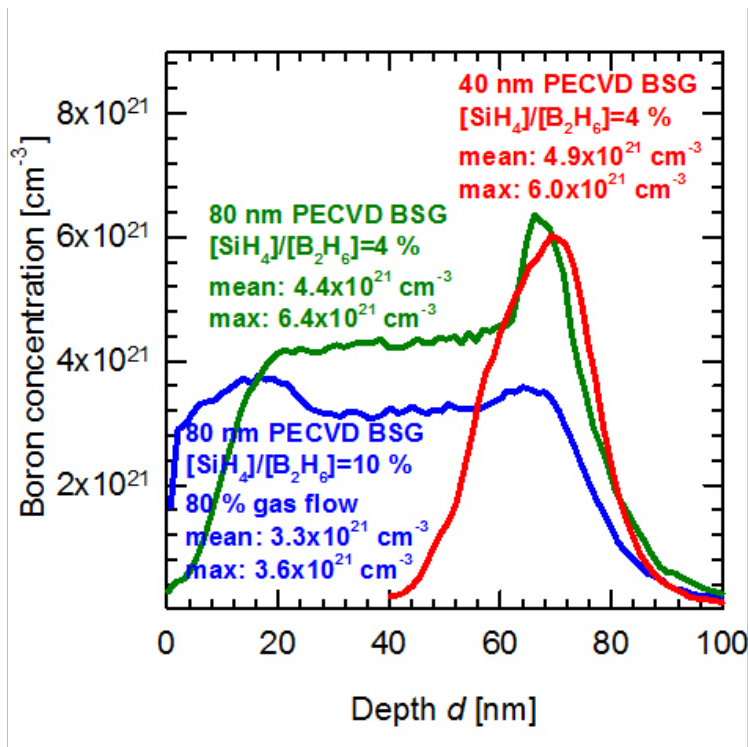


Figure 5.4: Depth-dependent boron concentration in PECVD BSG layers fabricated with $\text{SiH}_4/\text{B}_2\text{H}_6$ ratios of 10% or 4% and thicknesses of 40 or 80 nm, measured by PP-TOFMS (Horiba Scientific).

We conclude that by decreasing the $[\text{SiH}_4]/[\text{B}_2\text{H}_6]$ ratio and increasing the pressure during PECVD, the availability of B and thus the B concentration in the diffusion source is increased.

5.2 Boron diffusion from PECVD BSG and co-diffusion

The boron diffusion obtained from PECVD BSG layers as diffusion sources are characterised by R_{sheet} and J_0 measurements as well as doping profile measurements as described in Chapter 3. The PECVD parameters such as precursor gas flow ratios and layer thicknesses are varied and the in-

fluence on the resulting boron diffusion is discussed. Also, the impacts of different parameters of the co-diffusion process and of different capping layers on top of the BSG layer are investigated. We mostly use planar Cz silicon substrate wafers, but we also investigate the influence of the silicon surface and characterise PECVD deposition and boron diffusion on textured Si. For high boron concentrations in the PECVD diffusion source, the formation of a boron rich layer can be observed.

5.2.1 Impact of the PECVD gas flow ratios

From the first deposited PECVD BSG layers with thicknesses of about 60-130 nm and varied B_2H_6 precursor gas flows, the boron drive-in is performed in N_2 ambient at a high temperature of 1050 °C and for a long duration of 5 h in order to reach a measurable boron diffusion. No capping layer is applied on top of the PECVD BSG. Figure 5.5 shows the inductively measured boron sheet resistances $R_{sheet,B}$ in dependence of $[B_2H_6]$ for different $[SiH_4]/[N_2O]$ ratios. The B_2H_6 gas flow is increased until the maximum flow of 50 sccm, limited by the mass flow controller of our deposition tool, is reached. $R_{sheet,B}$ decreases with increasing B_2H_6 flows, but high sheet resistances $> 500 \Omega/\square$ are measured for $[SiH_4]/[N_2O]=25\%$. In order to further increase the amount of boron introduced in the PECVD BSG layer and to lower $R_{sheet,B}$, the SiH_4 gas flow and thus the $[SiH_4]/[N_2O]$ ratio is decreased. For the lowest $[SiH_4]/[N_2O]$ ratio of 6.25% and a maximum B_2H_6 gas flow of 50 sccm, a boron sheet resistance of $35 \Omega/\square$ is measured.

In order to form a boron emitter or back surface field from a PECVD BSG diffusion source during solar cell fabrication, sheet resistances of $R_{sheet,B} \leq 100 \Omega/\square$ should be achieved. Thus, in the following we apply the maximum diborane gas flow of 50 sccm and low silane gas flows and $[SiH_4]/[N_2O]$ ratios. In addition, the diffusion time and temperature for the boron drive-in step are reduced aiming at diffusion processes that are relevant for industrial solar cell fabrication. For a process simplification, the B drive-in shall not be performed in a separate diffusion but during a $POCl_3$ co-diffusion, as described in 4.3. Therefore, a capping layer needs to be deposited on the BSG to prevent a P indiffusion from the $POCl_3$ ambient. PECVD BSG layers with a thickness of either 40 nm

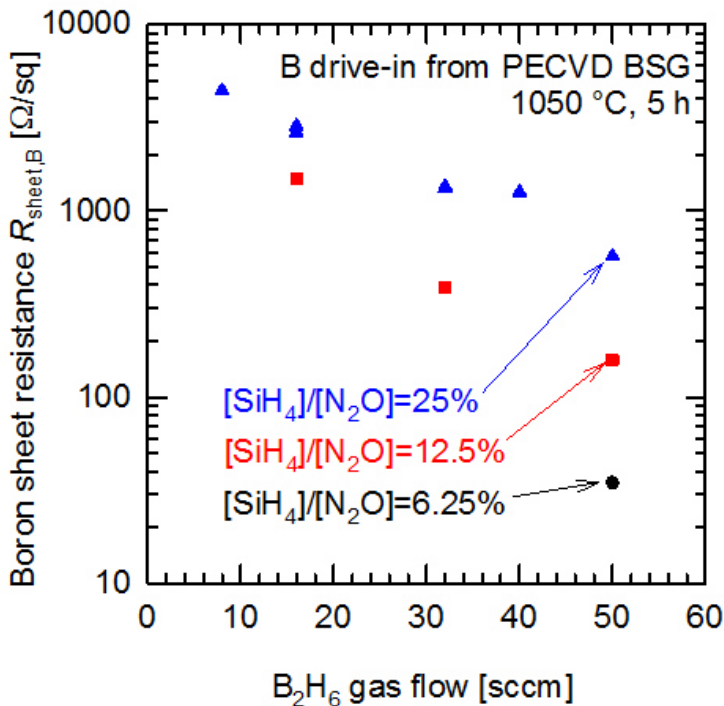


Figure 5.5: Boron sheet resistance $R_{sheet,B}$ in dependence on the B_2H_6 gas flow after a drive-in at $1050^\circ C$ for 5 h.

or 80 nm are deposited on planar n -type Cz-Si wafers. The B_2H_6 gas flow of 50 sccm and the total gas flow of 200 sccm are kept constant while the SiH_4 gas flow is increased from 1 sccm to 5 sccm thus the gas flow ratios $[SiH_4]/[B_2H_6]$ is varied from 2% to 10%. A 170 nm-thick SiN_x capping layer is deposited on top of the BSG. The boron drive-in from the PECVD BSG/ SiN_x stack is performed at $950^\circ C$ for 60 min during a $POCl_3$ co-diffusion.

Figure 5.6 shows R_{sheet} of the boron diffusions obtained from PECVD BSG for varying gas flow ratios $[SiH_4]/[B_2H_6]$ and two different thickness values. Each errorbar corresponds to the standard deviation of the FPP-measured R_{sheet} values on one $15.6 \times 15.6 \text{ cm}^2$ wafer. We find that R_{sheet} is strongly influenced by the SiH_4 and B_2H_6 gas flow and the $[SiH_4]/[B_2H_6]$ ratio during PECVD while the applied N_2O gas flow changes are very

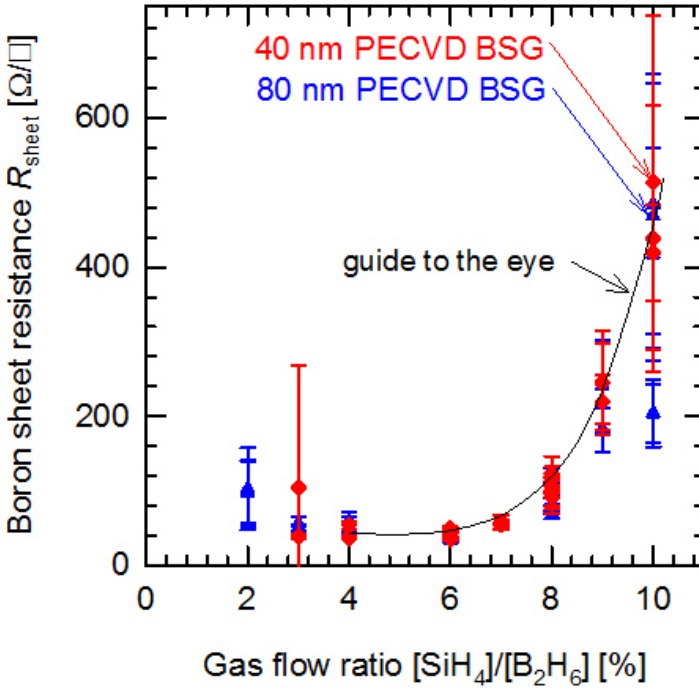


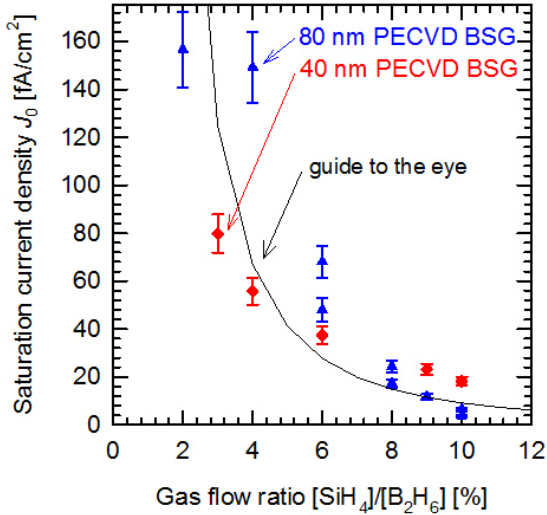
Figure 5.6: The sheet resistance R_{sheet} of boron diffusions in dependence on gas flow ratios of the precursor gases during PECVD, measured with a four-point probe (FPP). Two different PECVD BSG thicknesses are shown.

small ($\leq 3\%$) and do not affect the sheet resistance results. The sheet resistance decreases with decreasing $[SiH_4]/[B_2H_6]$ ratio. A minimum R_{sheet} of about $30 \Omega/\square$ with a minimum standard deviation of 4% is reached for a gas flow ratio of 6%. (Note that the B_2H_6 gas flow in the $[SiH_4]/[B_2H_6]$ ratio refers to the flow of 3% B_2H_6 in H_2 so that the absolute amount of diborane is quite small.) For the lowest gas flow ratios of 2% and 3% we observe an increase of the R_{sheet} values and stronger scattering of the data. These experimental results might be explained as follows: The B concentration in the PECVD BSG increases with decreasing gas flow ratios and for $[SiH_4]/[B_2H_6] \leq 6\%$ the dopant concentration is so high that the layer acts as an infinite diffusion source, comparable to BSG layers fabricated from BBr_3 in a furnace. For the lowest ratios $< 4\%$ the boron

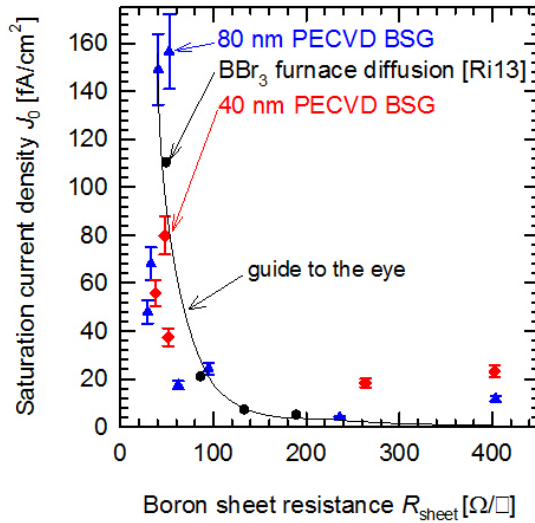
concentration might be that high that a boron rich layer (BRL) formation takes place so that the depths of the boron diffusion is lowered and R_{sheet} is increased, as also observed in [Ku12]. For gas flow ratios $\geq 8\%$, with a growing $[\text{SiH}_4]/[\text{B}_2\text{H}_6]$ ratio the sheet resistance and also the standard deviation are strongly increased. For the highest gas flow ratio of 10% we suspect a low boron content in the BSG layer that is nonhomogeneously distributed, resulting in a weak and inhomogeneous boron diffusion. Note that the sheet resistance is not evidently influenced by the thickness of the diffusion source, as will be discussed in more detail in 5.2.2.

As boron J_0 samples, planar n -type Cz silicon wafers are symmetrically deposited with PECVD BSG/ SiN_z and boron diffused during the co-diffusion. The samples are passivated by a stack of $\text{AlO}_x/\text{SiN}_y$ and fired. By using PECVD BSG layers as diffusion sources, low saturation current densities J_0 can be reached on the $\text{AlO}_x/\text{SiN}_y$ passivated p^+ -emitters, as shown in Fig. 5.7. J_0 depends on the gas flow ratio of the precursor gases and decreases for increasing $[\text{SiH}_4]/[\text{B}_2\text{H}_6]$, both for a 80 nm and a 40 nm-thin PECVD BSG diffusion source, as shown in Fig. 5.7 (a). In Fig. 5.7 (b), the J_0 results are plotted as a function of the boron sheet resistance R_{sheet} . The saturation current density decreases with increasing R_{sheet} values. We measure J_0 values as low as 4 fA/cm² at a sheet resistance of 236 Ω/\square and a layer thickness of 80 nm. For a reasonable boron emitter sheet resistance for solar cell fabrication of 62 Ω/\square we achieve $J_0=17$ fA/cm² after diffusion from an 80 nm PECVD BSG layer. Within the measurement uncertainty of 10% for J_0 measurements with the photoconductance lifetime tester we observe similar J_0 values for 80 nm and 40 nm-thin PECVD BSG diffusion sources. The measured J_0 values are similar to literature best values for standard BBr_3 furnace diffusions [Ri13] over a wide range of emitter sheet resistances.

To sum up, the gas flow ratio of the precursor gases silane and diborane applied during PECVD of BSG diffusion sources strongly influences the sheet resistance of the resulting boron p^+ -emitter. For increasing $[\text{SiH}_4]/[\text{B}_2\text{H}_6]$, R_{sheet} increases. Thus, the saturation current density J_0 on the $\text{AlO}_x/\text{SiN}_y$ -passivated emitters decreases as a function of R_{sheet} . Low J_0 results < 20 fA/cm² at $R_{sheet} \geq 60 \Omega/\square$ are achieved for $[\text{SiH}_4]/[\text{B}_2\text{H}_6] \leq 8\%$.



(a)



(b)

Figure 5.7: Saturation current densities J_0 plotted as a function of (a) the gas flow ratios $[SiH_4]/[B_2H_6]$ and (b) the boron sheet resistance R_{sheet} . The obtained J_0 values are comparable to literature best values resulting from BBr_3 furnace diffusions [Ri13].

J_0 is not evidently influenced by the thickness of the BSG layer, as will be discussed in more detail in 5.2.2.

Dopant concentration profiles

Boron doping profiles in the Si after co-diffusion from different PECVD BSG/SiN_z stacks are measured by ECV and shown in Fig. 5.8. The ECV measurements are performed after removal of all dielectric layers by HF and start at the silicon surface. The profile depth d is evaluated at a dopant concentration of $1.0 \times 10^{16} \text{ cm}^{-3}$.

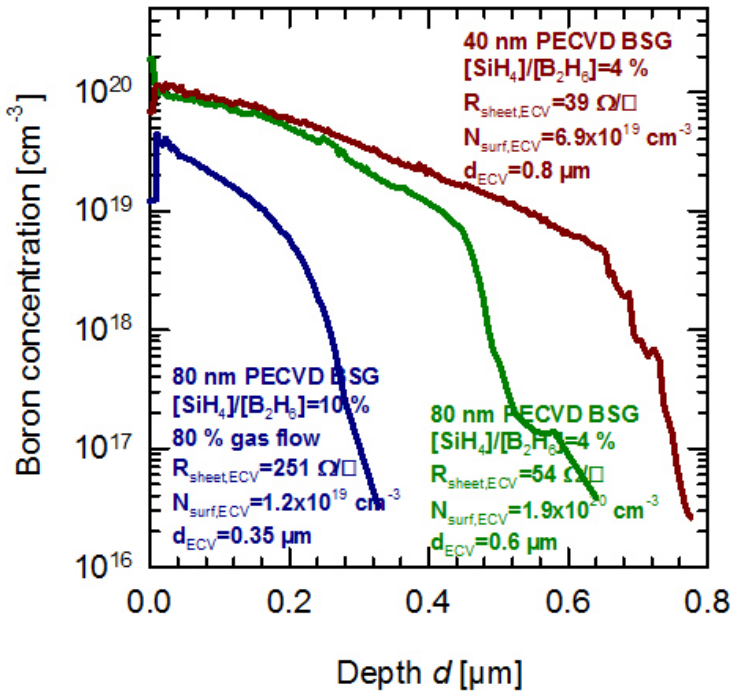


Figure 5.8: Boron concentration profiles after diffusion from different PECVD BSG layers measured by ECV.

For a boron diffusion from a 40-nm-thin PECVD BSG layer with a [SiH₄]/[B₂H₆] ratio of 4%, a surface concentration N_{surf} of $6.9 \times 10^{19} \text{ cm}^{-3}$ and a profile

depth d of about $0.8 \mu\text{m}$ measured, resulting in an R_{sheet} of $39 \Omega/\square$ (dark red line), as measured by an FPP (see Fig. 5.6). For the thicker diffusion source with a PECVD BSG layer thickness of 80 nm (dark green line), a pile-up of the B concentration at the surface is visible. The measured depth is lower resulting in a higher R_{sheet} of $54 \Omega/\square$, which is in agreement with the FPP measurements. For the higher $[\text{SiH}_4]/[\text{B}_2\text{H}_6]$ gas flow ratio of 10% (dark blue line), a shallow diffusion profile with a lower N_{surf} and a high boron sheet resistance of $251 \Omega/\square$ is derived from the ECV and FPP measurements.

We conclude that the $[\text{SiH}_4]/[\text{B}_2\text{H}_6]$ ratio and thus the B concentration in the PECVD diffusion source strongly influence the surface concentration, while the PECVD layer thickness affects the diffusion profile shape and depth.

The concentrations of the dopant atoms in a 80 nm -thick PECVD BSG layer with a $[\text{SiH}_4]/[\text{B}_2\text{H}_6]$ ratio of 4% capped with SiN_z on a Si substrate after co-diffusion can be measured by PP-TOFMS, as described in 3.4.

Fig. 5.9 shows the quantitative PP-TOFMS profiles of B and P in atoms $\times \text{cm}^{-3}$, as well as the relative ratios of Si, O, and N. The PP-TOFMS samples were not etched after co-diffusion and the measurement starts in the dielectric layers, revealing an about 300-nm -thick layer stack of PECVD BSG ($\approx 140 \text{ nm}$), SiN_z capping layer ($\approx 100 \text{ nm}$), and a PSG ($\approx 60 \text{ nm}$) grown during the POCl_3 codiffusion. The boron concentration in the PECVD BSG after diffusion shows a broader profile without the B concentration peak at the Si surface visible after deposition before annealing, as shown in Fig. 5.4. The PP-TOFMS measurements indicate a B diffusion not only into the Si wafer but into the SiN_z capping layer as well.

The PP-TOFMS-measured B concentration in the PECVD BSG diffusion source $c_{B,BSG}$ is used as an input parameter for our process simulations to reproduce the diffusion profiles, as will be presented in 7.1.

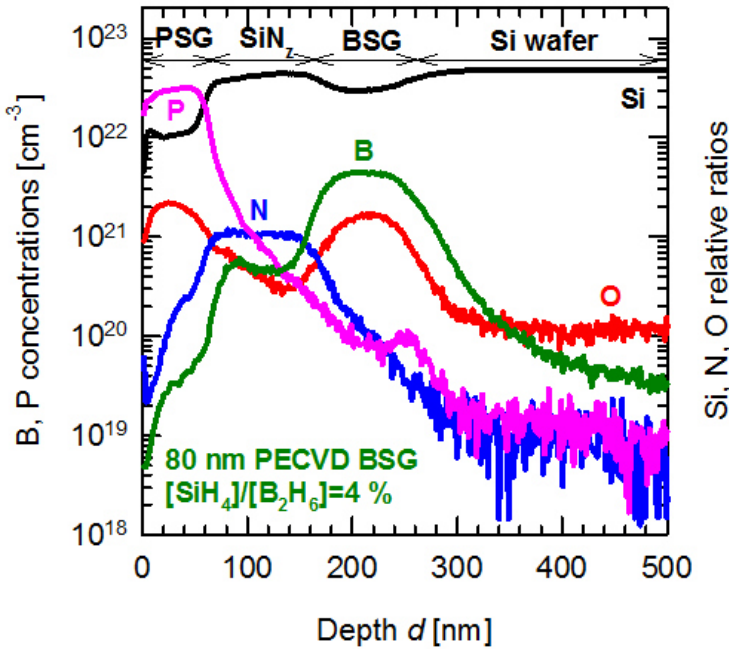


Figure 5.9: Concentration profiles of the elements B and P and relative ratios of Si, N, O measured by PP-TOFMS (Horiba Scientific). An about 300-nm-thick layer system of PSG, SiN_x and BSG is visible on top of the Si wafer after co-diffusion without etching.

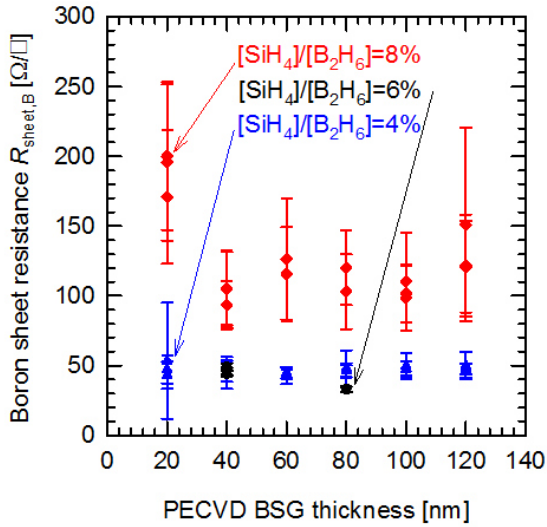
5.2.2 Impact of the PECVD BSG layer thickness

We investigate the influence of the PECVD BSG layer thickness on the resulting boron diffusion in more detail for three different gas flow ratios. Figure 5.10 (a) shows that $R_{sheet,B}$ is independent on the PECVD BSG layer thickness over a wide thickness range. The error bars are the standard deviations of 121 FPP measurements on the entire area of a $156 \times 156 \text{ mm}^2$ *n*-type Cz-Si wafer. For 20 nm-thin PECVD BSG layers we observe an increase of $R_{sheet,B}$ and its standard deviation compared to thicker BSG layers. We attribute this increase to an inhomogeneity of the PECVD BSG thickness: On a $156 \times 156 \text{ mm}^2$ wafer the layer thickness at the edge is about 10% to 30% smaller than in the center. Thus, when aiming at a 20 nm thick PECVD BSG layer in the wafer center, the

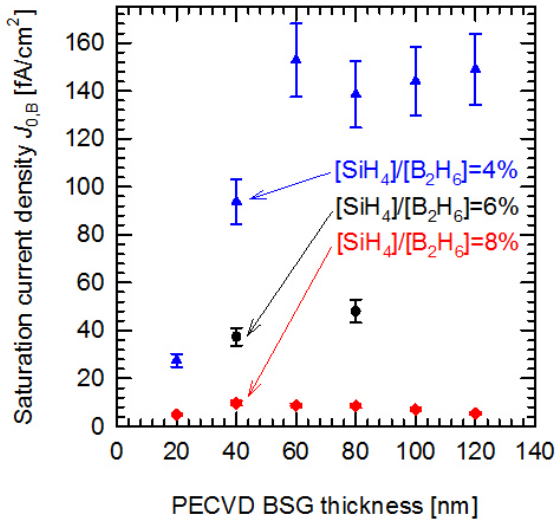
boron diffusion source is only about 14 nm at the edge. This results in an increase of the average $R_{sheet,B}$. For higher layer thickness values of 40 nm to 120 nm the measured $R_{sheet,B}$ is constant within the measurement uncertainty for all considered gas flow ratios. Assuming that the boron diffusion from PECVD BSG into Si is mainly influenced by the boron content present at the BSG-Si interface explains these findings including the independence of the sheet resistance on the layer thickness for layers that are thicker than 40 nm. Note that the higher $[SiH_4]/[B_2H_6]$ ratio of 8% results in higher sheet resistances and standard deviations because the PECVD BSG diffusion source has a lower boron content compared to a PECVD layer with $[SiH_4]/[B_2H_6]=4\%$ and 6%. $R_{sheet,B}$ is similar for the two lower gas flow ratios. The hypothesis of an infinite diffusion source for both PECVD BSG layers with $[SiH_4]/[B_2H_6]=4\%$ and 6% explains this behavior.

In Fig. 5.10 (b), the saturation current density values are shown for different PECVD BSG thickness values. The estimated measurement uncertainty is 10%. For the gas flow ratio $[SiH_4]/[B_2H_6]=8\%$ low $J_{0,B}$ values of 5 to 10 fA/cm² are reached (corresponding to an average sheet resistance of 127 Ω/\square). The PECVD BSG layer thickness has no discernible impact. For the lowest ratio of the precursor gases $[SiH_4]/[B_2H_6]=4\%$ we observe, however, a reduction of $J_{0,B}$ from 153 fA/cm² to 28 fA/cm² for thickness values decreasing from 60 nm to 20 nm, although $R_{sheet,B}=43 \Omega/\square$ to 53 Ω/\square is approximately constant.

We conclude that low $J_{0,B}$ can be obtained at low boron concentrations with BSG layers that have a thicknesses ranging from 20 nm to 120 nm. However, due to the observed inhomogeneity in BSG thickness at least 40 nm of BSG should be used. For higher boron concentrations and larger thickness values the saturation current density increases. We speculate that this is due to an increased concentration of supersaturated boron at the surface or even due to the formation of a boron rich layer (BRL) [Ke10]. We consider a layer thickness of 40 nm and a gas flow ratio of $[SiH_4]/[B_2H_6]=8\%$ as optimized PECVD parameters for the BSG diffusion source so that boron emitters with low $J_{0,B}$ values can be achieved without the formation of BRL as it is present in standard BBr₃ furnace diffusions.



(a)



(b)

Figure 5.10: (a) Measured sheet resistance $R_{sheet,B}$ and (b) saturation current density $J_{0,B}$ as a function of the PECVD BSG layer thickness for different $[SiH_4]/[B_2H_6]$ gas flow ratios. $J_{0,B}$ was measured on about $150 \mu m$ thick $5-6 \Omega cm$ n -type Cz-Si samples after two-sided PECVD, boron drive-in, AlO_x/SiN_y passivation and firing.

5.2.3 Impact of co-diffusion parameters and capping layers

We measure diffusion profiles for the B diffusion from PECVD BSG and for the P diffusion from POCl_3 gas that are formed during co-diffusions with different parameter settings. The diffusion profiles are known to be strongly affected by temperature and time. Thus, we vary the temperature of the B drive-in step of the co-diffusion from 950 °C to 1000 °C and the time from 30 min to 60 min. We also investigate the influence of the applied nitrogen flow during the B drive-in step by varying the flow from 1 standard liter per minute (slm) to 12 slm. The impact of different capping layers on top of the PECVD BSG is evaluated as well. PECVD silicon nitride (SiN_z) and silicon oxynitride (SiO_xN_y) layers with different thicknesses are used and the resulting diffusion profiles are compared with the diffusion from uncapped PECVD BSG layers. For a co-diffusion with a B drive-in step at 1000 °C for 60 min, we observe that the applied nitrogen flow during the B drive-in step affects the resulting P sheet resistances: an increasing N_2 flow leads to decreasing sheet resistance of the P diffusions as shown in Fig. 5.11. The ECV measurements indicate that *n*-type doped regions with low sheet resistances $R_{sheet,P}$ of about 15 Ω/\square and a profile depth of about 1.3 μm are reached for 12 slm N_2 . For the lower gas flow of 8 slm N_2 , the depth is lowered and therefore $R_{sheet,P}$ is increased to about 28 Ω/\square .

We attribute the impact of different N_2 flows on $R_{sheet,P}$ to the following effect: Nitrogen displaces oxygen from the air that flows in the furnace while loading the quartz boat containing the samples. For low N_2 flows during the 1000 °C step, a high concentration of unwanted oxygen reacts with silicon on the uncoated substrate surface leading to a thick thermal oxide layer. However, for high N_2 flows and resulting thin thermal oxide layers, the amount of P_2O_5 from the furnace walls dissolved in the oxide is sufficient to decrease the melting temperature of the SiO_2 - P_2O_5 -phase such that this mixed phase becomes liquid at diffusion temperatures ≥ 850 °C [Ba69]. Thus, P-diffused regions with very low sheet resistances of about 15 Ω/\square are formed during the 1000 °C step and the subsequent POCl_3 diffusion.

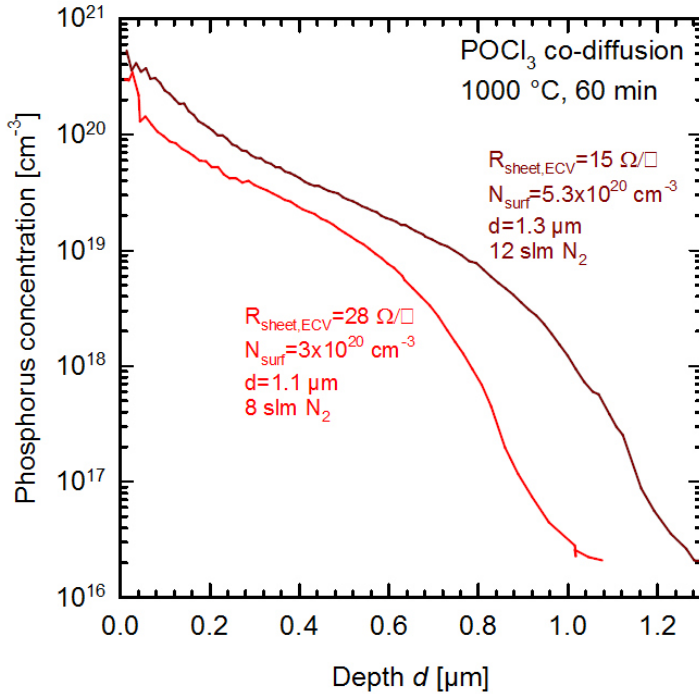
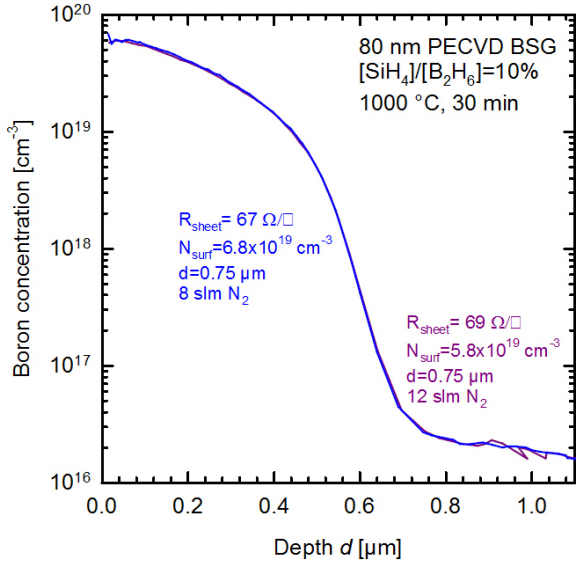
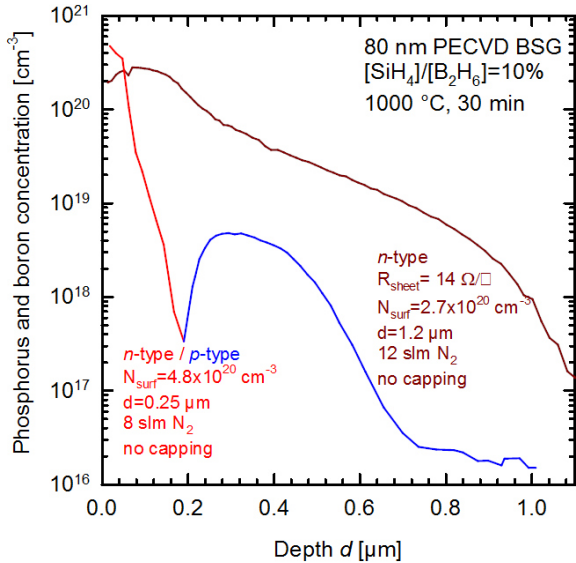


Figure 5.11: Doping profiles measured by ECV on the planar sample side that was uncovered and therefore was P-diffused during the co-diffusion process with N₂ gas flows of either 8 slm or 12 slm during the 1000 °C step.

Figure 5.12 (a) demonstrates that by the co-diffusion process, B-diffused *p*-type regions with sheet resistances of about 67-69 Ω/□ are successfully produced. Note the strong influence of the SiN_z capping layer: only PECVD BSG/SiN_z stacks result in *p*-type doped regions that are unaffected by the N₂ flow. The 80 nm-thick PECVD BSG with [SiH₄]/[B₂H₆] = 10% was capped with an about 50 nm-thick SiN_z. In the case of the uncapped BSG layers shown in Fig. 5.12 (b), *n*-type doping is measured at the sample surface indicating that phosphorus was diffused through the PECVD BSG. At a gas flow of 8 slm, the measured doping type changes to *p*-type due to boron diffusion, while at 12 slm of N₂ no *p*-type doping is observed at all.



(a)



(b)

Figure 5.12: Doping profiles measured by ECV on the planar sample sides that were covered with PECVD BSG, (a) with and (b) without a SiN_z capping layer. A co-diffusion process with N₂ gas flows of either 8 slm or 12 slm during the 1000 °C step was performed.

5.2.4 Impact of the silicon surface morphology

Until now, the boron diffusion from PECVD BSG was performed on planar (100)-oriented silicon surfaces. When an alkaline texture is applied, it is more challenging to deposit a closed PECVD BSG layer and a capping layer with a homogeneous layer thickness and to reach a continuous boron diffusion during co-diffusion.

Compared to a planar Si surface, a textured Si surface has an about 1.7 times larger surface area. Thus, the PECVD deposition time needs to be increased by this factor in order to reach approximately the same layer thickness on a textured surface as the target thickness on planar Si. When a random pyramid structure is present during PECVD, the layer thickness at the bottom of the pyramids is expected to be lower than at the tops due to shadowing effects.

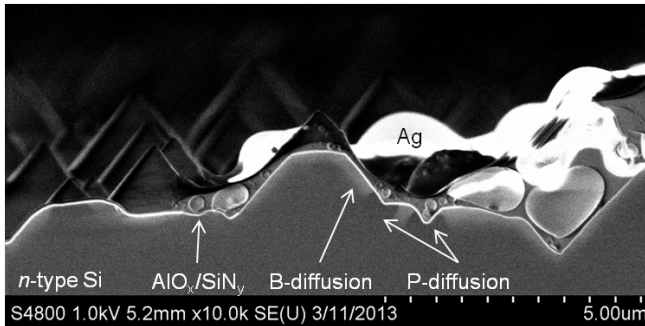


Figure 5.13: SEM image of a boron diffusion from a 80 nm-thick PECVD BSG with $[\text{SiH}_4]/[\text{B}_2\text{H}_6]=10\%$ capped with a 50 nm-thick SiN_z layer on alkaline textured *n*-type silicon. After co-diffusion (1000°C for 30 min), the BSG/ SiN_z stack is removed and an $\text{AlO}_x/\text{SiN}_y$ passivation and Ag screen-print metallization are applied. A P-indiffusion is visible that results in shunted solar cells.

Figure 5.13 shows an SEM image of a textured silicon sample with a boron diffusion from a PECVD BSG layer with a thickness of 80 nm, a gas flow ratio of $[\text{SiH}_4]/[\text{B}_2\text{H}_6]=10\%$ and a 50 nm-thick SiN_z capping layer (already removed on the sample shown in Fig. 5.13). After POCl_3 co-diffusion with a boron drive-in step at 1000°C for 30 min, a shallow boron diffusion with a depth of about 110 nm is measured by SEM that is apparent as a bright area. The boron diffusion is not continuous but espe-

cially at the bottom of the pyramids interruptions are visible. The darker color in the SEM image of these interruptions compared to the n -type silicon substrate and the round shape indicate a phosphorus indiffusion. We assume that the capping layer at the bottom of the pyramids was too thin - especially after cleaning steps - to act as a diffusion barrier against phosphorus. For the fabrication of solar cells, all dielectric layers are removed, an $\text{AlO}_x/\text{SiN}_y$ passivation stack and a Ag screen-printing metallization are applied. The P-diffused interruptions lead to shunted solar cells because the Ag contacts the Si substrate, as visible in Fig. 5.13.

Thus, the PECVD BSG/ SiN_z stack needs to be further improved by increasing the boron concentration and the capping layer thickness to be used as a diffusion source on textured substrates.

We apply a nominal 80 nm-thick PECVD BSG with a lower gas flow ratio of $[\text{SiH}_4]/[\text{B}_2\text{H}_6]=6\%$ to increase the boron concentration in the BSG layer. The total gas flow of typically 200 sccm is reduced to 160 sccm while a fixed B_2H_6 gas flow of 50 sccm is used. Thus, the share of B_2H_6 in the total gas flow is increased from 25% to 31% resulting in a further increased boron concentration in the PECVD BSG layer.

SEM images are taken directly after PECVD and after drive-in, in order to investigate the homogeneity of the PECVD BSG and the resulting boron diffusion on an alkaline textured surface. Fig. 5.14 (a) shows that the deposition of a BSG with a thickness target of 80 nm (on a planar silicon surface) leads to a closed BSG layer with a thickness of about 40-65 nm that is greatest at the pyramid tops. This about 1.7 times lower BSG layer thickness is to be expected due to the pyramid structure of textured silicon. After the deposition of a nominal 127 nm-thick SiN_z capping layer, co-diffusion at 1000 °C for 30 min and BSG removal, a continuous p -type boron diffusion is formed, that is clearly visible in Fig. 5.14 (b) due to the doping contrast. When the drive-in time is increased to 60 min, the resulting boron diffusion reaches a higher depth of about 1000 nm and a better homogeneity. The 80 nm-thick PECVD BSG and the 100 nm-thick SiN_z capping layer are not removed before SEM. We observe dark areas at the PECVD BSG/ SiN_z at the pyramid valleys. We speculate that the PECVD stack may have been lifted from the Si substrate in the pyramid valleys due to different mechanical properties and especially coefficients of extension of the BSG and the SiN_z .

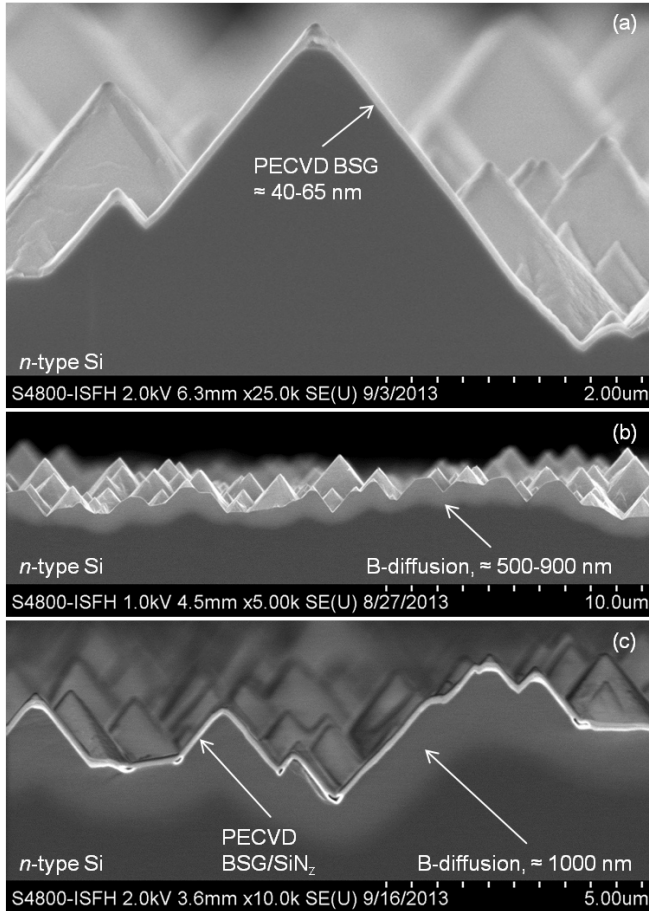


Figure 5.14: SEM images of a PECVD BSG on textured *n*-type silicon and the resulting boron diffusion. (a) A closed BSG layer is deposited, its thickness varies between about 65 nm at the top and 40 nm at the bottom of a pyramid. (b) After boron drive-in at 1000 °C for 30 min and BSG removal, a continuous *p*-type diffusion with a depth of 500-900 nm is observed. (c) For an increased drive-in time of 60 min, an about 1000 nm deep, homogeneous boron diffusion is obtained from a PECVD BSG with $[\text{SiH}_4]/[\text{B}_2\text{H}_6]=6\%$ and a 100 nm-thick SiN_z capping layer.

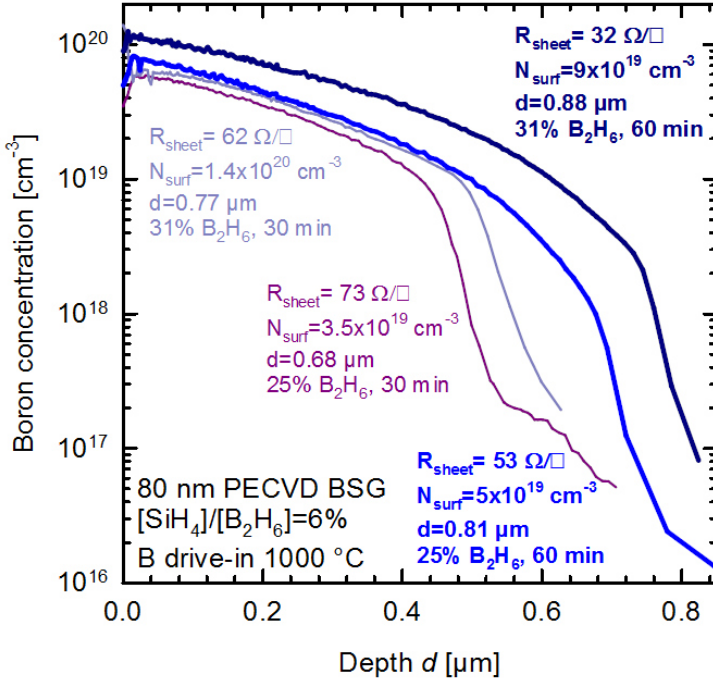


Figure 5.15: Boron doping profiles measured by ECV on textured silicon substrates. Higher diffusion depths and lower boron sheet resistances are reached by increasing the B₂H₆ gas flow share from 25% to 31% and the boron drive-in time from 30 min to 60 min.

Figure 5.15 shows boron doping profiles measured by ECV on textured samples for different PECVD gas flows and drive-in times of 30 min and 60 min. The 80 nm-thick PECVD BSG with [SiH₄]/[B₂H₆]=6% is capped with 127 nm SiN₂. Total gas flows of 200 sccm and 160 sccm and a fixed B₂H₆ gas flow are applied. The share of B₂H₆ in the total gas flow is 25% and 31%, respectively. After 30 min of boron drive-in, the doping profile for 25% B₂H₆ reveals a surface concentration of N_{surf}=3.5 × 10¹⁹ cm⁻³ resulting in a boron sheet resistance of R_{sheet}=73 Ω/□. For 31% B₂H₆, a pile-up of boron at the surface and a higher profile depth of 0.77 μm lead to a lower R_{sheet} of 62 Ω/□. Increasing the drive-in time to 60 min results in deeper doping profiles and also in higher surface concentrations of up to N_{surf}=9 × 10¹⁹ cm⁻³ for 31% B₂H₆ and thus a low sheet resistance of 32 Ω/□.

5.2.5 Boron-rich layer formation

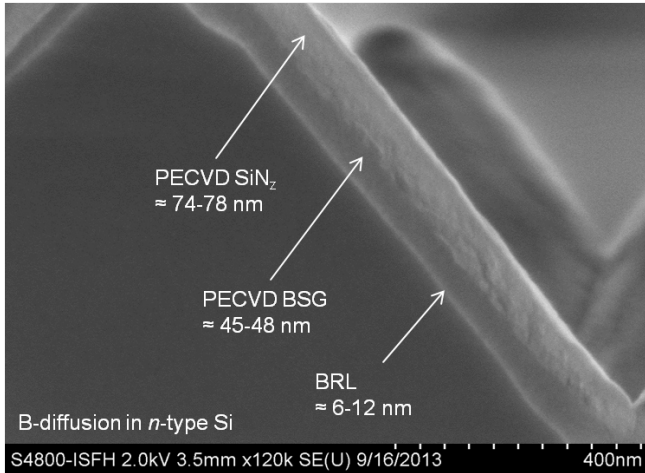


Figure 5.16: SEM image of a boron diffused textured Si sample. After 60 min B drive-in at 1000 °C from a PECVD BSG/SiN_z stack with [SiH₄]/[B₂H₆]=6%, a thin boron-rich layer (BRL) at the Si/BSG interface is present.

If the boron concentration in the PECVD BSG is high enough to exceed the solubility limit of boron in silicon of about $1.0 \times 10^{20} \text{ cm}^{-3}$ at the drive-in temperature of 1000 °C [Hu99, 10.4], a boron-rich layer (BRL) formation at the silicon/BSG interface occurs during the high-temperature step. The presence of a BRL is indicated by the observed hydrophilic behaviour of the sample surface after HF etch. In the SEM image shown in Fig. 5.16, a BRL with a thickness of 6-12 nm is visible as a bright line at the Si/BSG interface on a textured *n*-type silicon surface. For the PECVD BSG with a thickness target on a planar surface of 80 nm and the SiN_z capping layer with a thickness target of 100 nm, about 1.3-1.7 times lower thicknesses are determined due to the angles of the random pyramids.

The formation of a BRL makes a low temperature oxidation (LTO) necessary to remove the BRL in order to prevent bulk carrier lifetime degradation as observed in [Ke10]. The oxidation is an additional high-temperature step that we want to avoid during simplified solar cell processing. Thus, the boron concentration in the PECVD BSG diffusion source shall be

adjusted by increasing the $[\text{SiH}_4]/[\text{B}_2\text{H}_6]$ gas flow ratio so that the B concentration is below the solubility limit of B in Si and the BRL formation is prevented.

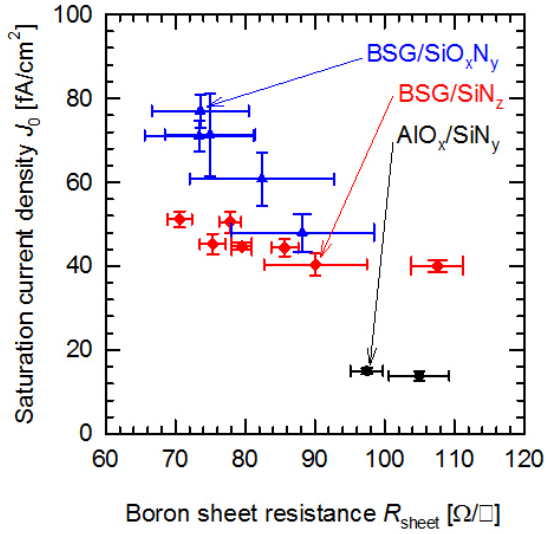
5.3 Passivation quality of PECVD BSG

After p^+ -emitter formation during co-diffusion from a PECVD BSG/ SiN_z or BSG/ SiO_xN_y stack, the diffused silicon surface needs to be passivated during cell fabrication. Up to now, this has been done by removing all dielectric layers in HF with a high concentration of 40% and deposition of $\text{AlO}_x/\text{SiN}_y$. These etching and deposition steps could be avoided and the processing of co-diffused solar cells could be further simplified by keeping the BSG and capping layer as a rear side passivation.

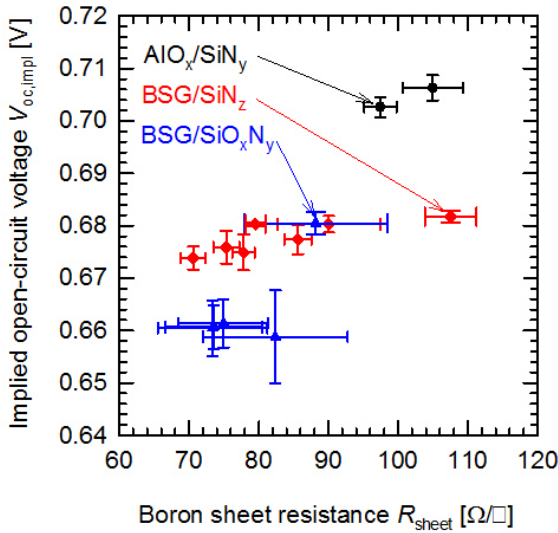
We evaluate the passivation quality of the PECVD BSG capped with either SiN_z or with PECVD SiO_xN_y by processing symmetrical samples on damage-etched and RCA-cleaned $156 \times 156 \text{ mm}^2$ n -type CZ silicon wafers with (100) orientation, with a starting thickness of $(170 \pm 20) \mu\text{m}$ and a resistivity of 5 to 6 $\Omega \text{ cm}$. The PECVD BSG layer with a thickness of 40 nm is deposited on both sides and it is capped with either 120 nm PECVD SiN_z or 300 nm SiO_xN_y . During the POCl_3 co-diffusion the B emitter is diffused from the solid BSG diffusion source on both wafer sides. A PSG etching is performed in HF with a low concentration of 1% for 90 s to remove only the PSG without removing the PECVD BSG and the capping layer.

To compare different passivation stacks, we also process symmetrically boron-diffused samples that are $\text{AlO}_x/\text{SiN}_y$ passivated after BSG-removal. Quasi-steady-state photoconductance (QSS-PC) measurements are performed before and after firing and the saturation current density J_0 , the inductively measured boron sheet resistance R_{sheet} and the implied open-circuit voltage $V_{oc,impl}$ are extracted.

Figure 5.17 shows (a) J_0 and (b) $V_{oc,impl}$ as a function of R_{sheet} for the different passivation stacks on the p^+ -emitter. The errorbars correspond to the standard deviation derived from measurements at nine different positions per $156 \times 156 \text{ mm}^2$ wafer. We achieve mean J_0 values of 40 to 51 fA/cm^2 and $V_{oc,impl}$ of 674 to 682 mV at boron sheet resistances R_{sheet}



(a)



(b)

Figure 5.17: (a) Saturation current density J_0 and (b) implied open-circuit voltage $V_{oc,impl}$ values for PECVD BSG and AlO_x/SiN_y passivation stacks on the p^+ -emitter after firing as a function of R_{sheet} .

of 71 to 108 Ω/\square with BSG/SiN_z stacks as diffusion source and passivation. For PECVD BSG/SiO_xN_y layers, the standard deviation of the measured R_{sheet} is increased due to the higher thickness inhomogeneity of the 300 nm-thick PECVD SiO_xN_y layer on 156 × 156 mm² area compared to a 120 nm-thick SiN_z layer. (The difference and variation in the PECVD layer thickness is optically distinguishable as a change in color, as can be seen in Fig. 6.11). This results in higher mean J_0 values for the BSG/SiO_xN_y stacks of 48 to 77 fA/cm² and corresponding lower $V_{oc,impl}$ of 659 to 681 mV with increased standard deviations compared to the BSG/SiN_z stacks. All J_0 data is measured both before (not shown in Fig. 5.17) and after firing at 850 °C. Neither an improvement nor a degradation is observed within the measurement uncertainty. This proves the firing stability of the BSG passivation. By removing the PECVD BSG and capping layer in HF after co-diffusion, RCA cleaning and passivating with an AlO_x/SiN_y stack, lowest J_0 results of 14 fA/cm² and highest $V_{oc,impl}$ values of 706 mV are reached.

We conclude that the PECVD BSG capped with PECVD SiN_z acts as an effective boron diffusion source resulting in boron emitters with homogeneous R_{sheet} that is applicable in solar cell fabrication. The BSG/SiN_z stack as emitter passivation does not yet reach the high passivation quality of AlO_x/SiN_y stacks, however, it simplifies the solar cell fabrication, as will be shown in 6.2.4.

5.3.1 Interface passivation mechanism

In order to investigate the fundamental passivation mechanism of (un)capped PECVD BSG on diffused and undiffused Si surfaces, a corona charge analysis, as described in 3.6, was performed for three different BSG passivated samples. The samples were charged in a corona chamber and lifetime measurements as well as measurements of the Kelvin voltage U_K were performed for each charging step. From the measurement data, the surface recombination velocity S_{eff} and the fixed charge density Q_f were extracted.

On three 156 × 156 cm² *n*-type Cz-Si wafers with a resistivity of 5-6.5 Ω cm, a PECVD BSG layer with a thickness of 40 nm and a gas flow ratio of [SiH₄]/[B₂H₆]=8% is deposited on both sides. On two samples, a

120 nm-thick SiN_z capping layer is deposited. One sample with PECVD BSG/ SiN_z is exposed to a co-diffusion so that a p^+ -emitter is formed during the B drive-in at 950 °C for 60 min. After PSG etching, the symmetrically diffused and passivated sample is fired at a peak temperature of 850 °C.

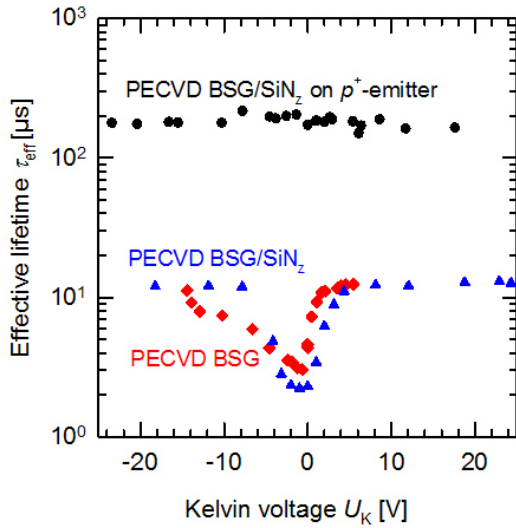
In Fig. 5.18(a) the effective lifetimes τ_{eff} , that are measured at an injection level of $1 \times 10^{14} \text{ cm}^{-3}$, are plotted as a function of the measured Kelvin voltage U_K . For both the PECVD BSG layer and the BSG/ SiN_z stack after deposition, low lifetimes of 2-5 μs are measured without corona charge that are increased to 13 μs with increasing charging steps and Kelvin voltage. After a POCl_3 co-diffusion, for the BSG/ SiN_z passivation stack on the p^+ -emitter lifetimes up to 216 μs are measured independent on the Kelvin voltage.

The surface recombination velocity S_{eff} and the corona charge density Q_{corona} are calculated according to equations 3.5 and 3.4 and plotted in Fig. 5.18(b). The effective surface recombination velocities of the unannealed samples show maximum values near $Q_{corona} = 0$ and decrease with increasing deposited corona charge $|Q_{corona}|$, similar to the calculated recombination rate shown in Fig. 3.4.

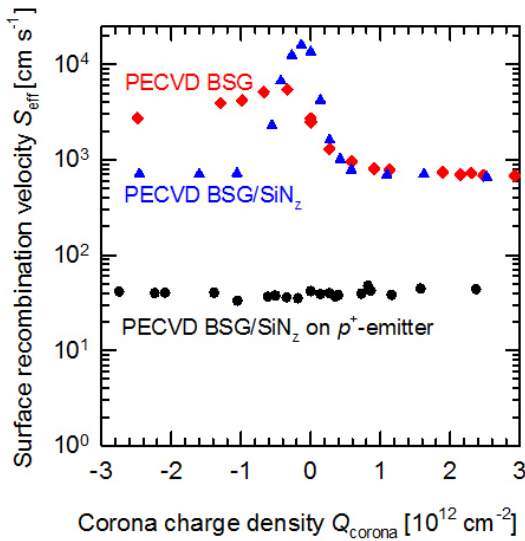
For the as-deposited BSG layer, a maximum value of $S_{eff} = 5500 \text{ cm s}^{-1}$ at a corona charge density $Q_{corona} = -3.3 \times 10^{11} \text{ cm}^{-2}$ is derived. For the as-deposited BSG/ SiN_z stack, S_{eff} reaches a maximum of 16000 cm s^{-1} at $Q_{corona} = -1.3 \times 10^{11} \text{ cm}^{-2}$.

From the charge densities $-Q_{corona}$ of the maximum S_{eff} values, the fixed charge density within the PECVD BSG passivation layer $Q_f = +(1.3-3.3) \times 10^{11} \text{ cm}^{-2}$ is derived. This positive fixed charge is in agreement with literature values for thermal oxides (see 2.4.1).

For the high-temperature annealed PECVD BSG/ SiN_z stack on the p^+ -emitter, a different behaviour is observed. Low S_{eff} values of $(34 \pm 2) \text{ cm s}^{-1}$ independent from the Kelvin voltage are identified. An average emitter saturation current density of $J_{0e} = 35 \text{ fA/cm}^2$ is derived from the measured lifetimes at an injection level of $1 \times 10^{15} \text{ cm}^{-3}$ with an estimated measurement uncertainty of 10%.



(a)



(b)

Figure 5.18: Corona charge analysis results for different PECVD BSG passivated n -type Cz-Si samples with and without SiN_z capping layer and diffusion process. (a) The effective lifetime τ_{eff} and the Kelvin voltage U_K are measured for each charging step. (b) The effective surface recombination velocity S_{eff} as a function of the deposited corona charge density Q_{corona} is extracted.

In order to evaluate and compare the passivation quality of the PECVD BSG on the p^+ -emitter, we extract the surface recombination velocity of electrons at the highly doped surface S_{n0} . The simulation tool EDNA 2 [Mc10] is applied to calculate J_{0e} from an experimental boron doping profile corresponding to the p^+ -emitter that is diffused from the PECVD BSG/SiN_z stack. After a POCl₃ co-diffusion with a boron drive-in step at 950 °C for 60 min, a surface boron concentration of $N_s=5 \times 10^{19} \text{ cm}^{-3}$, a profile depth of 0.6 μm and a boron sheet resistance of $R_{sheet}=80 \text{ }\Omega/\square$ are measured by ECV. As further input parameters, the resistivity of the n -type substrate wafer $\rho=5 \text{ }\Omega \text{ cm}$ and the derived fixed charge density $Q_f=+(1.3-3.3) \times 10^{11} \text{ cm}^{-2}$ are applied. By fitting the simulated J_{0e} to the experimental value, $S_{n0}=(1710 \pm 1370) \text{ cm s}^{-1}$ is determined. We assume a large uncertainty of 80% arising from the cumulated uncertainties of J_{0e} , of N_s and of Q_f .

In Fig. 5.19, S_{n0} results for different passivation layers on p^+ -emitter are plotted in dependence of N_s . Hoex et al. reported S_{n0} results for ALD Al₂O₃, SiN_x and thermal SiO₂ and found excellent passivation results for Al₂O₃ on highly p^+ -doped Si surfaces due to the high density of negative fixed charges (up to -10^{13} cm^{-2}) [Ho07]. The extracted S_{n0} for the PECVD BSG/SiN_z stack matches the results for thermal SiO₂ and is even lower than the S_{n0} values of SiN_x. For ALD Al₂O₃, only the maximum error bounds were extracted in [Ho07] and indicate lower S_{n0} results and thus a higher passivation quality on p^+ -emitters than the PECVD BSG.

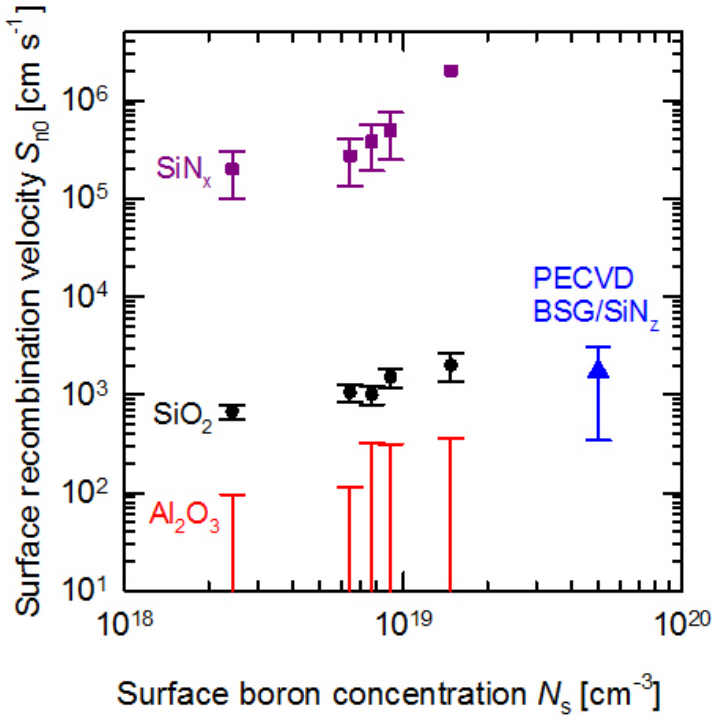


Figure 5.19: The surface recombination velocity on a p^+ -emitter S_{n0} for a BSG/ SiN_z passivation at a surface concentration of $N_s = 5 \times 10^{19} \text{ cm}^{-3}$ is derived and compared to S_{n0} results for ALD Al_2O_3 , SiN_x and thermal SiO_2 as reported in [Ho07].

To sum up, from the low lifetimes and high S_{eff} values of the unannealed samples, an insufficient passivation quality of the PECVD BSG layer on the Si substrate is concluded. After a high-temperature treatment of the PECVD BSG/ SiN_z stack, as applied during the POCl_3 co-diffusion, the passivation quality is significantly improved. The PECVD BSG passivation on the p^+ -emitter shows a passivation quality that is comparable to thermal SiO_x passivation layers. We speculate that during the diffusion process, a thin high-quality silicon dioxide layer is grown at the Si-BSG interface similar to a thermally grown oxide that is known for excellent passivation quality reaching S_{eff} values of $10\text{-}100 \text{ cm s}^{-1}$, as described in 2.4.1.

Chapter 6

Fabrication and characterization of solar cells

In the following Chapter, the fabrication of *n*-type solar cells and its simplification by applying a PECVD BSG diffusion source and a POCl_3 co-diffusion are discussed. First, we processed co-diffused front junction cells and demonstrated 17.5% efficiency on a small cell area of 4 cm^2 .

However, due to difficulties of the boron emitter formation from PECVD BSG on textured Si, we then focused on back junction cells with a boron emitter on the planar cell rear side. We processed simplified *n*-PERT BJ cells reaching a record high efficiency of 21.0% and compare them to reference PERT cells with separate diffusions and to *p*-PERC cells. A first module is fabricated from 12 co-diffused half cells and demonstrates an efficiency of 19.7%.

We also integrated the PECVD BSG diffusion source in the back-junction back-contact (BJBC) cell fabrication. An efficiency of 22.4% was demonstrated for a separate boron-drive in and POCl_3 diffusion. But when the co-diffusion was applied, shunting problems arose and only 15.4% efficiency could be reached.

The achieved passivation quality of a PECVD BSG/ SiN_x stack was applied to further simplify the *n*-PERT BJ cell process by keeping the BSG/ SiN_x stack as rear side passivation and thus saving etching and AlO_x deposition steps. In addition, an Al grid was screen-printed on the rear side. Thus, bifacial co-diffused rear emitter cells, that we name BiCoRE cells,

were developed and fabricated with an efficiency of 20.6% and a bifaciality factor of 78%. In a UV stability test, the BiCoRE rear side passivation showed no degradation. These simplified n -type cells have a comparable process complexity as industrial p -type PERC cells, however, on the long term they have a higher efficiency potential due to the used LID-stable n -type silicon substrate.

6.1 Co-diffused front junction cells

During conventional fabrication of high-efficiency front junction (FJ) solar cells, a large number of process steps is usually necessary for creating structured or single-side emitter and back surface field (BSF) regions. The process steps include at least two high-temperature furnace diffusions, each accompanied with depositing and removing capping layers. Resource, cost and time efficient production processes may be achieved by using solid diffusion sources deposited by means of plasma-enhanced chemical vapour deposition (PECVD): The PECVD diffusion sources are deposited one-sided, and in only one co-diffusion process, the dopant atoms from the PECVD layer are driven in while simultaneously a second doping type is diffused from the gas phase as already demonstrated in [Ba11].

Alternatively, PECVD layers with different doping types can be deposited on both sample sides and act as diffusion sources in a high-temperature step, so that the different doping profiles can be controlled and optimised independently as shown in [Ro13] and [Ca14]. Multifunctional PECVD layer stacks can also be used for surface passivation and as anti-reflective coating as demonstrated in [Se13] and [En15].

6.1.1 n -PERT FJ solar cells

We focus on growing PECVD BSG layers on n -type alkaline textured silicon substrates and applying a POCl_3 co-diffusion, relevant for fabricating bifacial n -type Passivated Emitter and Rear, Rear Totally doped (n -PERT) front junction (FJ) solar cells.

CVD BSG layers combined with a POCl_3 co-diffusion have already been applied to *n*-PERT FJ solar cells by different working groups, reaching conversion efficiencies up to 19.9% in 2014 for the co-diffused bifacial *n*-type CoBiN cell using an APCVD (atmospheric pressure CVD) BSG [Ro14] and 20.1% in 2014 for the bifacial SOLENNA cell applying PECVD $\text{SiO}_2\text{:B}$ [Ca14].

n-PERT FJ cell processing

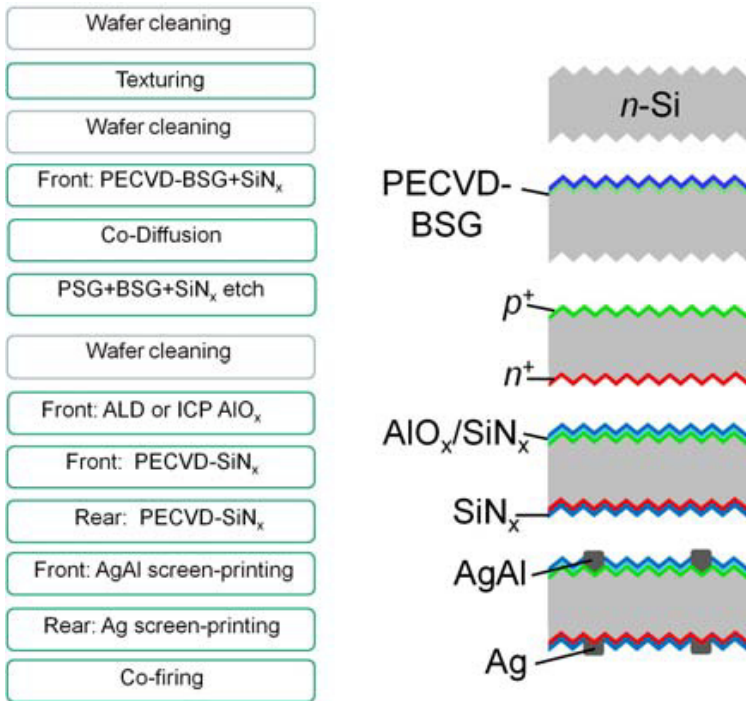


Figure 6.1: Simplified fabrication of bifacial *n*-PERT FJ solar cells. Using PECVD BSG layers allows to form the boron emitter and the phosphorus BSF simultaneously in a POCl_3 co-diffusion process. Only one high-temperature step and one protection layer are needed.

Our first *n*-PERT FJ cells with a PECVD BSG diffusion source were fabricated with the simplified processflow shown in Fig. 6.1. A $156 \times 156 \text{ mm}^2$ *n*-type Czochralski-grown (Cz) silicon substrate with a specific re-

sistivity of $5.5 \Omega \text{ cm}$ and a thickness of about $160 \mu\text{m}$ after alkaline texture is used as base material. A PECVD BSG with a thickness of 80 nm and a gas flow ratio of $[\text{SiH}_4]/[\text{B}_2\text{H}_6]=6\%$ and a SiN_x capping layer with a thickness of 100 nm are deposited. A POCl_3 co-diffusion with a boron drive-in step at $1000 \text{ }^\circ\text{C}$ for 60 min is applied. Resulting BSG and PSG layers are removed in hydrofluoric acid (HF) and the front and rear surfaces are passivated by a 100 nm thick $\text{AlO}_x/\text{SiN}_x$ stack and a SiN_x layer, respectively. For metallization, AgAl and Ag screen-printing with a 3-busbar layout are used and co-fired. For the characterisation of the cells, current- voltage (IV) measurements are performed using the LOANA Solar Cell Analysis System (pvtools) [LO15].

n-PERT FJ cell results

From the IV measurements of the first fabricated bifacial *n*-type PERT FJ cells the cell parameters shown in Tab. 6.1 are extracted.

Cell concept	η [%]	FF [%]	pFF [%]	J_{sc} [mA/cm^2]	V_{oc} [mV]	R_s [Ωcm^2]	A [cm^2]
<i>n</i> -PERT FJ co-diffused small-area	17.5	72.9	78.2	37.9	633	2.5	4.0
<i>n</i> -PERT FJ co-diffused large-area	4.3	26.7	78.2	25.3	636	22.8	239

Table 6.1: Results of the first co-diffused, all-screen-printed, bifacial *n*-type PERT FJ cells we fabricated in a simplified manner with PECVD BSG as diffusion source.

For these first bifacial *n*-PERT FJ cells fabricated in 2013 applying a PECVD BSG diffusion source, a co-diffusion and all-screen-printed metallization, an efficiency of $\eta=17.5\%$ was demonstrated on a cell area of 4 cm^2 . The large-area cell reached only 4.3% efficiency resulting from the low fill factor of 26.7% . A pseudo fill factor of 78.2% was measured and the FF was reduced by the high series resistance of $22.8 \Omega \text{ cm}^2$.

This cell was further characterized applying luminescence imaging and SEM. By means of electroluminescence (EL) imaging, charge carriers are excited electrically and the luminescence emission of the cell arising from radiative recombination is measured spatially resolved. Further details about the luminescence measurement technique can be found in [Hi11].

The EL image in Fig. 6.2 shows areas with a high luminescence signal intensity only in the lower right corner. SEM images from this cell area reveal a continuous boron emitter on the textured silicon substrate that is shown in Fig. 6.3(b) and comparable to Fig. 5.14(c). However, the boron diffusion in the upper left cell area is inhomogeneous and interrupted, as visible in Fig. 6.3(a). The 17.5% efficient 4 cm² *n*-PERT FJ cell was laser-cut from the intact area of the large-area cell as a proof-of-concept cell, as indicated in red in Fig. 6.2.

We conclude that there are some requirements to the emitter and BSF of a bifacial high-efficiency *n*-PERT FJ cell with reduced process steps that we need to fulfill by optimising the deposition of our PECVD stacks and the co-diffusion process: the PECVD BSG and capping layers have to be deposited homogeneously to form a continuous boron emitter on alkaline textured *n*-type silicon, as already discussed in 5.2.4. The emitter needs to have a sufficient thickness and surface concentration to allow efficient metallization. But the boron concentration in the BSG layer must be kept low enough to prevent BRL formation (see 5.2.5) so that no additional LTO and HF etch are needed.

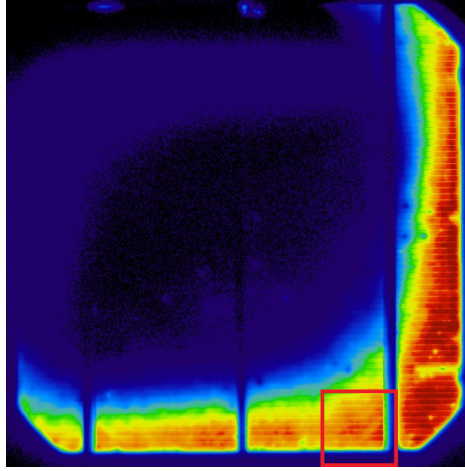


Figure 6.2: EL image (measured at V_{oc}) of the first fabricated large-area ($156 \times 156 \text{ mm}^2$) bifacial 4.3% efficient n -PERT FJ cell applying a PECVD BSG diffusion source on a textured Cz-Si substrate and a POCl_3 co-diffusion. A low EL signal is measured for the main cell area that is attributed to a nonhomogeneous boron diffusion. Only the lower right cell area is intact from that the 17.5% efficient 4 cm^2 cell was laser-cut.

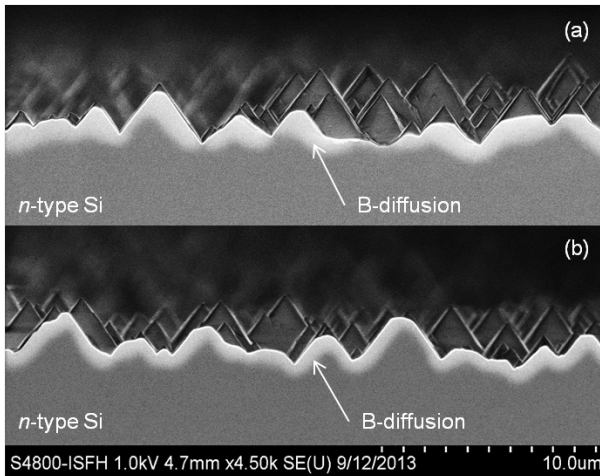


Figure 6.3: SEM image of the boron diffusion from a 80 nm-thick PECVD BSG diffusion source with $[\text{SiH}_4]/[\text{B}_2\text{H}_6]=6\%$ on the textured front side of the first fabricated n -PERT FJ cell (a) from the upper left cell area where the B diffusion is interrupted and (b) from the intact lower right cell area.

6.2 Co-diffused back junction cells

In order to prevent the difficulties arising from PECVD and emitter formation on textured silicon with our deposition tools and furnace process, we chose a different cell concept that uses a PECVD BSG diffusion source on a planar n -type silicon substrate for the formation of a rear side emitter.

In this thesis, we apply PECVD BSG diffusion sources combined with a POCl_3 co-diffusion process as an alternative approach to introduce the p^+ -emitter on the planar rear side and the n^+ -FSF on the textured front side of the n -PERT BJ cells.

We also integrate the PECVD BSG diffusion source in the fabrication process of high-efficiency back-junction back-contact (BJBC) cells.

6.2.1 n -PERT BJ solar cells

The PERT cell in back junction (BJ) configuration is an n^+np^+ device. This n -PERT BJ cell has a similar structure as the Passivated Emitter and Rear Cell (PERC) in front junction configuration (see Fig. 6.4). The PERC concept, that is based on p -type silicon substrates and is thus an n^+pp^+ device, is expected to become a major industrial solar cell technology [IT16]. With a lean process flow, efficiencies of up to 22.13% [Ye16] could be demonstrated very recently. However, the efficiencies of PERC solar cells typically decrease due to light-induced degradation (LID) of the p -type silicon used as base material [Sc04].

The n -PERT BJ cell is an attractive cell concept which combines the advantages of n -type silicon (no LID, high bulk lifetime [Sc07]) and of a process flow that is very similar to industrial p -PERC cells. The PERT BJ fabrication has the potential to be further simplified and to be implemented in existing PERC production lines.

The main difference between the two cell concepts is the n -type substrate and the full-area boron diffusion at the rear of the PERT BJ cell, which acts as the emitter. In laboratory-scale processing, this emitter is commonly formed during a BBr_3 furnace diffusion which is followed by the deposition of a dielectric layer. This layer protects the emitter during the following front-side texturing and POCl_3 diffusion to form the n^+ -front

surface field (FSF). Thus, two additional process steps are applied: (1) the BBr_3 diffusion and (2) the deposition of a protection layer.

Until now, n -PERT BJ cells applying BBr_3 and POCl_3 furnace diffusions have demonstrated conversion efficiencies up to 22.5% using Ni/Cu/Ag plating on the front side and AlSi sputtering on the rear side for metallization [Ur15] and with screen-printed contacts up to 21.8% [Bo16].

We apply PECVD BSG diffusion sources and a POCl_3 co-diffusion process for the simplified fabrication of n -PERT BJ cells.

n -PERT BJ cell processing

For the simplified fabrication of monofacial n -PERT BJ cells, we use n -type $156 \times 156 \text{ mm}^2$ Cz silicon wafers with (100) orientation, a starting thickness of $(180 \pm 20) \mu\text{m}$ and a resistivity of 5 to 6 $\Omega \text{ cm}$ (after high-temperature treatment). The wafers are etched in KOH for saw damage removal and are subsequently RCA-cleaned. 40 nm-thick PECVD BSG with a gas flow ratio of $[\text{SiH}_4]/[\text{B}_2\text{H}_6] = 8\%$ is deposited on the planar rear side and capped with a 170 nm-thick PECVD SiN_z layer (SiNA, Meyer Burger). The PECVD BSG/ SiN_z stack acts as an etch barrier during alkaline texturing and as a diffusion barrier during the following POCl_3 co-diffusion. After removal of all dielectric layers in HF, the rear side is passivated by a stack of 5 nm AlO_x deposited by spatial atomic layer deposition (ALD) (InPassion LAB tool, SoLayTec) and 100 nm SiN_y . On the front side, a PECVD SiN_y layer acts as passivation and as anti-reflective coating (ARC). After laser contact opening (LCO) on the rear side, the front side metallization is performed by Ag-screen printing applying a 5 busbar layout and a dual-print process as described in [Ha14]. Full-area Al-screen-printing on the rear side and co-firing finalize the cell process. For comparison, n -PERT BJ reference cells using sequential BBr_3 and POCl_3 diffusions are also fabricated as described in [Li16].

Fig. 6.4 compares the process flows for our co-diffused n -PERT BJ cells and for n -PERT BJ reference cells using sequential BBr_3 and POCl_3 diffusions with p -PERC cells according to [Ha14].

<i>n</i> -type PERT BJ co-diffused	<i>n</i> -type PERT BJ reference	<i>p</i> -type PERC FJ
Wafer cleaning	Wafer cleaning	Wafer cleaning
	B-diffusion	
	BSG etch	
PECVD BSG+SiN _z	Rear protection layer	Rear protection layer
Texturing	Texturing	Texturing
Co-diffusion	P-diffusion	P-diffusion
PSG+BSG+SiN _z etch	PSG+dielectric etch	PSG+dielectric etch
Rear: AlO _x +SiN _y pass.	Rear: AlO _x +SiN _y pass.	Rear: AlO _x +SiN _y pass.
Front: SiN _y pass.	Front: SiN _y pass.	Front: SiN _y pass.
Laser contact opening	Laser contact opening	Laser contact opening
Front: Ag screen-print.	Front: Ag screen-print.	Front: Ag screen-print.
Rear: Al screen-print.	Rear: Al screen-print.	Rear: Al screen-print.
Co-firing	Co-firing	Co-firing
11 steps	13 steps	11 steps

Figure 6.4: Schematic diagrams and process steps for *n*-PERT BJ cells (left) using either PECVD BSG diffusion sources and POCl₃ co-diffusions or sequential diffusions (middle) compared with *p*-PERC FJ cells (right). The main difference is the use of *n*-type wafers and the additional boron rear-side doping for *n*-PERT BJ cells. The similar process flow eases the production implementation of *n*-PERT BJ as upgrade of *p*-PERC FJ production lines.

n-PERT BJ cell results

A finished monofacial *n*-PERT BJ cell is shown in Fig. 6.5.

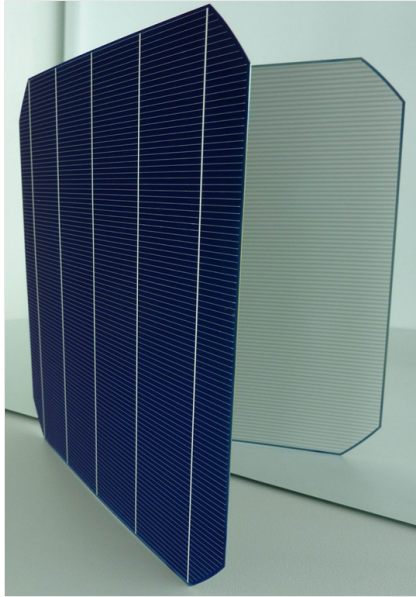


Figure 6.5: Monofacial *n*-PERT BJ cell with Ag-screen-printed front contacts applying a 5-busbar layout and full-area Al-screen-printing on the rear side.

Table 6.2 compares the cell results for *n*-type PERT BJ cells applying PECVD BSG and co-diffusion and *n*-PERT BJ reference cells using sequential diffusions [Li16] with previously reported cell results for *p*-type PERC cells [Ha14]. For all cell concepts efficiencies above 21% are reached when a 5-busbar layout as described in [Ha14] is applied. The optimization of the PECVD BSG diffusion source results in independently confirmed conversion efficiencies of 21.0% for the best cell and also as an average (in-house-measured) efficiency indicating a reliable fabrication process. The efficiency is almost as high as that of the reference *n*-PERT BJ cell with separate diffusions, despite of the reduced number of process steps (compare Fig. 6.4). Note that the *n*-PERT BJ solar cells yield notably higher open-circuit voltages than the *p*-PERC solar cells due to the lower bulk recombination of the *n*-type substrates.

Cell concept	η [%]	FF [%]	J_{sc} [mA/cm ²]	V_{oc} [mV]
<i>n</i> -PERT BJ co-diffused average parameters	21.0* (21.02±0.05)	80.5 (81.2±0.2)	39.1 (38.92±0.04)	666 (665±1)
<i>n</i> -PERT BJ reference [Li16]	21.2*	80.0	39.3	674
<i>p</i> -PERC [Ha14]	21.2*	80.9	39.6	661

* Independently confirmed by Fraunhofer ISE CaLab.

Table 6.2: Cell results for *n*-PERT BJ and *p*-PERC cells obtained on a cell area of 239 cm² with 5-busbar layout. The average IV parameters and their standard deviations of 6 co-diffused cells are indicated in brackets.

Cell concept	η [%]	FF [%]	J_{sc} [mA/cm ²]	V_{oc} [mV]
<i>n</i> -PERT BJ reference	20.6	79.6	39.0	663
<i>n</i> -PERT BJ reference (after LID)	20.5	79.3	39.0	664
<i>p</i> -PERC [Li14]	20.6*	80.5	38.8	658
<i>p</i> -PERC (after LID) [Li14]	19.7	80.1	38.1	645

* Independently confirmed by Fraunhofer ISE CaLab.

Table 6.3: IV parameters for reference *n*-PERT BJ and *p*-PERC cells obtained on a cell area of 239 cm² with 3-busbar layout before and after complete LID by illumination at room temperature for 16 h.

Table 6.3 summarizes the IV parameters of a 3-busbar reference *n*-PERT BJ cell and a 3-busbar *p*-PERC cell measured before and after complete LID. The PERC cell suffer from LID and loses 0.9%_{abs.} in efficiency after 16 h of illumination at room temperature due to the degradation of the *p*-type silicon substrate. The PERT BJ cell using an *n*-type silicon substrate keeps the high performance under illumination: $\Delta\eta = \pm 0.1\%$ _{abs.} is measured after 16h of illumination, which is within the measurement uncertainty, as also reported in [Li14].

To sum up, a confirmed efficiency of 21.0% is reached with a reduced number of process steps when compared to the reference case with separate diffusions. Only one high temperature step is required. Hence, co-

diffused n -PERT BJ cells can be produced with comparable time effort as p -PERC cells and fully avoid performance losses by LID. The efficiency of 21.0% is the highest efficiency reported so far (published in January 2016) for co-diffused screen-printed n -PERT BJ cells applying PECVD BSG.

6.2.2 n -PERT BJ module

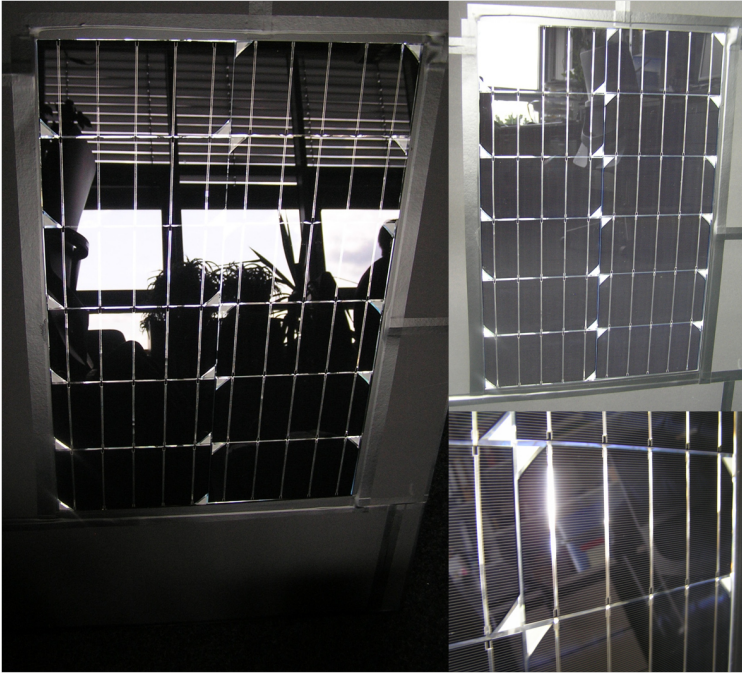


Figure 6.6: The first module from 12 co-diffused n -PERT BJ half cells demonstrates 19.7% efficiency and an output power of 29.7 W.

We fabricate a demonstration module from our best co-diffused n -PERT BJ cells, that is shown in Fig. 6.6. Ag solder pads are screen-printed on the rear side and the Al rear side and Ag front side metallizations are performed by dual print with a 5-busbar half cell layout. After firing, the cells are laser-cut into half cells. 12 half cells with an average cell efficiency of $(20.9 \pm 0.1)\%$ are connected in two strings, laminated

in ethylene vinyl acetate (EVA) foil and covered with a glass plate. The cell spacings and the connectors are covered with a reflective foil to direct the incident light on the cell area and thus to minimize reflection losses. Under standard testing conditions, a module efficiency of 19.7% is measured so that a cell to module loss $<6\%_{rel.}$ is reached. This first n -PERT BJ module demonstrated an open-circuit voltage V_{oc} of 7.9 V and a short circuit current I_{sc} of 4.7 A and a power output at the maximum power point P_{mpp} of 29.7 W.

6.2.3 Simplified BJBC cells

In this thesis, we also evaluate the integration of the PECVD BSG diffusion source and the POCl_3 co-diffusion process in the fabrication of a high-efficiency cell concept. For advanced back-junction back-contact (BJBC) cells, the highest reported efficiency of 25.2% [Gr16] has been demonstrated with high process effort and cost. Keding et al. demonstrated a process simplification by applying prepatterned solid diffusion sources and a co-diffusion and reported 20.2% efficient industrially feasible BJBC cells [Ke13].

We fabricate BJBC cells, as schematically shown in Fig. 6.7, applying PECVD BSG as a boron diffusion source. In first experiments, the boron drive-in is performed separately. The cell processing steps are similar to [SH15] and listed in Fig. 6.8 (left column).

The n^+ -BSF is formed on n -type mono Cz-Si $1.5 \Omega \text{ cm}$ Si wafers during a POCl_3 diffusion. After the laser ablation of an SiN_x capping layer and the subsequent KOH etching (emitter patterning), PECVD BSG is deposited, and the boron is driven-in at $1000 \text{ }^\circ\text{C}$ for 30-60 min to form the p^+ -emitter.

For the fabrication of co-diffused BJBC cells (see Fig. 6.8 right column), the PECVD BSG is deposited on planar $15.6 \times 15.6 \text{ cm}^2$ n -type Cz-Si wafers and capped with PECVD SiN_x . After the patterning of the rear side by laser structuring and KOH etching (BSF patterning), the POCl_3 co-diffusion is performed to generate both the p^+ -emitter and n^+ -BSF in a single high-temperature step.

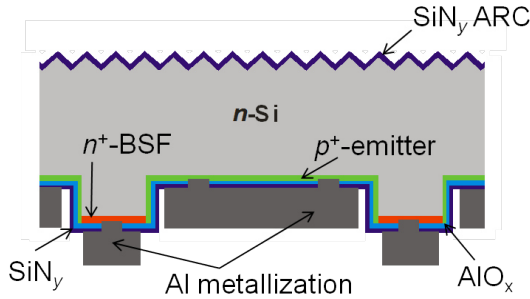


Figure 6.7: Schematic diagram of a BJBC solar cell [SH15]. The fabrication can be simplified by applying a PECVD BSG boron diffusion source and a POCl_3 co-diffusion process.

<i>n</i> -type BJBC separate diffusions	<i>n</i> -type BJBC co-diffusion
Wafer cleaning	Wafer cleaning
P-diffusion	
PSG etch	
SiN_z protection layer	PECVD BSG+ SiN_z
Laser structuring	Laser structuring
KOH etching	KOH etching
PECVD BSG	
B drive-in	Co-diffusion
BSG etch	PSG+BSG+ SiN_z etch
Front: SiN_y passivation	Front: SiN_y passivation
Rear: AlO_x + SiN_y pass.	Rear: AlO_x + SiN_y pass.
Laser contact opening	Laser contact opening
Rear: Al evaporation	Rear: Al evaporation
Contact separation	Contact separation
14 steps	11 steps

Figure 6.8: Processing steps for *n*-type BJBC cells using PECVD BSG as a boron diffusion source with separate POCl_3 diffusion and B drive-in (left) and with POCl_3 co-diffusion (right).

For both types of BJBC cells, PECVD SiN_y is deposited on the textured front side as surface passivation and as an antireflective coating. The rear side is passivated with a layer of ALD- AlO_x capped by a PECVD SiN_y layer. Laser contact openings are prepared by ablation of these layers. The rear side of the cells is metallized by Al evaporation followed by a self-aligned wet chemical separation of the emitter and BSF regions.

For the BJBC cells using PECVD BSG as a diffusion source, the measured IV parameters are listed in Tab. 6.4. An efficiency of up to 22.4% on a cell area of 4 cm^2 and of 20.0% on a $12.5 \times 12.5 \text{ cm}^2$ cell is demonstrated when the boron drive-in and the POCl_3 diffusion are performed separately. This shows that the PECVD BSG diffusion source can successfully be implemented in the fabrication process of high-efficiency solar cell concepts. The boron drive-in from the single-sided diffusion source replaces a boron furnace diffusion and thus saves the deposition of a front side protection layer and reduces the total processing steps compared to [SH15]. The PECVD BSG-diffused cells - especially on a large cell area - do not yet reach the performance of the reference cells processed with separate furnace diffusions which might be attributed to an inhomogeneous PECVD deposition on the structured silicon substrates.

The first co-diffused BJBC solar cells show high short-circuit current densities of up to $J_{sc}=39.3 \text{ mA/cm}^2$ and moderate open-circuit voltages V_{oc} of up to 652 mV. However, they suffer from very low shunt resistances of $0.11 \text{ k}\Omega \text{ cm}^2$ which reduce the pseudo fill factor pFF to 66% resulting in low efficiencies of about 15%. Thus, further optimization is needed to realize the full potential for process simplification, that is indicated in Fig. 6.8, by applying PECVD BSG diffusion sources and POCl_3 co-diffusion during BJBC cell fabrication.

Cell concept	η [%]	FF [%]	pFF [%]	J_{sc} [mA/cm ²]	V_{oc} [mV]	R_s [Ω cm ²]	A [cm ²]
<i>n</i> -BJBC, B drive-in	22.4	81.7		40.6	675		4
<i>n</i> -BJBC, co-diffusion	15.4	60.0	66.0	39.3	652	1.52	4
<i>n</i> -BJBC, reference	22.9	82.0		40.9	681		4
<i>n</i> -BJBC, B drive-in	20.0	75.8	82.1	39.6	667	1.29	156
<i>n</i> -BJBC, reference	21.2	77.0		40.2	686		156

Table 6.4: Cell results for *n*-BJBC cells fabricated with PECVD BSG as diffusion source, either with separate B drive-in and POCl₃ diffusion or with a co-diffusion process. For comparison, the results of reference BJBC cells with separate furnace diffusions for two different cell areas are also listed.

6.2.4 BiCoRE solar cells

On the way to further process simplification and integration into industrial production, as an advancement of the n -PERT BJ cells we introduced a BSG passivation and a bifaciality in our cell concept.

We fabricated n -type rear emitter cells with a multifunctional PECVD BSG/SiN_z stack, acting both as a boron diffusion source and as the rear side passivation: The PECVD diffusion source is not removed after co-diffusion but remains on the rear side emitter as a passivation layer and also as anti reflective coating (ARC). To fabricate bifacial cells, a screen-printed Al grid is applied on the rear side.

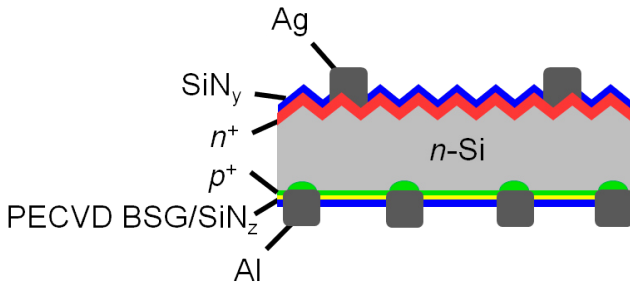


Figure 6.9: Schematic of the Bifacial Co-diffused Rear Emitter (BiCoRE) cell with PECVD BSG/SiN_z as rear-side diffusion source and passivation.

We name our n^+np^+ solar cell concept shown in Fig. 6.9 BiCoRE (Bifacial Co-diffused Rear Emitter) cell. The process flow of the BiCoRE cell is as lean as an industrial PERC process. The BiCoRE cell is a potentially very attractive candidate for p -PERC solar cell manufacturers to migrate to LID-free n -type Cz-Si wafers and bifacial solar cells with only minimal changes to their existing production tools and process recipes.

BiCoRE cell processing

The process flow for the fabrication of BiCoRE cells and of monofacial n -CoRE cells is summarized in Fig. 6.10 (left column). $156 \times 156 \text{ mm}^2$ n -type Cz silicon wafers with (100) orientation with a starting thickness of $(170 \pm 20) \mu\text{m}$ and a resistivity of 5 to 6 $\Omega \text{ cm}$ are damage-etched in

<i>n</i> -(Bi)CoRE	<i>n</i> -PERT BJ reference	<i>p</i> -PERC FJ
Wafer cleaning	Wafer cleaning	Wafer cleaning
	B-diffusion	
	BSG etch	
PECVD BSG+SiN _z /SiO _x N _y	Rear protection layer	
Texturing	Texturing	Texturing
Co-diffusion	P-diffusion	P-diffusion
PSG etch	PSG+dielectric etch	Polishing+PSG etch
	Rear: AlO _x +SiN _y pass.	Rear: AlO _x +SiN _y pass.
Front: SiN _y pass.	Front: SiN _y pass.	Front: SiN _y pass.
Laser contact opening	Laser contact opening	Laser contact opening
Front: Ag screen-print.	Front: Ag screen-print.	Front: Ag screen-print.
Rear: Al screen-print.	Rear: Al screen-print.	Rear: Al screen-print.
Co-firing	Co-firing	Co-firing
10 steps	13 steps	10 steps

Figure 6.10: The process flow for bifacial *n*-BiCoRE and monofacial *n*-CoRE cells applying co-diffusion and BSG passivation is compared to *n*-PERT BJ reference cells using separate furnace diffusions and to industrial *p*-PERC FJ cells.

KOH and RCA-cleaned. The PECVD BSG layer with a thickness of 40 nm is deposited on the rear side. It is capped with 120 nm PECVD SiN_z (SiNA tool). Alternatively, a double layer of 40 nm BSG and 300 nm SiO_xN_y is deposited in a single PECVD recipe. During the following texturing, the BSG/SiN_z or BSG/SiO_xN_y stack acts as etching barrier. During the POCl₃ co-diffusion (see Fig. 4.2) the B emitter is diffused from the solid BSG diffusion source and the phosphorus FSF is diffused from the gas phase. After PSG etching in HF, only the front side needs to be passivated by 100 nm PECVD SiN_y, the BSG/SiN_z or BSG/SiO_xN_y stack is kept as rear side passivation. We perform laser contact opening and metalize the cell by Ag screen-printing on the front side with a 5-busbar layout. We screen print an Al grid on the rear side in order to

achieve bifacial (BiCoRE) cells or full area Al for monofacial (CoRE) cells. Co-firing finishes the cells. For comparison of different passivation stacks on the p^+ -emitter, we also process BiCoRE cells with a stack of 5 nm-thin atomic-layer-deposited AlO_x and 100 nm PECVD SiN_y on the rear side.

Figure 6.10 compares the lean BiCoRE cell process with BSG passivation to n -PERT BJ reference cells that are processed with separate B and P diffusions and with industry-typical p -PERC front junction cells. The BiCoRE cells have a very similar process flow as industrial PERC cells so that they can be implemented in existing processing lines with only minor changes to the tool set. The BiCoRE process complexity is comparable to that of PERC cells but due to the n -type substrate wafer they potentially may obtain higher efficiencies.

BiCoRE cell results

Photographs of n -BiCoRE cells with either a PECVD BSG/ SiN_z or BSG/ SiO_xN_y rear side passivation are shown in Fig. 6.11.

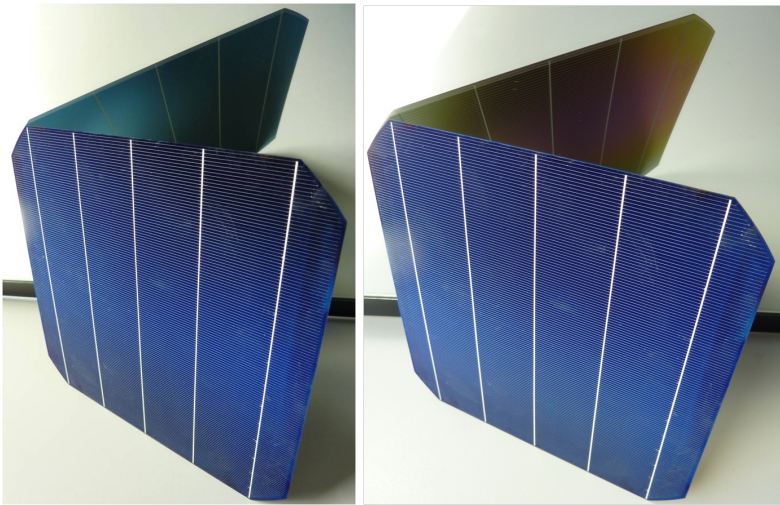


Figure 6.11: Bifacial n -BiCoRE cell with a BSG/ SiN_z or BSG/ SiO_xN_y rear side passivation and with screen-printed Ag front contacts and Al rear contacts applying a 5-busbar layout.

The change in color of the BSG/SiO_xN_y passivated cell results from the thickness inhomogeneity of our PECVD tool, as already discussed in 5.2.2 and 5.3. The target thickness of the SiO_xN_y layer of 300 nm is reached in the center of the 156 × 156 mm² wafer, towards the edges the thickness is reduced by about 10-30% to a layer thickness down to about 210 nm. This large thickness variation of the PECVD stack is visible as a change in color from violet in the center to yellow at the edges.

Table 6.5 summarizes the cell results of our best *n*-type BiCoRE, monofacial CoRE and the PERT BJ reference cells measured on a brass chuck. 20.6% efficiency is demonstrated for our new BiCoRE cell concept and 20.6% efficiency is reached for the monofacial CoRE cells, both with BSG rear side passivation. The AlO_x-passivated and the BSG-passivated BiCoRE cells reach comparable V_{oc} values of 668-671 mV and efficiencies of 20.6%. The reduced efficiency of the BSG/SiO_xN_y-passivated cell of 20.4% is attributed to the increased series resistance $R_s=1.4 \Omega \text{ cm}^2$ that reduces the fill factor to 77.4%. The BSG/SiO_xN_y-passivated cell reaches the highest short-circuit current density $J_{sc}=39.4 \text{ mA/cm}^2$. Thus, good cell results are reached both for an AlO_x and a BSG rear side passivation regardless of the PECVD thickness inhomogeneity.

A comparison of the BiCoRE and the monofacial CoRE cells shows that the bifacial cells reach 0.2-0.6 mA/cm² higher short-circuit current densities and about 3-6 mV higher V_{oc} values. A bifaciality of up to 78% is measured for the BiCoRE cells both on a brass and a black (not shown in Table 6.5) measurement chuck.

Compared to the bifacial *n*-PERT BJ reference cell reaching 21.1% efficiency and 78% bifaciality, the best 20.6% efficient *n*-BiCoRE cell with AlO_x/SiN_y-passivation suffers from the high series resistance $R_s=1.2 \Omega \text{ cm}^2$ that reduces the fill factor to 78.4%. We attribute the increased R_s to the P FSF, thus the co-diffusion needs to be optimized aiming for lower and homogeneously distributed P sheet resistances that can effectively be contacted by Ag screen-printing.

Cell type	Diffusion	Metallization rear side	Passivation rear side	η [%]	FF [%]	J_{sc} [mA/cm ²]	V_{oc} [mV]	R_s [Ω cm ²]
BiCoRE	PECVD BSG		BSG/SiN _z	20.6	78.5	39.2	668	1.0
BiCoRE	co diffusion	bifacial, Al grid	BSG/SiO _x N _y	20.4	77.4	39.4	670	1.4
BiCoRE			AIO _x /SiN _y	20.6	78.4	39.2	671	1.2
CoRE			BSG/SiN _z	20.6	80.1	38.8	664	0.6
CoRE	PECVD BSG	monofacial, full Al	BSG/SiO _x N _y	20.7	80.0	39.0	664	0.74
CoRE	co diffusion		AIO _x /SiN _y	20.7	79.2	39.0	668	0.98
PERT BJ	BBr ₃ /POCl ₃	bifacial, Al grid	AIO _x /SiN _y	21.1	79.2	39.5	674	0.96
PERT BJ		monofacial, full Al		21.0	80.2	39.1	670	0.71

Table 6.5: Results of the best n -type BiCoRE and monofacial CoRE cells with BSG/SiN_z, BSG/SiO_xN_y and AIO_x/SiN_y rear side passivation, respectively, compared to n -type PERT BJ reference cells with separate diffusions. All measurements are performed in-house on a brass chuck.

We conclude that although the PECVD BSG/SiN_z and BSG/SiO_xN_y stack as emitter passivation does not yet reach the high passivation quality of AlO_x/SiN_y stacks, as discussed in 5.3, on cell level the impact on cell performance is currently negligible. As it simplifies the solar cell fabrication significantly (compare Fig. 6.10), it is an attractive option for the industrialization of the BiCoRE cells.

The bifaciality of the BiCoRE cell of 78% is relatively low and results from the rear side efficiency of 16.1% that is significantly smaller than the front side efficiency of 20.6%. The cell front side is optimized concerning the optical properties by applying a textured silicon surface with a random pyramid texture and a SiN_y passivation layer that also acts as ARC in order to minimize reflection losses. The rear side of the BiCoRE cells is planar and passivated with the capped PECVD BSG. Thus, the rear side is optimized concerning the boron diffusion formed during co-diffusion and the simplification of the cell processing. To further improve the BiCoRE cells, the rear side needs to be optimized concerning optical losses by adjusting thickness and refractive index of the PECVD layer stack so that it acts as ARC and by potentially applying a random pyramid structure for better light harvesting.

6.2.5 UV stability of BiCoRE solar cells

The long-term stability of the fabricated BiCoRE cells under UV illumination is evaluated. Therefore, four cells with different rear side passivation layer stacks are placed under a cover glass and either the cell front side or the rear side is exposed to ultra violet (UV) irradiation in the wavelength domain of 300-600 nm. The measured spectrum of the used lamps (UVASPOT, Höhnle) is plotted in Fig. 6.12 together with a terrestrial reference air mass 1.5 (AM1.5) spectrum [AS12].

The solar cells are exposed to 2000 h of UV illumination with an average illumination intensity of $(278 \pm 11) \text{ W m}^{-2}$. A total UV dose of $(583 \pm 27) \text{ kW h m}^{-2}$ is calculated that corresponds to an equivalent illumination time under AM1.5 solar irradiance of $(12600 \pm 600) \text{ h}$ (≈ 18 months). The measured transmittance of the cover glass is also plotted in Fig. 6.12. From the half maximum transmittance, a cut-off wavelength of $(318 \pm 2) \text{ nm}$ is derived. Thus, the cover glass is transparent for the full spectrum

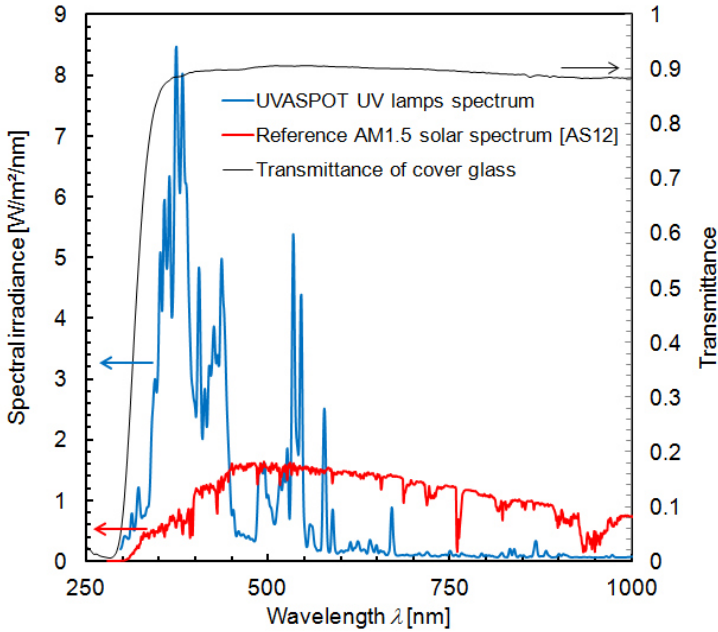


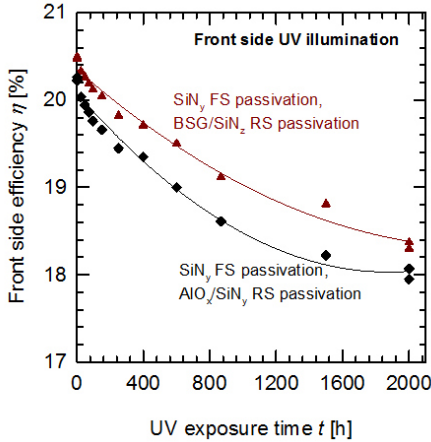
Figure 6.12: Measured spectral irradiance of the used UV lamps (UVASPOT, Höhnlle), reference AM1.5 solar spectral irradiance [AS12] and transmittance of the cover glass.

of the UV lamps.

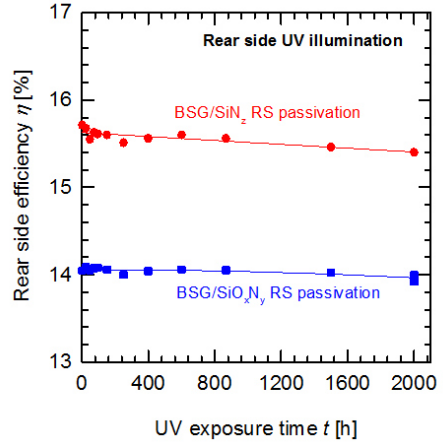
For increasing UV exposure times, the IV parameters of the solar cells are measured. Figure 6.13 shows the measured change in the cell efficiency η and the open-circuit voltage V_{oc} under UV illumination. Two of the n -BiCoRE cells are illuminated and measured from the front side (FS) (Fig. 6.13 (a) and (c)) that is textured, P-diffused and coated with a SiN_y layer as passivation and ARC. The cell with a BSG/ SiN_z rear side passivation and a starting efficiency of 20.5% (dark red triangles) and the $\text{AlO}_x/\text{SiN}_y$ passivated cell with a starting efficiency of 20.3% (black diamonds) lose 2.2%_{abs.} in FS efficiency after 2000 h. This loss is attributed to the significant drop in V_{oc} of 23-31 mV. At the beginning of the UV exposure, a fast degradation of the open-circuit voltages and thus the FS cell efficiencies is observed that slows down after about 1500 h of illumination so that the FS efficiencies seem to approximate constant values.

The cells that are illuminated and measured from the planar rear side (RS) (Fig. 6.13 (b) and (d)) that is B-diffused and passivated with a PECVD stack of BSG/SiN_z (red circles) or BSG/SiO_xN_y (blue squares) show an approximately constant RS efficiency of 15.6% and 14.0 % and V_{oc} of 666 mV and 661 mV during 2000 h of UV exposure. For the SiN_z capping layer, a FS efficiency loss of $\Delta\eta=0.3\%_{abs.}$ is measured that is within the measurement uncertainty while for the SiO_xN_y capping layer, a constant FS efficiency ($\Delta\eta=0.05\%_{abs.}$) is observed. The efficiencies of the unilluminated front sides of these BiCoRE cells of 20.1% and 20.2% (not plotted in Fig. 6.13) are also constant within the measurement uncertainty.

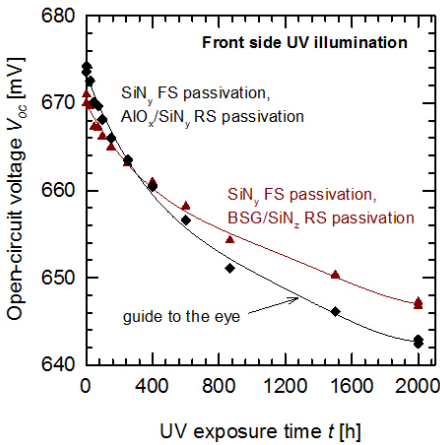
We conclude that the PECVD BSG passivation layer is stable, whereas the front side SiN_y degrades under intense UV illumination. The observed degradation of the passivation quality of silicon nitride is in agreement with the findings in [La98], where a decrease of the effective lifetime of SiN-passivated *p*-type Si lifetime-samples under UV illumination is reported. The UV stability is found to increase for increasing SiN thickness, for increasing UV cut-off wavelengths and for applying an encapsulation. For encapsulated bifacial Si solar cells, the SiN passivation is UV-stable and stable efficiencies of 17-18% for up to 20 years are prognosticated in [La98].



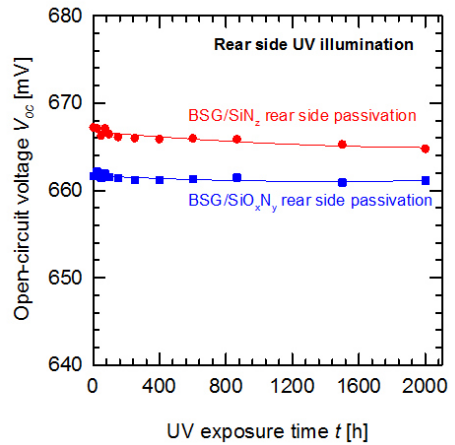
(a)



(b)



(c)



(d)

Figure 6.13: Change in efficiency η and open circuit voltage V_{oc} for n -type Bi-CoRE cells with SiN_y front side passivation and either PECVD BSG/SiN_z or $\text{BSG/SiO}_x\text{N}_y$ or $\text{AlO}_x/\text{SiN}_y$ rear side passivations under UV illumination. The four BiCoRE cells are covered with glass plates and illuminated and measured either from the front side (FS) or the rear side (RS).

Chapter 7

Process and device simulations

In this Chapter, we set up a process simulation model and apply the software “Sentaurus Process” in order to reproduce boron diffusion profiles that are formed during a POCl_3 co-diffusion from a PECVD BSG diffusion source.

Device simulations of n -PERT BJ cells are performed using the simulation tool “Quokka”. Free energy loss analysis (FELA) and synergistic efficiency gain analysis (SEGA) allow us to evaluate recombination loss contributions and potential efficiency gains.

7.1 Simulation of boron diffusion profiles

For the simulation of boron diffusion profiles, we use a process simulation model as described in [Wa11] that contains both the Si substrate and the dielectric layer. This is in contrast with most common diffusion models, where only the Si region is simulated with the surface dopant concentration N_s as boundary condition. In contrast to [Wa11], where a PSG layer is considered, we simulate the diffusion from a PECVD BSG layer with a thickness of 40 nm and a $[\text{SiH}_4]/[\text{B}_2\text{H}_6]$ gas flow ratio of 4% during a POCl_3 co-diffusion. We use the measured B concentrations in the PECVD BSG layer, the temperature, and time of the furnace process as input parameters. However, further simulation parameters such as the diffusivity and the segregation coefficient of B in the PECVD BSG layer must be considered.

Although the deposited layers are commonly called PECVD BSG, from the simulation point of view, they are treated as boron-doped oxides. In contrast to glasses, oxides have a high melting point and do not start to become viscous at typical diffusion temperatures of 800-1000 °C. Thus, in a B-doped oxide, a B concentration profile is present, and its variation during a diffusion process can be described by our process simulation model.

We use a temperature-independent segregation coefficient of B for the PECVD BSG layer of $k=0.357$ from [Su93] and an activation energy for the diffusion of B in the PECVD layer $E_{a,B,BSG}$ of 3.2-3.5 eV from [Wo86]. The PP-TOFMS-measured B concentration in the PECVD BSG diffusion source, $c_{B,BSG}=6.0 \times 10^{21} \text{ cm}^{-3}$, as indicated in Fig. 5.4, is used as an input parameter. The temperature profile of the co-diffusion including ramping from 700 °C to 950 °C and cooling (see Fig. 4.2) are taken into account.

Figure 7.1 shows exemplarily a simulated B concentration profile of a diffusion from a 40-nm-thick PECVD BSG layer with $[\text{SiH}_4]/[\text{B}_2\text{H}_6]=4\%$ (black line). The B concentration in the PECVD BSG diffusion source is adapted to the PP-TOFMS measured maximum concentration of $c_{B,BSG}=6.0 \times 10^{21} \text{ cm}^{-3}$ (bold red line). Using an activation energy of $E_{a,B,BSG}=3.28$ eV, the simulation matches the ECV-measured B concentration (dark red line) but results in a larger profile depth. This might be explained by an underestimation of the profile depth measured by the ECV technique due to carrier spillover (see [Wa11] for details). The PP-TOFMS measured B doping profile in Si (thin red line) slightly differs from the simulation and from the ECV measurements, both in shape and in depth. The PP-TOFMS measurement was performed after co-diffusion without etching, so that the B concentration in the PECVD BSG is also measured and visible in Fig. 7.1 for $d \leq 0 \text{ }\mu\text{m}$. The position $d=0 \text{ }\mu\text{m}$ of the Si surface is determined with an uncertainty of about $\pm 0.05 \text{ }\mu\text{m}$. With increasing profile depth, the signal-to-noise ratio of the PP-TOFMS measurement increases due to the decreasing boron concentration. The measurement quality may also degrade due to the rough surface of the Cz-Si substrate wafer and the dielectric layers on top. Thus, the ECV-measured and simulated concentration drop can not be dissolved by PP-TOFMS.

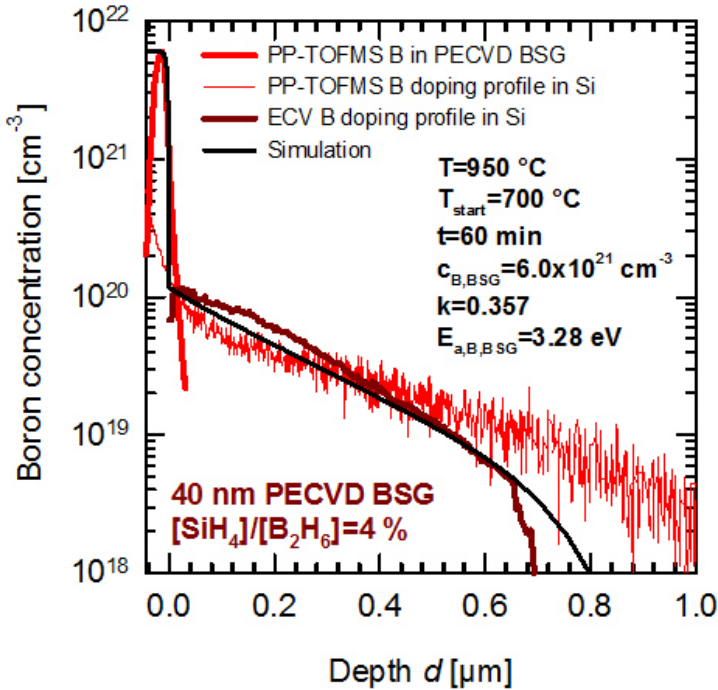


Figure 7.1: B doping profile after diffusion from a PECVD BSG layer as diffusion source in a co-diffusion process can be simulated using our process simulation model. The simulation and the experimental PP-TOFMS and ECV concentration profiles are matched by adapting the input parameters of the B concentration $c_{B,BSG}$ and the activation energy for the diffusion of B $E_{a,B,BSG}$ within the diffusion source.

We conclude that our simulation model using the PP-TOFMS-measured boron concentration in the diffusion source and the temperature profile of the co-diffusion as input parameters reproduces the ECV diffusion profile from the PECVD BSG layer very well. Thus, we successfully developed and applied the first simulation model for the boron diffusion from a solid boron diffusion source during co-diffusion that allows to reproduce experimental doping profiles and to study the impact of the diffusion source properties on the resulting boron profile.

7.2 Device simulations

We perform two-dimensional device simulations applying the Conductive Boundary (CoBo) model [Br12] as implemented in the Quokka software [Fe12]. The CoBo model uses the experimentally extracted R_{sheet} and J_0 data listed in Table 7.1 as input parameters.

Cell type	$R_{sheet,B}$ [Ω/\square]	$J_{0,B}$ [fA/cm ²]	impl. $V_{oc,B}$ [mV]	$R_{sheet,P}$ [Ω/\square]	$J_{0,P}$ [fA/cm ²]	impl. $V_{oc,P}$ [mV]
<i>n</i> -PERT BJ co-diffused	70	21	697	92	87	668
<i>n</i> -BiCoRE, BSG/SiN _z passivated	90	40	680	92	87	668
<i>n</i> -PERT BJ reference	100	24	707	155	46	670

Table 7.1: Experimental R_{sheet} , J_0 and $V_{oc,impl.}$ results of the boron and phosphorus dopings of the best *n*-PERT BJ and BiCoRE cells measured on symmetrically fabricated *n*-type Cz-Si J_0 -samples using $n_i=8.6\times 10^9$ cm⁻³ with an AlO_x/SiN_y or a BSG/SiN_z passivation, after firing.

The experimental $R_{sheet,B}$, $J_{0,B}$ and $V_{oc,impl.}$ data is measured on unmetallized test wafers that were processed in parallel with the 21.0% *n*-PERT BJ and the reference cell with AlO_x/SiN_y rear side passivation (see Table 6.2) and with the 20.6% BiCoRE cell with a PECVD BSG/SiN_z passivation stack (see Table 6.5).

Further input parameters are given in [Li16]. Important parameters are the measured wafer thickness of 151 μ m and a wafer resistivity of 5.6 Ω cm. For the metallized regions, J_0 values of 400 fA/cm² for the Ag front contacts and of 320 fA/cm² for the Al rear contacts are applied. The simulated cell results are specified in Table 7.2 and compared to the measured cell results.

Cell type		η [%]	FF [%]	J_{sc} [mA/cm ²]	V_{oc} [mV]
<i>n</i> -PERT BJ co-diffused	simulation	21.2	81.2	38.9	673
	measurement	21.0*	80.5	39.1	666
<i>n</i> -BiCoRE, BSG/SiN _z pass.	simulation	21.1	81.1	38.9	669
	measurement	20.6	78.5	39.2	668
<i>n</i> -PERT BJ reference [Li16]	simulation	21.6	81.0	39.4	679
	measurement	21.2*	80.0	39.3	674

* Independently confirmed by Fraunhofer ISE CalLab.

Table 7.2: Simulated cell results for co-diffused and reference *n*-PERT BJ cells obtained on a cell area of 239 cm² with 5-busbar layout. Also simulated results for a BiCoRE cell with a BSG/SiN_z rear side passivation instead of AlO_x/SiN_y are listed. The simulated results are compared to the measured IV parameters for the best *n*-PERT BJ and BiCoRE cells.

For the co-diffused and the reference *n*-PERT BJ cell with AlO_x/SiN_y rear side passivation, the simulated J_{sc} values match the experimental results, but the V_{oc} values are overestimated in the simulations resulting in higher simulated FF and η compared to the experimental data. The simulated cell results for a BSG/SiN_z passivation (BiCoRE cell) show the same J_{sc} and FF results as with an AlO_x/SiN_y stack (co-diffused *n*-PERT BJ cell), but a reduced V_{oc} due to the higher $J_{0,B}$ of 40 fA/cm² instead of 21 fA/cm². According to the Quokka simulations, a conversion efficiency of 21.1% is to be expected, that may be overestimated by 0.2%_{abs.}, as observed for the co-diffused *n*-PERT BJ cell efficiency. Hence, the slightly higher $J_{0,B}$ value of the BSG/SiN_z passivation compared to the AlO_x/SiN_y passivation translates into a 0.1%_{abs.} lower conversion efficiency. In summary, comparable cell results can be reached by the BSG/SiN_z passivation while realizing significant process simplifications by reducing dielectric etching and saving deposition steps.

7.2.1 Free energy loss analysis

Figure 7.2 shows the results of a free energy loss analysis (FELA), as described in [Br08], of the simulated *n*-PERT BJ cells applying co-diffusion and AlO_x/SiN_y passivation, co-diffusion and BSG/SiN_z passivation and, in the case of the reference cell, sequential diffusions.

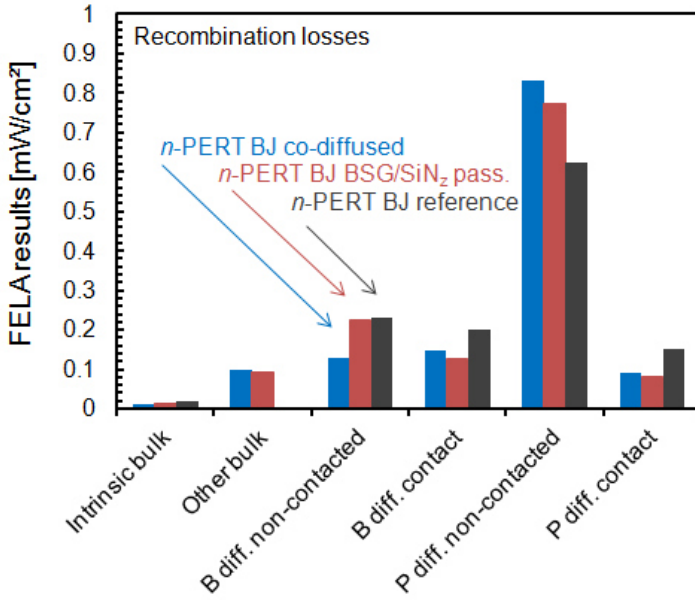


Figure 7.2: Free energy loss analysis (FELA) results for the recombination losses in the simulated co-diffused and reference n -PERT BJ cells carried out at the maximum power point (MPP). The internal generated power is 23.6 mW/cm^2 , the recombination losses add up to 1.3 mW/cm^2 .

Recombination in the non-metallized area of the phosphorus diffusion is the largest recombination loss and amounts to $0.77\text{-}0.83 \text{ mW/cm}^2$ for the co-diffused and 0.62 mW/cm^2 for the sequentially-diffused reference cell. Thus, the FSF that forms during co-diffusion needs to be further optimized by aiming at higher sheet resistances $R_{sheet,P}$ and lower $J_{0,P}$. There is only a small contribution of the non-metallized boron diffusion to the power losses of 0.13 mW/cm^2 for the co-diffused cell and 0.23 mW/cm^2 for the reference cell. This proves that the PECVD BSG boron diffusion source is successfully implemented into the n -PERT BJ cell fabrication. For the BSG/SiN_z-passivated boron diffusion, the recombination loss of 0.22 mW is increased compared to the co-diffused and AlO_x/SiN_y-passivated n -PERT BJ cell. This can be attributed to the higher passivation quality of the AlO_x/SiN_y stack with about 50% lower J_0 results. The screen-printed contacts result in low recombination losses $<0.2 \text{ mW/cm}^2$

for both the B and P diffusions that are even lower for the co-diffused cells due to the lower sheet resistances $R_{sheet,B}$ and $R_{sheet,P}$.

7.2.2 Synergistic energy gain analysis

Figure 7.3 shows the results of a synergistic energy gain analysis (SEGA) [Pe14] of the simulated n -PERT BJ cell applying co-diffusion and $\text{AlO}_x/\text{SiN}_y$ rear side passivation. The SEGA quantifies all individual power losses of the PERT BJ solar cell by setting the respective simulation input parameter from its real value to an ideal value corresponding to an ideal silicon solar cell with 29.0% efficiency. Hence, the simulated efficiency gains for the different loss mechanisms (grouped in resistance, optics and recombination, compare 2.2.2) are determined. In addition, by deactivating groups of losses simultaneously, the interaction of loss mechanisms is taken into account and efficiency gains from these “synergistic” effects are identified. For more details on the SEGA analysis and the origin of the synergy contributions we refer to reference [Br16].

The largest gain (1.1%_{abs.}) is possible when eliminating recombination in the non-metallized area of the phosphorus diffusion on the front side. In contrast, there is only a small gain of 0.1%_{abs.} possible when eliminating the recombination at the non-contacted boron diffusion. This demonstrates that the quality of our PECVD BSG boron diffusion is sufficiently high and reduces the efficiency of our cell by less than 0.1%. There is only a 0.1%_{abs.} gain from recombination in the bulk due to the used n -type silicon base material with a high bulk lifetime. Reducing recombination offers the largest potential for further cell improvements amounting in an ideal scenario to 1.5%_{abs.} from the sum of all individual recombination gains and a maximum improvement of 2.6%_{abs.} from synergistic effects if all recombination losses could be eliminated simultaneously. Through optical improvements, (2.2+0.1)%_{abs.} efficiency gain from the sum of all optical gains and from synergistic effects can be achieved while resistive improvements only contribute to 0.7%_{abs.}.

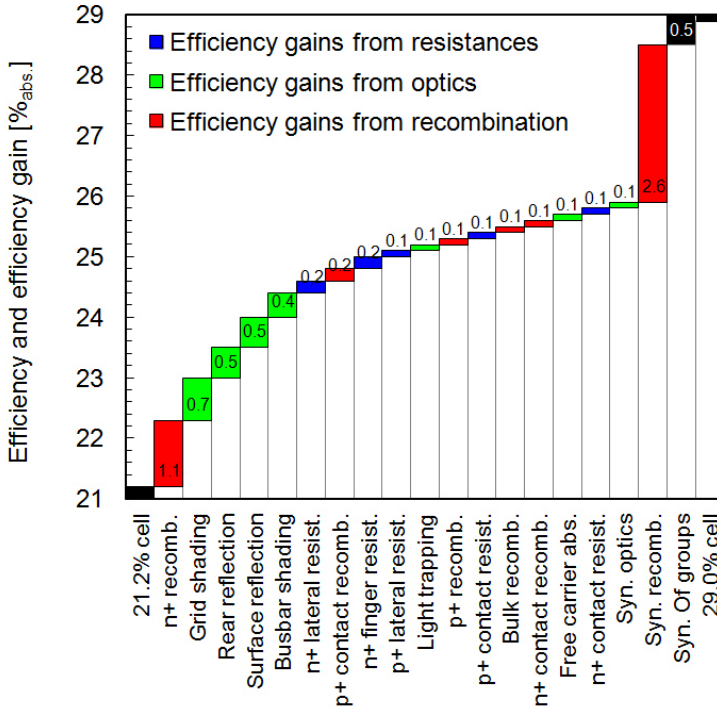


Figure 7.3: Synergistic energy gain analysis (SEGA) results for the simulated 21.2%-efficient co-diffused *n*-PERT BJ cell with $\text{AlO}_x/\text{SiN}_y$ rear side passivation.

In conclusion, the FELA and the SEGA prove the high quality of our boron diffusion source and shows the optimization potential for the phosphorus diffusion that leads to the main possible efficiency gain from recombination of 1.1%_{abs.}. The recombination in the phosphorus-diffused FSF of about 0.8 mW/cm² is the main free energy loss. This recombination loss contribution could be reduced by aiming at a higher P sheet resistance during POCl_3 co-diffusion comparable to $R_{sheet}=155 \Omega/\square$ of the reference cell and thus reducing $J_{0,P}$ to values below 50 fA/cm², as was reached during the separate POCl_3 diffusion of the reference cell.

Chapter 8

Summary and outlook

8.1 Summary

In this thesis, PECVD layer stacks and a co-diffusion process were successfully optimized and applied for the simplification of n -type silicon solar cell fabrication.

The properties of PECVD BSG layers as solid diffusion sources were investigated and the resulting boron diffusion was found to be mainly influenced by the gas flow ratio of $[\text{SiH}_4]/[\text{B}_2\text{H}_6]$. A two-stage POCl_3 co-diffusion process was developed to drive in the boron from the BSG to form the p^+ -emitter and to perform a phosphorus diffusion for n^+ FSF formation in only one high-temperature step. In order to prevent a phosphorus indiffusion in the BSG during co-diffusion, a capping layer needs to be applied on top of the PECVD BSG. We found that PECVD SiN_z and SiO_xN_y layers are suitable as P diffusion barriers and also as protection layers during chemical cleaning and texturing. As optimized boron diffusion sources, a stack of 40 nm BSG with $[\text{SiH}_4]/[\text{B}_2\text{H}_6]=8\%$ and 120 nm SiN_z was identified that allows for saturation current densities J_0 below 10 fA/cm^2 at boron sheet resistances R_{sheet} around $100 \Omega/\square$, when the p^+ -emitter is passivated with an $\text{AlO}_x/\text{SiN}_y$ stack and fired. Thus, the quality of the boron emitter diffused from PECVD BSG/ SiN_z is comparable to highest-quality BBr_3 -diffused B emitters.

We investigated the passivation quality of PECVD BSG/ SiN_z and BSG/ SiO_xN_y stacks and reached lowest published J_0 values of 40 fA/cm^2 for

a BSG/SiN_z-passivated p^+ -emitter. From a corona charge analysis, we found that the passivation quality of unannealed PECVD BSG is insufficient and it is only established after a high-temperature treatment, where the growth of a high-quality interface oxide was made responsible.

With the optimized PECVD diffusion source, we fabricated the first co-diffused n -PERT BJ cells and achieved an independently confirmed energy conversion efficiency of 21.0% on $15.6 \times 15.6 \text{ cm}^2$ cell area with a simplified process flow. This was the highest efficiency reported so far for a co-diffused n -type PERT BJ cell using PECVD BSG/SiN_z as diffusion source. From n -PERT BJ half cells, the first demonstration module was fabricated and reached an efficiency of 19.7% and a cell to module loss $< 6\%_{rel.}$.

We also integrated the PECVD diffusion source into the fabrication of high-efficiency BJBC cells. With a drive-in of B from PECVD BSG, a BJBC cell efficiency of 22.4% could be demonstrated.

In order to fully utilize the multifunctionality of the PECVD BSG/SiN_z stack acting as diffusion source and barrier, rear side passivation and ARC, we developed a novel bifacial co-diffused rear emitter cell concept that we named BiCoRE. The first n -type BiCoRE cells were fabricated in only 10 processing steps with a process flow comparable to industrial PERC cells and reached 20.6% efficiency and 78% bifaciality. In contrast to p -type PERC cells, that degrade under illumination, our n -type solar cells were found to be LID-stable. The UV-stability was tested and the BSG passivation layer was found to be stable under intense UV illumination for 2000 h which corresponds to 1.4 years under AM1.5 conditions. We set up a new process simulation model that contained both the silicon substrate and the PECVD BSG layer. With the boron concentration in the PECVD diffusion source as well as the temperature and time of the co-diffusion as input parameter, the experimental boron diffusion profiles could be reproduced. Device simulations including free energy loss and synergistic efficiency gain analysis of our co-diffused cells proved the high quality of the optimized PECVD BSG diffusion source. We identified the main possible efficiency gain of $1.1\%_{abs.}$ from improving the n^+ -FSF formed during co-diffusion.

8.2 Outlook

The PECVD deposition and boron drive-in on textured silicon was found to be challenging. Noncontinuous boron emitters with phosphorus indiffusions were observed. For increased B concentrations within the BSG diffusion source, deep continuous boron emitters could be achieved but the formation of a disadvantageous BRL could arise. As next steps, these challenges need to be overcome, if simplified front junction cells or BiCoRE cells with a textured rear side and thus an improved light-harvesting shall be fabricated.

Though the recombination in the n^+ -FSF was discovered as the main loss mechanism by our device simulations, the POCl_3 co-diffusion process needs to be further optimized by decreasing the saturation current density of the phosphorus diffusion. The co-diffusion can become more time and cost efficient by decreasing drive-in temperature and step duration and by potentially reaching a single-stage POCl_3 co-diffusion process. For a single-stage co-diffusion, due to the different diffusion mechanism and activation energies for B and P, an appropriate thermal budget needs to be identified: The diffusion temperature needs to be high enough to allow for a sufficient boron diffusion from PECVD BSG, so that a continuous p^+ -emitter is formed. However, for a high-quality n^+ -FSF characterised by low $J_{0,FSF}$ values, the temperature for the phosphorus diffusion needs to be reduced. Alternatively, an oxidation or etchback step might be applied in order to reduce the surface P concentration and thus the $J_{0,FSF}$.

In order to demonstrate the full potential for the simplified fabrication of high-efficiency BJBC cells, the integration of the POCl_3 co-diffusion into the BJBC process flow shall be realized. Our first co-diffused BJBC cells suffered from very low shunt resistances that significantly reduced the fill factor and the efficiency. The occurrence of shunting problems needs to be further investigated and avoided.

Our first 20.6%-efficient n -BiCoRE cells were limited by high series resistances that we attributed to the phosphorus FSF. The simulated cell efficiency of the BiCoRE cells of 21.1% can be reached and even outpassed with an optimized cell rear side concerning the n^+ -FSF. In addition, the PECVD BSG/ SiN_x rear side passivation can be optimized concerning the optical properties in order to further improve the rear side efficiency and

the bifaciality.

In the future, if the importance of n -type cell concepts increases, simplified n -PERT BJ and n -BiCoRE cells may be integrated into industrial PERC production lines and may follow the PERC cells as major industrial solar cell technology.

Chapter 9

Appendix

9.1 Abbreviations and symbols

Abbreviations

ALD	atomic layer deposition
AM	air mass
APCVD	atmospheric pressure chemical vapor deposition
ARC	anti-reflective coating
BiCoRE	bifacial co-diffused rear emitter (cell)
BJ	back junction
BJBC	back-junction back-contact
BSF	back surface field
CVD	chemical vapor deposition
Cz	Czochralski
DC	direct current
DI	deionized (water)
ECV	electrochemical capacitance-voltage (measurement)
EDS	energy-dispersive X-ray spectroscopy
EL	electroluminescence
FJ	front junction
FPP	four point probe
FS	front side
FSF	front surface field
Fz	float zone
ICP	inductively coupled plasma
LID	light-induced degradation
LCO	laser contact opening
LTO	low temperature oxidation
PCD	photoconductance decay
PECVD	plasma enhanced chemical vapor deposition
PERC	passivated emitter and rear cell
PERT	passivated emitter and rear, rear totally doped (cell)
QSSPC	quasi steady-state photoconductance
RCA	Radio Corporation of America standard chemical wafer cleaning process sequence
RF	radio frequency
RS	rear side

SEM	scanning electron microscopy
UV	ultra violet
VHF	very high frequency

Chemical elements and compounds

Ag	silver
Al	aluminium
AlO _x / Al ₂ O ₃	aluminium oxide
B	boron
BBr ₃	boron tribromide
BRL	boron rich layer
BSG	boron silicate glass
Cu	copper
EVA	ethylene vinyl acetate
H ₂	hydrogen
H ₂ O ₂	hydrogen peroxide
HCl	hydrochloric acid
HF	hydrofluoric acid
KOH	potassium hydroxide
N ₂ O	nitrous oxide
NH ₄ OH	ammonium hydroxide
Ni	nickel
P	phosphorus
POCl ₃	phosphorus oxychloride
PSG	phosphorus silicate glass
Si	silicon
SiH ₄	silane
SiN _z / Si ₃ N ₄	silicon nitride
SiO ₂	silicon dioxide
SiO _x N _y	silicon oxynitride

Symbols

A	cell area
c	speed of light
c	concentration
C	capacity
Δn	excess carrier density
d	thickness / depth
$D_{n/p}$	diffusivity of electrons / holes
ϵ	permittivity
ϵ_0	dielectric constant
η	conversion efficiency
E	energy
E_c	energy of the conduction band edge
E_g	energy of the band gap
E_v	energy of the valence band edge
FF	fill factor
G	generation rate
I	current
I_{mpp}	current at at maximum power point
I_{sc}	short circuit current
J_0	saturation current density
$J_{0,BSF}$	BSF saturation current density
$J_{0,e}$	emitter saturation current density
J_{sc}	short circuit current density
k	Boltzmann constant
λ	wavelength
μ_n	mobility of electrons
μ_p	mobility of holes
n	refractive index
n	total electron concentration
n_i	intrinsic carrier density
N_A	acceptor concentration
N_D	donor concentration
N_{dop}	dopant concentration
N_s	surface dopant concentration

p	total hole concentration
P_{light}	power from light irradiation
P_{mpp}	power at maximum power point
pFF	pseudo fill factor
q	elementary charge
Q	charge density
Q_{corona}	corona charge density
Q_f	fixed charge density
ρ	resistivity
R_{Aug}	Auger recombination rate
R_s	series resistance
R_{sh}	shunt resistance
R_{sheet}	sheet resistance
σ	conductivity
s	spacing
S_{eff}	effective surface recombination velocity
S_{n0}	surface recombination velocity of electrons
t	time
ϑ	Celsius temperature
T	temperature
τ	lifetime
τ_{Aug}	Auger lifetime
τ_{bulk}	bulk lifetime
τ_{eff}	effective lifetime
τ_{rad}	radiative lifetime
τ_{SRH}	Shockley-Read-Hall lifetime
U	voltage
U_K	Kelvin voltage
V	voltage
V_{mpp}	voltage at at maximum power point
V_{oc}	open circuit voltage
$V_{oc,impl}$	implied open circuit voltage
W	wafer thickness

9.2 References

- [Al03] P. P. Altermatt, A. Schenk, F. Geelhaar, G. Heiser, Reassessment of the intrinsic carrier density in crystalline silicon in view of band-gap narrowing, *J. Appl. Phys.*, Vol. 93, No. 3, pp. 1598-1604 (2003).
- [AS12] American Society for Testing and Materials (ASTM), Standard Tables for Reference Solar Spectral Irradiances: Direct Normal and Hemispherical on 37° Tilted Surface, ASTM G173 - 03 (2012).
- [Ba69] P. Balk, J. M. Elderidge, Phosphosilicate Glass Stabilization of FET Devices, *Proc. IEEE*, Vol. 57, No. 9, pp. 1558-1563 (1969).
- [Ba11] B. Bazer-Bachi, C. Oliver, B. Semmache, Y. Pellegrin, M. Gauthier, N. Le Quang, M. Lemiti, Co-diffusion from boron doped oxide and POCl_3 , *Proc. 26th EU PVSEC*, pp. 1155-1159 (2011).
- [Bo16] S. Bordihn, V. Mertens, J. Cieslak, G. Zimmermann, R. Lantsch, J. Scharf, S. Geißler, S. Hörnlein, M. Neuberger, S. Laube, A. Dietrich, B. Szramowski, S. Esefelder, T. Ballmann, B. Eisenhawer, A. Mohr, M. Schaper, K. Petter, J. W. Müller, D. J. W. Jeonga, R. Haob, T. S. Ravib, Status of Industrial Back Junction *n*-type Si Solar Cell Development, *Energy Procedia*, Vol. 92, pp. 678-683 (2016).
- [Br08] R. Brendel, S. Dreissigacker, N. P. Harder, and P. P. Altermatt, Theory of analyzing free energy losses in solar cells, *Appl. Phys. Lett.* 93, 173503 (2008).
- [Br12] R. Brendel, Modeling solar cells with the dopant-diffused layers treated as conductive boundaries, *Prog. Photovolt.: Res. Appl.*, 20, pp. 31-43 (2012).
- [Br16] R. Brendel, T. Dullweber, R. Peibst, C. Kranz, A. Merkle, D. Walter, Breakdown of the Efficiency Gap to 29% Based on Experimental Input Data and Modelling, *Prog. Photovolt: Res. Appl.*, 24, pp. 1475-1486 (2016).

- [Ca14] R. Cabal, B. Grange, L. Bounaas, R. Monna, N. Plassat, E. Pihan, Y. Veschetti, 20% PERT technology adapted to *n*-type mono-like silicon: Simplified process and narrowed cell efficiency distribution, Proc. 29th EUPVSEC, pp. 648-652 (2014).
- [Ch16] N. Chen, A. Ebong, Towards 20% efficient industrial Al-BSF silicon solar cell with multiple busbars and fine gridlines, Solar Energy Materials & Solar Cells, 146, pp. 107-113 (2016).
- [Cl97] D. A. Clugston and P. A. Basore, PC1D Version 5: 32-bit solar cell modeling on personal computers, Proc. 26th IEEE Photovoltaic Specialists Conference, Anaheim, pp. 207-210 (1997).
- [Da02] S. Dauwe, J. Schmidt, R. Hezel, Very low surface recombination velocities on *p*- and *n*-type silicon wafers passivated with hydrogenated amorphous silicon films, Proc. 29th IEEE Photovoltaic Specialists Conference, pp. 1246-1249 (2002).
- [Du12] T. Dullweber, S. Gatz, H. Hannebauer, T. Falcon, R. Hesse, J. Schmidt, and R. Brendel, Towards 20% efficient large-area screen-printed rear-passivated silicon solar cells, Prog. Photovolt.: Res. Appl., 20, pp. 630-638 (2012).
- [Du13] T. Dullweber, C. Kranz, U. Baumann, R. Hesse, D. Walter, J. Schmidt, P. Altermatt, and R. Brendel, Silicon wafer material options for highly efficient *p*-type PERC solar cells, Proc. 39th IEEE PVSC, pp. 3074-3078 (2013).
- [DK13] T. Dullweber, C. Kranz, B. Beier, B. Veith, J. Schmidt, B. F. P. Roos, O. Hohn, T. Dippell, R. Brendel, Inductively coupled plasma chemical vapour deposited $\text{AlO}_x/\text{SiN}_y$ layer stacks for applications in high-efficiency industrial-type silicon solar cells, Solar Energy Materials & Solar Cells 112, pp. 196-201 (2013).
- [En15] J. Engelhardt, A. Frey, S. Gloger, G. Hahn, B. Terheiden, Passivating boron silicate glasses for co-diffused high-efficiency *n*-type silicon solar cell application, Appl. Phys. Lett. 107, 042102 (2015).

- [Fe12] A. Fell, Quokka version 2: Selective surface doping, luminescence modeling and data fitting, *IEEE Trans. Electron Devices* 60 (2), pp. 733-738 (2012).
- [Fr14] A. Frey, J. Engelhardt, S. Fritz, S. Gloger, G. Hahn, B. Terheiden, *N*-type bi-facial solar cells with boron emitters from doped PECVD layers, *Proc. 29th EUPVSEC*, pp. 656-660 (2014).
- [Go98] A. Goetzberger, J. Knobloch, B. Voss, *Crystalline Silicon Solar Cells*, John Wiley & Sons Ltd., Chichester, England (1998).
- [Go03] J. Goldstein, D. Newbury, D. Joy, C. Lyman, P. Echlin, E. Lifshin, L. Sawyer, J. Michael, *Scanning Electron Microscopy and X-Ray Microanalysis*, Third Edition, Springer, New York, USA (2003).
- [Gr16] M. A. Green, K. Emery, Y. Hishikawa, W. Warta and E. D. Dunlop, Solar cell efficiency tables (version 47), *Prog. Photovolt: Res. Appl.*, 24, pp. 3-11 (2016).
- [Ha14] H. Hannebauer, T. Dullweber, U. Baumann, T. Falcon, R. Brendel, 21.2%-efficient fineline-printed PERC solar cell with 5 busbar front grid, *Phys. Status Solidi RRL* 8, No. 8, pp. 675-679 (2014).
- [Hi11] D. Hinken, C. Schinke, S. Herlufsen, A. Schmidt, K. Bothe, R. Brendel, Experimental setup for camera-based measurements of electrically and optically stimulated luminescence of silicon solar cells and wafers, *Review of Scientific Instruments*, 82, 033706, pp. 1-9 (2011).
- [Ho07] B. Hoex, J. Schmidt, R. Bock, P.P. Altermatt, M. C. M. van de Sanden, W. M. M. Kessels, Excellent passivation of highly doped *p*-type Si surfaces by the negative-charge-dielectric Al₂O₃, *Appl. Phys. Lett.* 91, 112107, pp. 1-3 (2007).
- [Ho08] B. Hoex, J. Schmidt, P. Pohl, M. C. M. van de Sanden, W. M. M. Kessels, Silicon surface passivation by atomic layer deposited Al₂O₃, *Journal of Applied Physics* 104, 044903, pp. 1-12 (2008).

- [Hu99] R. Hull, Properties of cristalline silicon, INSPEC, London, UK (1999).
- [IT16] International Technology Roadmap for Photovoltaic (ITRPV): Results 2015, Seventh Edition (March 2016).
- [Ka85] D. E. Kane, R. M. Swanson, Measurement of the emitter saturation current by a contactless photoconductivity decay method, Proc. 18th IEEE Photovoltaic Specialists Conference, pp. 578-583 (1985).
- [KC02] M.J. Kerr, A. Cuevas, Comprehensive study of the doping and injection-level dependence of stoichiometric plasma silicon nitride passivation for silicon solar cells, Proc. 29th IEEE Photovoltaic Specialists Conference, pp. 102-105 (2002).
- [Ke10] M. A. Kessler, T. Ohrdes, B. Wolpensinger, N.-P. Harder, Charge carrier lifetime degradation in Cz silicon through the formation of a boron-rich layer during BBr_3 diffusion processes, Semicond. Sci. Technol. 25, 055001, pp. 1-9 (2010).
- [Ke13] R. Keding, D. Stüwe, M. Kamp, C. Reichel, A. Wolf, R. Woehl, D. Borchert, H. Reinecke, D. Biro, Co-Diffused Back-Contact Back-Junction Silicon Solar Cells without Gap Regions, IEEE J. Phtovoltaics, Vol. 3, No. 4, pp. 1236-1242 (2013).
- [Ku12] I. Kurachi, K. Yoshioka, Investigation of Boron Solid-Phase Diffusion from BSG Film Deposited by AP-CVD for Solar Cell Application, Proc. 27th EUPVSEC, pp.1873-1876 (2012).
- [La98] T. Lauinger, J. Moschner, A. G. Aberle, R. Hezel, Optimization and characterization of remote plasma-enhanced chemical vapor deposition silicon nitride for the passivation of *p*-type crystalline silicon surfaces, J. Vac. Sci. Technol. A 16 (2), pp. 530-543 (1998).
- [Li14] B. Lim, T. Brendemühl, M. Berger, A. Christ, and T. Dullweber, *N*-PERT back junction solar cells: an option for the next industrial technology generation?, Proc. 29th EUPVSEC, pp. 661-665 (2014).

- [Li16] B. Lim, T. Brendemühl, T. Dullweber, R. Brendel, Loss Analysis of *n*-Type Passivated Emitter Rear Totally Diffused Back-Junction Silicon Solar Cells with Efficiencies up to 21.2%, IEEE Journal of Photovoltaics, Vol. 6, No. 2, pp. 447-453 (2016).
- [LO15] LOANA Solar Cell Analysis System, pvtools, User Manual (06.2015).
- [Ma03] T. Markvart, L. Castaner, Practical Handbook of Photovoltaics: Fundamentals and Applications, Elsevier, Oxford, UK (2003).
- [MB16] Meyer Burger, SiNA/MAiA, The modular system for anti-reflection coating and passivation layers, fact sheet (2016).
- [Mc10] K.R. McIntosh and P.P. Altermatt, A freeware 1D emitter model for silicon solar cells, Proc. 35th Photovoltaic Specialists Conference, pp. 2188-2193 (2010).
- [Me13] V. Mertens, T. Ballmann, J. Cieslak, M. Kauert, A. Mohr, F. Stenzel, M. Junghänel, K. Suva, C. Klenke, G. Zimmermann, and W. Müller, Large area *n*-type Cz double side contact back junction solar cell with 21.3% conversion efficiency, Proc. 28th EUPVSEC, pp. 714-717 (2013).
- [No02] M. A. Noras, Trek Application Note, Number 3001 (2002).
- [Pe14] J. H. Petermann, Prozessentwicklung & Verlustanalysen für dünne monokristalline Siliziumsolarzellen und deren Prozessierung auf Modullevel, Dissertation, Leibniz Universität Hannover (2014).
- [Ri13] A. Richter, J. Benick, and M. Hermle, Boron emitter passivation with Al₂O₃ and Al₂O₃/SiN_x stacks using ALD Al₂O₃, IEEE Journal of Photovoltaics, Vol. 3, No. 1, pp. 236-245 (2013).
- [Ro13] P. Rothardt, R. Keding, A. Wolf, D. Biro, Co-diffusion from solid sources for bifacial *n*-type solar cells, Phys. Status Solidi RRL 7, pp. 623-626 (2013).

- [Ro14] P. Rothhardt, S. Meier, K. Jiang, A. Wolf, D. Biro, 19.9% efficient bifacial *n*-type solar cell produced by co-diffusion - CoBiN, Proc. 29th EUPVSEC, pp. 653-655 (2014).
- [Sc98] J. Schmidt, Untersuchungen zur Ladungsträgerrekombination an den Oberflächen und im Volumen von kristallinen Silicium-Solarzellen, Dissertation, Leibniz Universität Hannover (1998).
- [Sc04] J. Schmidt, Light-induced degradation in crystalline silicon solar cells, Solid State Phenomena 95-96, pp. 187-196 (2004).
- [Sc07] J. Schmidt, K. Bothe, R. Bock, C. Schmiga, R. Krain, R. Brendel, *N*-type silicon - the better material choice for industrial high-efficiency solar cells?, Proc. 22nd EUPVSEC, pp. 998-1001 (2007).
- [Sc09] J. Schmidt, B. Veith, and R. Brendel, Effective surface passivation of crystalline silicon using ultrathin Al₂O₃ films and Al₂O₃/SiN_x stacks, Phys. Status Solidi RRL 3, pp. 287-289 (2009).
- [Se13] J. Seiffe, F. Pillath, D. Trogus, A. Brand, C. Savio, M. Hofmann, J. Rentsch, R. Preu, Multifunctional PECVD layers: Dopant source, passivation and optics, IEEE Journal of Photovoltaics, Vol. 3, No. 1, pp. 224-229 (2013).
- [Sh61] W. Shockley, H. J. Queisser, Detailed balance limit of efficiency of *p-n* junction solar cells, Journal of Applied Physics, Vol. 32, pp. 510-519 (1961).
- [SH15] H. Schulte-Huxel, S. Blankemeyer, A. Merkle, V. Steckenreiter, S. Kajari-Schröder, R. Brendel, Interconnection of busbar-free back contacted solar cells by laser welding, Prog. Photovolt: Res. Appl., 23, pp. 1057-1065 (2015).
- [Si06] WCT-120 Photoconductance Lifetime Tester, User Manual, Sinton Instruments, Boulder, USA (2006-2012).

- [Sr98] D. K. Schroder, Semiconductor material and device characterization, Second edition, John Wiley & Sons, New York, USA (1998).
- [Su93] K. Suzuki, Y. Yamashita, Y. Kataoka, K. Yamazaki, and K. Kawamura, Segregation coefficient of boron and arsenic at polycrystalline silicon/SiO₂ interface, J. Electrochem. Soc., vol. 140, no. 10, pp. 2960-2964 (1993).
- [Te14] A. Tempez, S. Legendre, P. Chapon, Depth profile analysis by plasma profiling time of flight mass spectrometry, Nucl. Instr. Meth. B 332, pp. 351-354 (2014).
- [Ur15] A. Uruena, M. Aleman, E. Cornagliotti, A. Sharma, J. Deckers, M. Haslinger, L. Tous, R. Russell, J. John, Y. Yao, T. Söderström, F. Duerinckx, J. Szlufcik, Beyond 22% large area *n*-type silicon solar cells with front laser doping and a rear emitter, Proc. 31st EUPVSEC, pp. 410-413 (2015).
- [VAAT] Von Ardenne, Betriebsanleitung CS 400 P Clustersystem (2010).
- [Wa11] H. Wagner, A. Dastgheib-Shirazi, R. Chen, S.T. Dunham, M. Kessler, and P.P. Altermatt, Improving the predictive power of modeling the emitter diffusion by fully including the phosphosilicate glass (PSG) layer, Proc. 37th IEEE Photovoltaic Specialists Conference, Art. No. 835, pp. 2957-2962 (2011).
- [Wa13] H. Wagner, Improving the predictive power of modeling the emitter diffusion by fully including the phosphosilicate glass (PSG) layer development of simulation models for crystalline silicon solar cells, (in German), Ph.D. dissertation, Leibniz University of Hannover, Hannover, Germany (2013).
- [We14] F. Werner, Atomic layer deposition of aluminum oxide on crystalline silicon: Fundamental interface properties and application to solar cells, Dissertation, Leibniz Universität Hannover (2014).

-
- [Wo86] C. Wong and F. Lai, Ambient and dopant effects on boron diffusion in oxides, *Appl. Phys. Lett.*, vol. 48, p. 1658 (1986).
- [WP03] Measurement theory for the Wafer Profiler CVP21 (2003).
- [WT86] S. Wolf and R. Tauber, *Silicon Processing for the VLSI Era (Vol I)*, Lattice Press [ISBN 0-961672-3-7], p. 223 (1986).
- [Ye16] F. Ye, W. Deng, W. Guo, R. Liu, D. Chen, Y. Chen, Y. Yang, N. Yuan, J. Ding, Z. Feng, P. P. Altermatt, P. J. Verlinden, 22.13% efficient industrial *p*-type mono PERC solar cell, *Proc. 43rd IEEE Photovoltaic Specialists Conference*, pp. 3360-3365 (2016).

9.3 List of publications

Parts of this work have been published before in:

Refereed journal papers

- [1] T. Dullweber, N. Wehmeier, A. Nowack, T. Brendemühl, S. Kajari-Schröder, and R. Brendel, BiCoRE: combining a PERC-type cell process with *n*-type wafers, *Photovoltaics International*, Vol. 33, pp. 37-44 (2016).
- [2] T. Dullweber, N. Wehmeier, A. Nowack, T. Brendemühl, S. Kajari-Schröder, R. Brendel, Industrial bifacial *n*-type silicon solar cells applying a boron co-diffused rear emitter and an aluminum rear finger grid, *Phys. Status Solidi A*, Vol. 213, No. 11, pp. 3046-3052 (2016).
DOI 10.1002/pssa.201600346
- [3] N. Wehmeier, A. Nowack, B. Lim, T. Brendemühl, S. Kajari-Schröder, J. Schmidt, R. Brendel, T. Dullweber, 21.0%-efficient screen-printed *n*-PERT back-junction silicon solar cell with plasma-deposited boron diffusion source, *Solar Energy Materials and Solar Cells*, Vol. 158, No. 1, pp. 50-54 (2016).
DOI 10.1016/j.solmat.2016.05.054
- [4] N. Wehmeier, B. Lim, A. Nowack, J. Schmidt, T. Dullweber, and R. Brendel, 21.0%-efficient co-diffused screen printed *n*-type silicon solar cell with rear-side boron emitter, *Phys. Status Solidi RRL*, Vol. 10, No. 2, pp. 148-152 (2016).
DOI 10.1002/pssr.201510393
- [5] N. Wehmeier, B. Lim, A. Merkle, A. Tempez, S. Legendre, H. Wagner, A. Nowack, T. Dullweber, and Pietro P. Altermatt, PECVD BSG diffusion sources for simplified high-efficiency *n*-PERT BJ and BJBC solar cells, *IEEE Journal of Photovoltaics*, Vol. 6, No. 1, pp. 119-125 (2016).
DOI 10.1109/JPHOTOV.2015.2493364

Refereed papers and presentations presented at international conferences

- [1] N. Wehmeier, S. Kajari-Schröder, T. Brendemühl, A. Nowack, R. Brendel, T. Dullweber, Industrial *n*-type bifacial co-diffused rear emitter solar cells with boron silicate glass as diffusion source and passivation, Proc. 32nd European Photovoltaic Solar Energy Conference and Exhibition, pp. 443-446 (2016).
- [2] A. Tempez, S. Legendre, N. Wehmeier, B. Lim, H. Wagner, and P. P. Altermatt, Ultra fast depth profile analysis of boron silicate glass by plasma profiling time of flight mass spectrometry, presentation at Photovoltaic Technical Conference, Aix-en-Provence (2015).
- [3] N. Wehmeier, B. Lim, A. Tempez, S. Legendre, H. Wagner, T. Dullweber, and P.P. Altermatt, Investigation of PECVD BSG diffusion sources for simplified high-efficiency *n*-PERT BJ solar cells, Technical Digest of The 6th World Conference on Photovoltaic Energy Conversion, pp. 531-532 (2014).
- [4] N. Wehmeier, G. Schraps, H. Wagner, B. Lim, N.-P. Harder, and P. P. Altermatt, Boron-doped PECVD silicon oxides as diffusion sources for simplified high-efficiency solar cell fabrication, Proc. 28th European Photovoltaic Solar Energy Conference and Exhibition, pp. 1980-1985 (2013).

9.4 Acknowledgement

First of all, I would like to thank my referees Prof. Dr. Jan Schmidt and Prof. Dr.-Ing. Tobias Wietler for their time and effort, patience and encouragement. I thank my colleagues from the SimpliHigh and PERC2.0 projects, especially Dr. Bianca Lim, Dr. Sarah Kajari-Schröder, Anja Nowack and Till Brendemühl for planning and discussions and new planning, Miriam Berger, Anja Christ and Peter Giesel for n -PERT cell processing and Dr. Mircea Turcu for depositions and characterization. Thanks to Sarah Spätlich for diffusion optimization and David Sylla and Tobias Neubert for laser processes. For furnace diffusions and ECV measurements, I thank Gunnar Schrap. Thanks to Agnes Merkle for BJBC cell concept discussions and fabrication, to Bettina Wolpensinger for SEM and EDS analysis and to Dr. Agnes Tempez for PP-TOFMS measurements. Thanks to Dr. Ralf Gogolin and Michael Siebert for the Clustersystem support. For supporting the process and device simulations, I would like to acknowledge Prof. Dr. Pietro Altermatt, Dr. Hannes Wagner and Prof. Dr.-Ing. Rolf Brendel. Thanks to Arnaud Morlier and Robert Witteck for supporting the UV stability test. For mastering all electrical and mechanical, IT and energy saving challenges, I thank Stefan Beisse, Michael Weiß, Dirk Bartels, Johannes Schlieker, Andreas Treder, Jo Otto, Tobias Ziegner and Manuel Stratmann. For organizational and administrative questions, Marita Steinhof, Sabine Kreber, Brigitte Hielscher, Mareike Weiner, Wolfgang Gaßdorf, Markus Klöpfer, Marion Brucksch, Simone Lücking, Iris Berger and Lisa Brunotte are acknowledged. Special thanks to my office colleagues Verena Steckenreiter, Alwina Knorr and Anja Nowack for scientific and non-scientific discussions and to all other colleagues of ISFH for the good working atmosphere.

Thanks to the institute leader Prof. Dr.-Ing. Rolf Brendel and to all group leaders - especially Dr. Sarah Kajari-Schröder, Prof. Dr. Jan Schmidt, Dr. Thorsten Dullweber and Prof. Dr. Robby Peibst - for facilitating solar energy research.

Parts of this work arise from project work that was funded by the German Federal Ministry for Economic Affairs and Energy under Grant 0325478 (SimpliHigh) and Grant 0325880A (PERC 2.0) and by the state of Lower Saxony.

LEBENS LAUF

PERSÖNLICHE DATEN

Name: Nadine Wehmeier
Anschrift: Memeler Str. 15
31789 Hameln
Geburtsdatum: 31.10.1986
Geburtsort: Bünde
Staatsangehörigkeit: deutsch
Familienstand: ledig



SCHULBILDUNG

1997 - 2006: Städtisches Gymnasium Löhne, Abitur

STUDIUM

Universität: Westfälische Wilhelms-Universität Münster
Studiengang: Physik, mit Spezialisierung auf Medizinische Physik und Biophysik, Bionik, Photovoltaik, Messtechnik, Material- und Halbleiterphysik, Thermoelektrik
10.2006 - 09.2009: B.Sc. Physik, Bachelorarbeit zum Thema Grätzel-Zelle
10.2009 - 09.2011: M.Sc. Physik, Masterarbeit zu Isotopenangereicherten Silizium- Multilagenstrukturen für thermoelektrische Anwendungen

BERUFSERFAHRUNG

seit 01.2012: Wissenschaftliche Mitarbeiterin am Institut für Solar-energieforschung Hameln (ISFH)
Themen: Solarzellenentwicklung, Plasma-Beschich-
tungen, Diffusionsprozesse

Hameln, 20. Oktober 2016